UNIVERSITY OF ROCHESTER
LABORATORY FOR LASER ENERGETICS

Volume 134
January–March 2013
DOE/NA/28302-1106

LLE Review

Quarterly Report

About the Cover:

The cover photo highlights some of the contributors to laser development and operation for the demonstration of 1-D multi-FM smoothing by spectral dispersion on OMEGA EP. The Laser-Technology Development group [J. Zuegel, R. Cuffney, A. Okishev, I. Begishev, C. Dorrer, and R. Roides (not pictured)]; System Science group (B. Kruschwitz and J. Kelly); Electronics group (W. Bittle and G. Kick); and Laser Sources group (E. Hill, A. Consentino, and G. Balonek) were involved in designing, building, and operating systems to support the multi-FM smoothing demonstration, with primary goals of safe operation on a NIF-like system and characterization of beam-smoothing performance.

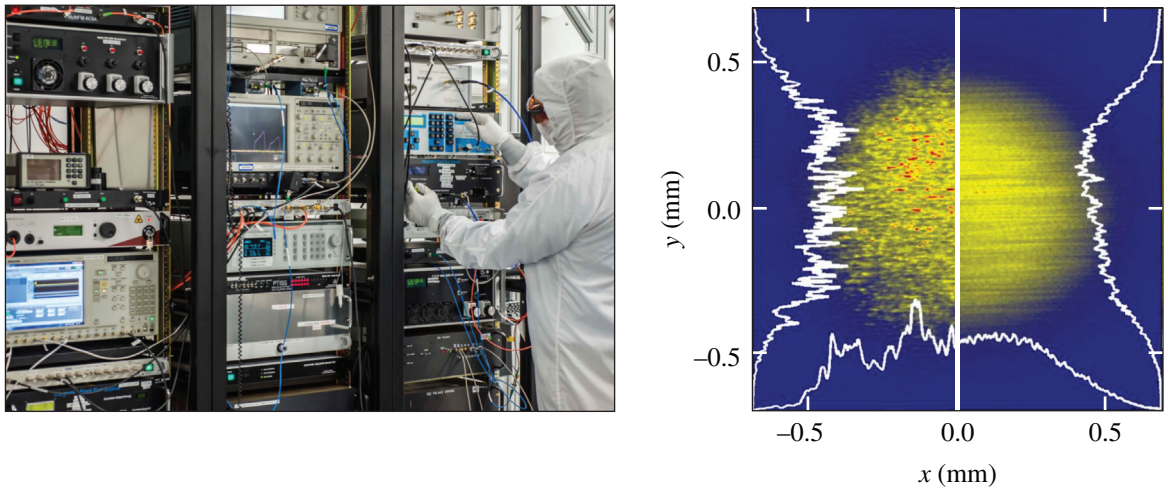

The picture on the left shows Rick Roides making adjustments to the fiber front end built to support the demonstration of multi-FM beam smoothing on OMEGA EP. The figure on the right presents equivalent-target-plane measurements of the OMEGA EP focal spot after frequency conversion, propagation in a distributed phase plate, and focusing. High-contrast speckles are observed without smoothing by spectral dispersion, but significant beam smoothing is demonstrated with multi-FM phase modulation and a diffraction grating in the NIF preamplifier module.

The work described in this volume includes current research at the Laboratory for Laser Energetics, which is supported by New York State Energy Research and Development Authority, the University of Rochester, the U.S. Department of Energy Office of Inertial Confinement Fusion under Cooperative Agreement No. DE-FC52-08NA28302, and other agencies.

Printed in the United States of America
Available from
National Technical Information Services
U.S. Department of Commerce
5285 Port Royal Road
Springfield, VA 22161
www.ntis.gov

For questions or comments, contact
Christophe Dorrer, Editor
Laboratory for Laser Energetics
250 East River Road
Rochester, NY 14623-1299
(585) 273-2778
www.lle.rochester.edu

UNIVERSITY OF ROCHESTER
LABORATORY FOR LASER ENERGETICS

Volume 134
January–March 2013
DOE/NA/28302-1106

LLE Review

Quarterly Report

UR LLE

Contents

In Brief

This volume of the LLE Review, covering January–March 2013, features "Commissioning of a Multiple-Frequency−Modulation Smoothing by Spectral Dispersion Demonstration System on OMEGA EP" by B. E. Kruschwitz, J. H. Kelly, C. Dorrer, A. V. Okishev, L. J. Waxer, G. Balonek, I. A. Begishev, W. Bittle, A. Consentino, R. Cuffney, E. Hill, J. A. Marozas, M. Moore, R. G. Roides, and J. D. Zuegel. In this article (p. 75), the performance of OMEGA EP seeded by optical pulses with high-frequency phase modulations is described. This demonstration includes angular dispersion by a diffraction grating, propagation and amplification in a NIF preamplifier module and one OMEGA EP beamline, frequency conversion, and beam smoothing after a distributed phase plate and focusing. Laser operation is characterized in conditions relevant to an implementation of multi-FM beam smoothing on the NIF to support polar drive.

Additional highlights of research presented in this issue include the following:

- J. H. Kelly, A. Shvydky, J. A. Marozas, M. J. Guardalben, B. E. Kruschwitz, L. J. Waxer, C. Dorrer, E. Hill, and A. V. Okishev present modeling and simulation results describing the propagation of spatially dispersed frequency-modulated optical pulses. A Miró model is used to set a peak-power limit for multi-FM pickets, taking into account nonlinear propagation in the optical components and conversion of frequency modulation into amplitude modulation because of diffraction.

- C. Dorrer, R. G. Roides, R. Cuffney, A. V. Okishev, W. A. Bittle, G. Balonek, A. Consentino, E. Hill, and J. D. Zuegel describe the fiber front end built to support the demonstration of multi-FM beam smoothing on OMEGA EP. High-bandwidth pulse shaping, multi-FM phase modulation, spectral-amplitude compensation, chromatic dispersion compensation, and fail-safe systems have been implemented to provide seed pulses that meet all operational requirements.

- J. F. Myatt, R. W. Short, A. V. Maximov, and W. Seka (LLE); H. X. Vu (University of California); D. F. DuBois (LANL); D. A. Russell (Lodestar Research); and J. Zhang and D. H. Edgell (LLE and Department of Mechanical Engineering, University of Rochester) present a generalization of the extended Zakharov model of two-plasmon decay that includes the evolution of the electron-distribution function in the quasi-linear approximation. This makes it possible to investigate anomalous absorption of laser light and hot-electron production caused by the two-plasmon–decay instability of multiple overlapping electromagnetic waves.

- J. Li and J. R. Davies (LLE and Department of Mechanical Engineering, University of Rochester); W. B. Mori (University of California); C. Ren (LLE, Department of Mechanical Engineering and Department of Physics and Astronomy, University of Rochester); A. A. Solodov and W. Theobald (LLE); T. Ma (LLNL and University of California); and J. Tonge (University of California) present particle-in-cell simulation results pertaining to cone-in-shell integrated fast-ignition experiments at the Omega Laser Facility, providing further evidence of the detrimental effects of pre-plasma in the cone. Studies of hot-electron generation from laser/pre-plasma interactions and transport show that the generated hot electrons are dominated in number by low-energy electrons but in energy by multi-MeV electrons.

- J. E. Schoenly (University of Toronto, LLE, and Institute of Optics, University of Rochester); W. Seka (LLE and Institute of Optics, University of Rochester); and P. Rechmann (University of California) describe experiments and models relating to dental calculus ablation in human teeth using 400-nm laser pulses. Calculus-removal rates, microscopy, and spectroscopy after irradiation are consistent with tissue-specific ablation at 400 nm caused by absorption by bacterial porphyrins within calculus. A heuristic model for calculus ablation agrees well with observed data.

Christophe Dorrer
Editor

Commissioning of a Multiple-Frequency–Modulation Smoothing by Spectral Dispersion Demonstration System on OMEGA EP

Introduction

Smoothing by spectral dispersion (SSD) has become a critically important method for smoothing laser-imprinted nonuniformities in target implosions.[1] The spot shape on target is generally controlled using distributed phase plates (DPP's), which effectively control the low-order beam profile but introduce fine-scale speckle structures that require smoothing.[2] Recently, a new concept for a one-dimensional (1-D) SSD system was proposed that utilizes multiple frequencies for phase modulation (multi-FM SSD).[3] By carefully selecting modulation frequencies, resonant features that often limit the effectiveness of SSD systems can be eliminated. As a result, effective beam smoothing can be achieved with a 1-D system using a modest modulation bandwidth in a frequency-conversion scheme that utilizes a single tripler crystal. These features allow for the integration of multi-FM SSD into either the OMEGA EP Laser System[4] or the National Ignition Facility (NIF)[5] laser.

Polar-drive experiments on the NIF will require pulse shapes that incorporate multi-FM SSD.[6] Conceptual pulse shapes are illustrated in Fig. 134.1. The three different shapes correspond to three different latitudes of the beams entering the NIF target chamber, with Ring 1 corresponding to higher latitudes and Ring 3 being nearest the equator. Beam smoothing using multi-FM SSD is required only during the three pickets at the beginning of the pulse. During the main pulse, at which higher power levels are required and amplitude modulation becomes a correspondingly greater concern, only the standard NIF 1-D SSD and stimulated Brillouin scattering suppression (SBSS) would be applied. Therefore, dynamic application of the multi-FM SSD bandwidth must be accommodated in the system design.

To demonstrate multi-FM SSD on a laser system with an architecture similar to the NIF, a prototype system was developed and integrated into a long-pulse beamline of OMEGA EP. Simulations of amplitude modulation caused by free-space propagation of a frequency-modulated beam in the OMEGA EP beamline and the design and performance of the fiber front end supporting multi-FM experiments on OMEGA EP are

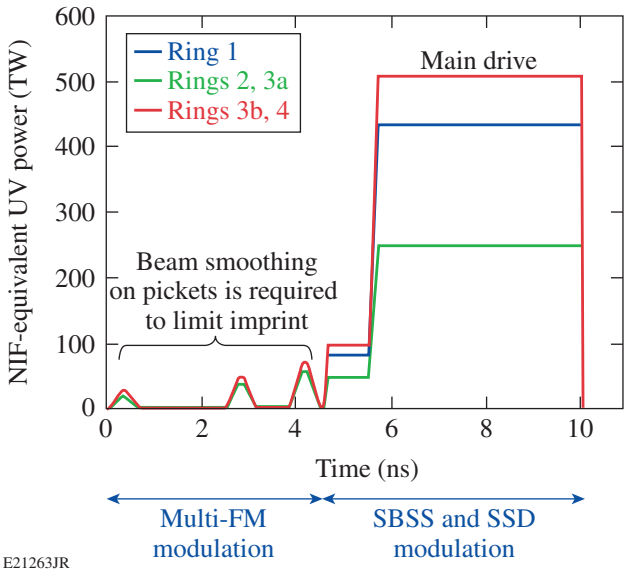

Figure 134.1
Representative triple-picket pulse shapes for polar-drive experiments on the NIF. The three pulse shapes correspond to beams entering the target chamber at different latitudes. In all cases, multi-FM smoothing by spectral dispersion (multi-FM SSD) is applied for only the picket pulses. SBSS: stimulated Brillouin scattering suppression.

presented in ***Simulations of the Propagation of Multiple-FM Smoothing by Spectral Dispersion on OMEGA EP*** (p. 85) and ***Fiber Front End with Multiple Phase Modulations and High-Bandwidth Pulse Shaping*** (p. 98). This article describes the prototype system and presents results from the integration and commissioning on the OMEGA EP beamline. Particular attention is paid to the important issue of amplitude modulation in the high-power beam at critical points in the system.

System Description

The prototype multi-FM SSD front end is illustrated in Fig. 134.2. A fiber front end comprises two separate channels—a main-pulse channel and a multi-FM picket channel.[7] (Details on the phase modulation for multi-FM and other system specifications can be found in Table 134.I.) The main-pulse channel is similar to the NIF front end, including phase modulation at 3 GHz for SBSS and 17 GHz for SSD, although the

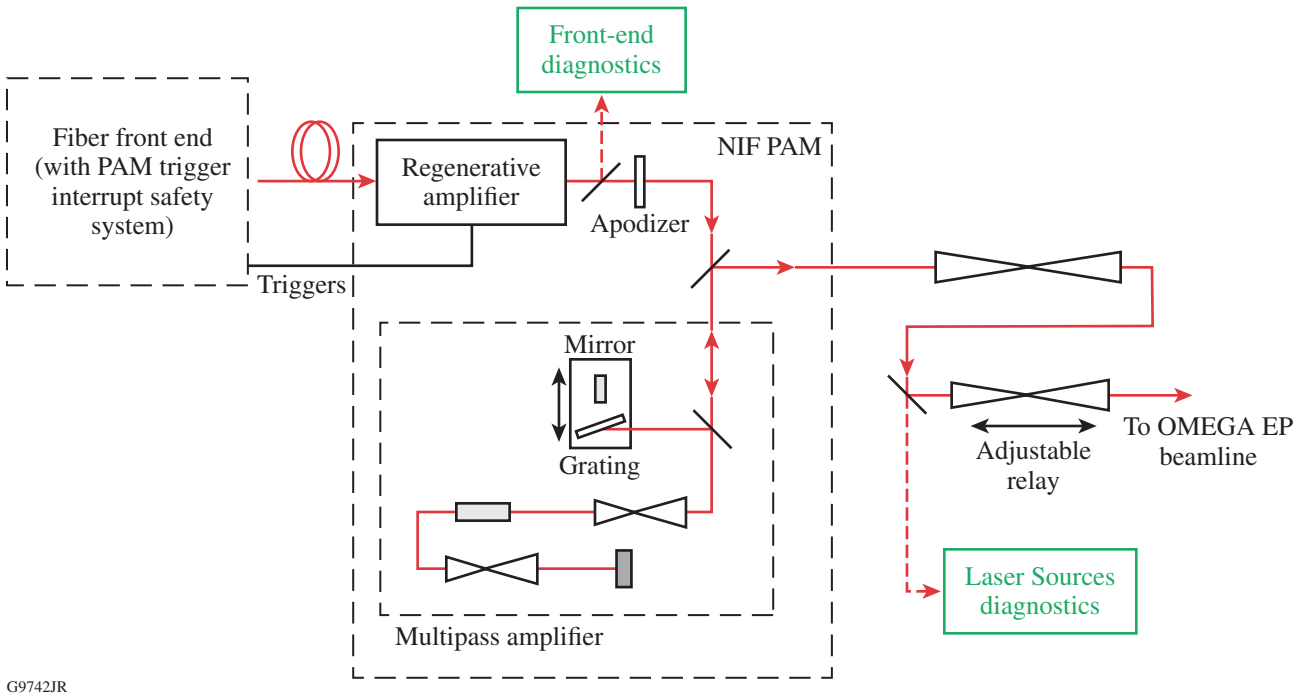

Figure 134.2
Schematic layout of the multi-FM SSD prototype front end. Red lines indicate the optical path, black lines indicate electrical trigger signals, and green blocks indicate laser diagnostics. PAM: preamplifier module.

Table 134.I: Specifications of the multi-FM SSD demonstration system.

Parameter	Value
Modulation frequencies (f_1, f_2, f_3)	21.165, 22.837, 31.881 GHz
Modulation indices (δ_1, δ_2, δ_3)	0.45, 1.04, 2.07 rad
Grating angular dispersion (in PAM), $d\theta/d\lambda$	381.4 μrad/Å
Spectral bandwidth	7.3 Å
Magnification, PAM to beamline	21.5
Temporal skew from pulse-front tilt	229 ps

17-GHz, 1-D SSD phase modulation was not utilized for high-energy shots.

The two channels are fiber optically combined and injected into a NIF preamplifier module (NIF PAM).[8] Pulses are initially amplified to the mJ level in a regenerative amplifier. The fiber front end also contains a system safety feature called the PAM trigger interrupt safety system (PTISS), which monitors the seed pulses and prevents emission of an amplified pulse from the regenerative amplifier in the event of an unsafe condition.[7] Upon exiting the regenerative amplifier, the beam is passed through an apodizer that shapes the edges of the beam and precompensates for spatial-gain variations in the beamline amplifiers. After an image relay, the beam is injected into a multipass amplifier (MPA), where it undergoes amplification to ~500 mJ via four passes through a flash-lamp–pumped, 32-mm-diam × 300-mm-long Nd:glass rod amplifier. The beam is angularly multiplexed in the MPA and passes through a spatial filter with an array of four 5.16-mm-diam pinholes on each pass. After accounting for magnification into the OMEGA EP beamline, these pinhole sizes correspond to a full-angle acceptance of ~200 μrad in the final OMEGA EP beam, making them the tightest pinholes in the system.

A diffraction grating inserted into the MPA after the second pass of the MPA disperses the SSD bandwidth. The 1700-lines/mm gold grating is aligned at the Littrow angle and mounted on a translation stage that also supports a flat mirror. This allows us to translate the mirror into place and operate the system without any angular dispersion of the SSD bandwidth. Note that because phase modulation is performed in a fiber system, there is no pre-shear diffraction grating as found

in most SSD systems. As a result, the dispersing diffraction grating also introduces a pulse-front tilt, or temporal shear, of 229 ps across the beam width.

After exiting the NIF PAM, the beam passes through a set of image relays and is injected into the OMEGA EP beamline. One of the image relays is adjustable to allow for fine control of the image plane's position.

Two sets of beam diagnostics are provided within the multi-FM front-end system. The front-end diagnostics characterize the output of the regenerative amplifier and comprise an energy diagnostic, a spectrometer (<5-GHz resolution), and fast photodetection (45-GHz response) for measuring amplitude noise. The Laser Sources diagnostics, characterizing the beam at the output of the NIF PAM, contain energy diagnostics, cameras that image the near-field and far-field beam profiles, a streak camera that measures the pulse shape, and a setup for measuring the amplitude noise near an image plane of the diffraction grating.

The pulse exiting the Laser Sources Bay is injected into the OMEGA EP long-pulse beamline (illustrated in Fig. 134.3). The OMEGA EP beamline is similar to a folded version of the NIF beamline. The beamline is an angularly multiplexed system in which a pulse undergoes two passes through the seven-disk booster amplifier and four passes through the eleven-disk main amplifier. The transport and cavity spatial filters (TSF and CSF, respectively) are each populated with 300-μrad full-angle pinholes to filter high-frequency spatial modulations on the beam. After undergoing full amplification in the beamline, the pulse exits the TSF and propagates to the frequency-conversion crystals (FCC's), which convert the 1.053-μm beam to the third harmonic. One critical difference from the NIF system is that the FCC's are physically separated from the final focusing optics by 8 m. The final focusing optics include a DPP, a focusing lens (f = 3.4 m), a vacuum window, and a thin debris shield.

Finally, one important consideration for a frequency-converted system with SSD is that the 1ω beam at the input of the frequency conversion should have a minimal amplitude modulation (AM). Because propagation away from the dispersing grating in a SSD system will convert FM to AM, it is beneficial to accurately image the grating to the FCC plane. This was accomplished on OMEGA EP by translating the

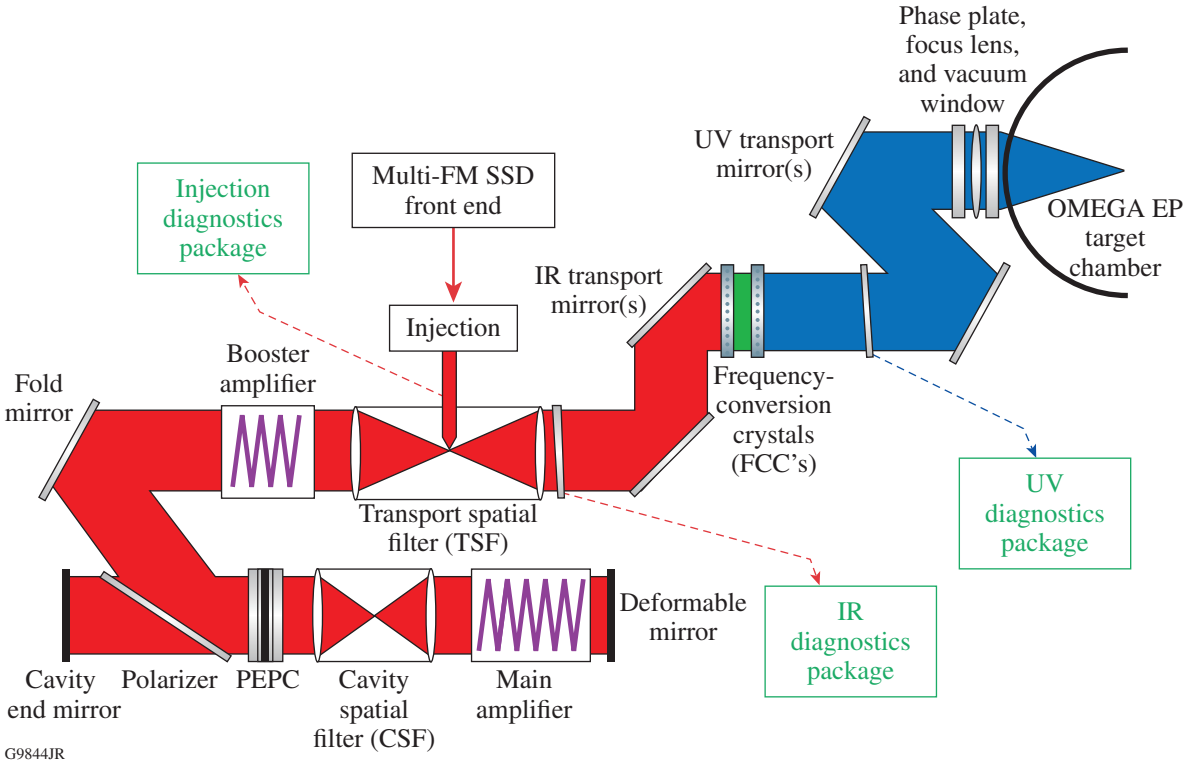

Figure 134.3
Schematic layout of the OMEGA EP long-pulse beamline. PEPC: plasma-electrode Pockels cell.

adjustable image relay in the front end (see Fig. 134.2) to shift the grating image plane onto the FCC's.

Three different diagnostics packages monitor the beam properties at various points in the system. An injection diagnostic package measures the energy, pulse shape, and near-field beam profile of the beam prior to up-collimation into the beamline. At the output of the beamline, the infrared diagnostics package (IRDP) contains diagnostics that measure the energy, near-field and far-field beam profiles, pulse shape, and wavefront of the 1ω amplified beam. Finally, after the frequency conversion, the ultraviolet diagnostics package (UVDP) measures the energy in the first, second, and third harmonics, and the near field, far field, and pulse shape of the 3ω beam. The UVDP also has provisions for inserting a DPP to measure the focal spot at an equivalent target plane.

Amplitude-Modulation Concerns

One of the key concerns with frequency modulation in a high-energy laser system is the generation of high peak intensities caused by AM. FM can be converted into AM by a number of mechanisms.[9] Ideally, a direct AM measurement in the planes of all the optics would ensure that AM is within tolerable levels; however, this measurement would be extremely difficult to make. A streak camera—the deployed pulse-shape diagnostic—does not have sufficient resolution to accurately measure noise at the multi-FM SSD frequencies. Therefore, for this demonstration, our approach was to measure the AM in the front end of the system and produce a budget for further AM in the beamline, based on simulations where possible and on conservative estimates where simulation was impossible. This budgeting process, which resulted in a limit to the peak power that could be safely produced on the system, is described in this section along with the results.

1. Amplitude Modulation in the UV Optics

A model of multi-FM propagation in the final stages of the OMEGA EP system is presented in ***Simulations of the Propagation of Multiple-FM Smoothing by Spectral Dispersion on OMEGA EP*** (p. 85).[10] The model, implemented in the laser simulation code Miró,[11] simulated a pulse with multi-FM SSD, beginning from the final pinhole in the TSF and propagating to the final UV optics at the target-chamber port. The pulse was assumed to be free of AM and to cleanly propagate through this final pinhole, and the SSD diffraction grating was assumed to be well imaged to the FCC plane. Amplitude modulation caused by the frequency-conversion process and propagation away from the FCC's was simulated, and a spatiotemporal model of the pulse intensity was developed for each optic. From this data, the *B*-integral (ΣB) accumulated from the final pinhole through the remaining transmissive optics was calculated. To keep the accumulated ΣB below 2.0 rad, it was determined that the maximum 3ω power on target (in the absence of other sources of AM) should be limited to 1.6 TW. Note that the simulations were performed assuming a grating with a larger dispersion (1800 lines/mm) than was actually used for this commissioning. Using this result as a basis for setting a system performance limit was therefore a conservative approach.

2. Amplitude Modulation via Amplification in the OMEGA EP Beamline

Amplification of the broadband multi-FM pulse can lead to FM-to-AM conversion and therefore must be considered when apportioning a budget for AM in the laser chain. Specifically, we consider the effects of material dispersion, gain narrowing, and phase changes caused by the line shape of the gain medium, referred to as the Kramers–Kronig phase. Additional effects such as etaloning in the system's optics or spectral clipping on the pinholes were not considered because these effects are specific to the optics and alignment of the particular beamline. A broadband, 1-D model of the IR portion of OMEGA EP, including material dispersion of all of the optics, the gain spectrum of the Nd-doped, LHG-8 glass amplifiers, and the phase introduced by this gain spectrum, was developed. Because the multi-FM spectral width is comparable to that of the gain spectrum of the Nd:glass, one expects that gain narrowing and the associated phase effects may alter both the power spectrum and the spectral phase of the multi-FM pulse, thereby producing AM.

Figure 134.4 shows the results of the model described above for a noise-free multi-FM pulse that is injected into the beamline (red). The multi-FM spectrum was created using the parameters shown in Table 134.I. This simulation shows that one can expect some FM-to-AM conversion to take place in the amplifier chain, producing an output pulse with amplitude modulation (blue). Zooming in on the modulation pattern, it is clear that amplification of the FM pulse in the OMEGA EP laser chain will lead to about a 10% peak-to-mean modulation on the pulse as a result of the effects considered in the model. This amount of AM must be included in the modulation budget as will be discussed in the following section.

3. Peak-Power Specification and AM Budget

A budget to allow for a reasonable level of AM accumulation in the OMEGA EP Laser System was developed to specify a peak power. The 1.6 TW determined from the Miró model of the final optics was used as a starting point, and allowances

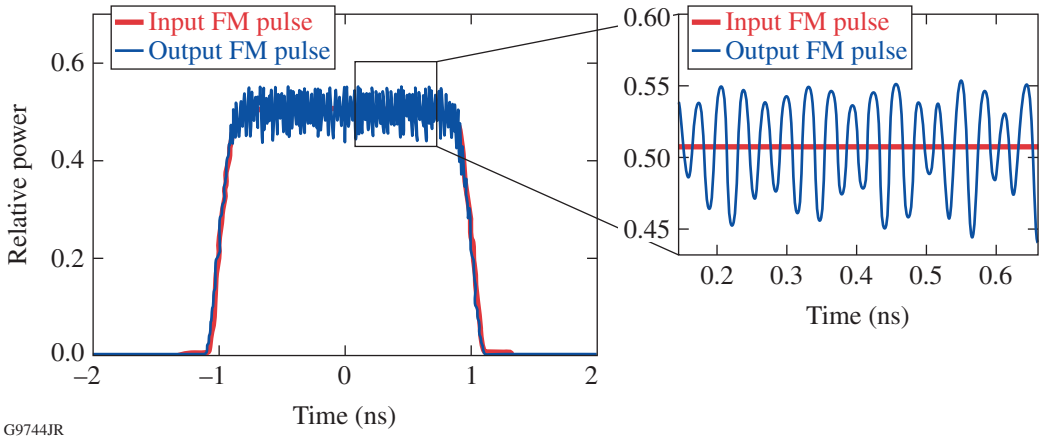

Figure 134.4
Result of a simulation of amplitude modulation in a 1ω pulse introduced by amplification in the OMEGA EP beamline.

were made for other sources of AM. The first of these was AM arising in the beamline (via dispersion, gain narrowing, and the Kramers–Kronig phase), as discussed in **Amplitude Modulation via Amplification in the OMEGA EP Beamline** (p. 78). The second was AM arising from "technical" sources of AM that cannot be predicted via simulation. These include AM arising from etalons, loss of spectrum from clipping on pinholes, etc. Finally, an allowance was made for residual AM in the front end. These sources of AM were assumed to contribute incoherently and were root sum squared to form an overall budget. Finally, a safety margin was applied to allow for both model uncertainties and energy instability in the system. A summary of the AM budget is shown in Table 134.II.

The result of the budgeting process is that the maximum UV on-target power for which OMEGA EP will utilize the multi-FM SSD system is 0.85 TW.

System Integration and Commissioning

1. Spectral Dispersion Concerns in the PAM Spatial Filters

One of the key concerns in limiting AM in the SSD system is to ensure that the spectrum, which is dispersed in the far field as a result of dispersion from the diffraction grating, cleanly passes through the pinholes of the system. The limiting pinholes in the system are in the multipass amplifier in the NIF PAM, i.e., the first pinholes after the diffraction grating. Therefore, the dispersion of the grating was selected to ensure that the beam can propagate through these pinholes without spectral clipping. To evaluate this, the far-field camera in the Laser Sources diagnostics (see Fig. 134.2) was used to image the dispersed spectrum at the output of the PAM and compared to the expected spectrum resulting from the multi-FM modulation. The result is shown in Fig. 134.5.

Inspection of the plot in Fig. 134.5(b) clearly shows that all the significant sidebands of the modulation spectrum can be observed in the output beam and therefore are not being clipped in the pinholes. In fact, under perfect alignment conditions, the pinhole cutoff frequency is given by

$$f_{\text{cutoff}} = \frac{c}{\lambda_0^2} \frac{\theta_{1/2}}{(\mathrm{d}\theta/\mathrm{d}\lambda)_{\text{grating}}}, \tag{1}$$

Table 134.II: Amplitude modulation budget and peak-power specification.

	Allowance	Resulting Peak Power
B-integral in UV optics (Miró model)	—	1.6 TW
AM in front end	15% peak to mean	—
AM introduced in beamline	10% peak to mean	—
Other "technical" sources of AM	20% peak to mean	—
Root-sum-square total	27%	1.17 TW
Safety margin	28%	**0.85 TW**

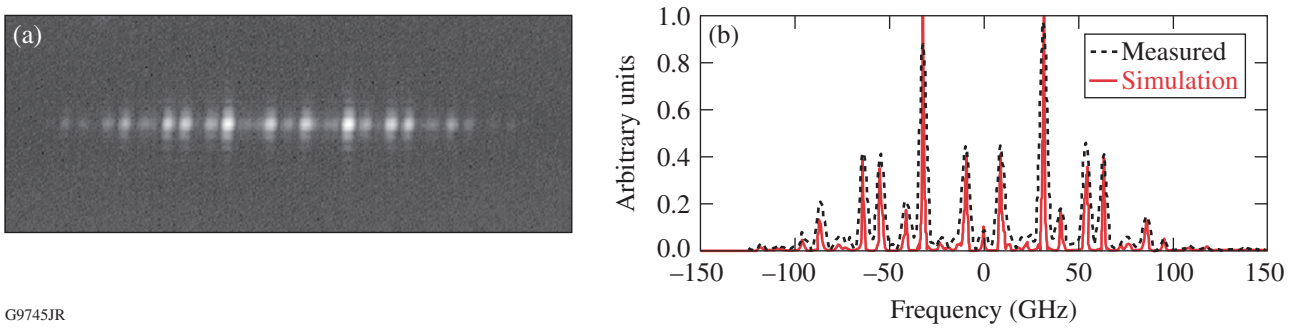

Figure 134.5
(a) Far-field image of the beam exiting the PAM with multi-FM SSD applied. (b) Lineout of the far-field image (black dashed line) with the calculated modulation spectrum superimposed (red solid line), with the far-field camera spatial scale converted to the spectral domain based on the grating dispersion and the magnification to the camera.

where $\theta_{1/2}$ is the acceptance half-angle of the spatial filter (2.07 mrad for the spatial filter with a 1.249-m-focal-length lens and 2.58-mm-radius pinhole), $(d\theta/d\lambda)_{grating}$ is the angular dispersion of the diffraction grating (given in Table 134.I), and λ_0 is the central frequency of the seed source (1053.044 nm). The result is an ideal cutoff frequency of 146 GHz, significantly higher than the highest signal frequency shown in Fig. 134.5. In practice, the pinhole cutoff will be somewhat lower because of misalignment into the spatial filters and between the multiple passes through the MPA. Finally, noise measurements on the beam at the output of the MPA in the Laser Sources diagnostics have confirmed that the AM is below the 15% peak-to-mean allowance in Table 134.II (see Fig. 134.34).

2. Commissioning on OMEGA EP

The commissioning process on OMEGA EP proceeded by initially activating without dispersion of the modulation bandwidth, by removing the diffraction grating from the beam path in the NIF PAM and inserting the mirror (see Fig. 134.2). Each of the two channels (the multi-FM SSD channel and the main-pulse channel) was introduced individually. Initial shots were taken just within the Laser Sources Bay to confirm stability and acceptable beam quality and to develop configurations to produce the appropriate energies. Subsequent shots energy ramped the system first just to the beamline output. Finally, a UV energy ramp to the system limits was undertaken and the picket and main channels were combined. After full-system performance was demonstrated, the diffraction grating was inserted and the system was methodically ramped to full performance. Only the final results are presented herein.

Results from a UV shot near the 0.85-TW system limit using a triple-picket pulse applied to the multi-FM channel (no main pulse) are shown in Fig. 134.6: the near-field beam profiles at the injection [Fig. 134.6(a)]; beamline output [Fig. 134.6(b)]; and the UV output [Fig. 134.6(c)]. The beam quality as shown is comparable to a typical performance on this beamline with the narrowband OMEGA EP front end. The UV pulse shape, calibrated to on-target power [shown in Fig. 134.6(d)], indicates that the shot did, in fact, achieve a peak power of >0.8 TW.

The far-field intensities measured on a multi-FM picket-only shot are plotted in Fig. 134.7. The measured focal spot at the beamline output, from the far-field camera in the IRDP, is shown in Fig. 134.7(a). A lineout of this image along with the simulated dispersion of the modulation spectrum is shown in Fig. 134.7(b). The same measurements at 3ω from the UV far-field camera are shown in Figs. 134.7(c) and 134.7(d). Note that the wavefront error accumulated in the beamline has broadened these focal spots, making the different sidebands of the 1ω spectrum difficult to distinguish in the IR far-field image. The width of the focal-spot lineout is consistent, however, with the width of the simulated spectrum, providing evidence that the spectrum is not clipped by propagation in the beamline.

The 3ω spectrum is by design very complex with a large number of closely spaced sidebands approximating a quasi-uniform modulation spectrum. As a consequence, the far field approximates a continuously blurred version of the narrowband far-field profile, with the blurring applied in one dimension. Note in Fig. 134.7(d) that the width of the far field is consistent with the width of the modulation spectrum, indicating that the full spectrum was frequency converted.

In addition to the triple-picket pulse shape shown in Fig. 134.6(d), a variety of other pulse shapes have been used with the multi-FM SSD source in the process of commissioning. The sample shown in Fig. 134.8 includes a narrow

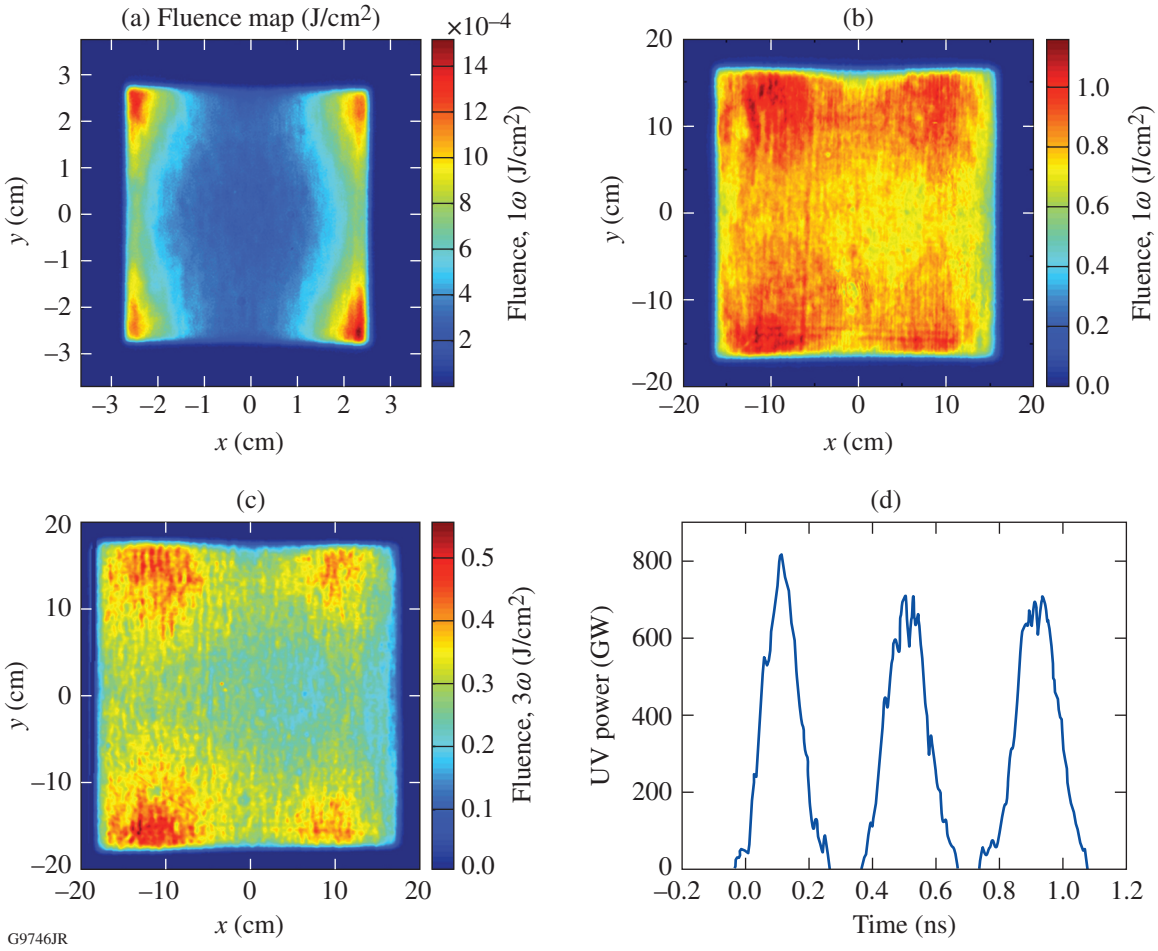

Figure 134.6
Beam profile at various points in the system for a triple-picket multi-FM SSD shot near the system performance limit. Beam profiles as measured by the near-field cameras in the (a) injection diagnostics, (b) IRDP, and (c) UVDP; (d) the UV pulse shape as measured by the streak camera in the UVDP.

150-ps picket [Fig. 134.8(a)], a series of three 650-ps pickets [Fig. 134.8(b)], and a 2-ns square pulse at the system power limit [Fig. 134.8(c)].

3. Demonstration of Beam-Smoothing Performance

Upon completion of the commissioning of the multi-FM SSD demonstration system on OMEGA EP, an experiment was performed to demonstrate the resulting beam smoothing. A DPP, designed to produce a super-Gaussian spot with a 1.1-mm diameter at the target plane, was mounted in the UV diagnostics path. In this configuration, the UV far-field camera measures the fluence distribution in an equivalent target plane. For this experiment, a single 650-ps picket pulse was used.

A baseline measurement was first made with the narrow-bandwidth main-pulse source (with only the 3-GHz SBSS bandwidth applied). To eliminate any dispersion of even this low bandwidth, the PAM diffraction grating was not used and was replaced with the mirror. The resulting target-plane intensity distribution is shown in Fig. 134.9(a). Lineouts through the center of the beam in both the horizontal and vertical directions [shown in Fig. 134.9(b)] indicate a high speckle contrast.

A smoothed beam profile was measured using the identical pulse shape formed with the multi-FM picket seed source. The diffraction grating was reinserted into the beam path in the PAM to provide dispersion of the bandwidth. The smoothed target-plane intensity distribution is plotted in Fig. 134.9(c) and the corresponding lineouts in Fig. 134.9(d). The effect of SSD on the beam profile is clear, with the smoothing being more effective in the horizontal (dispersion) direction, as expected in a 1-D SSD system.

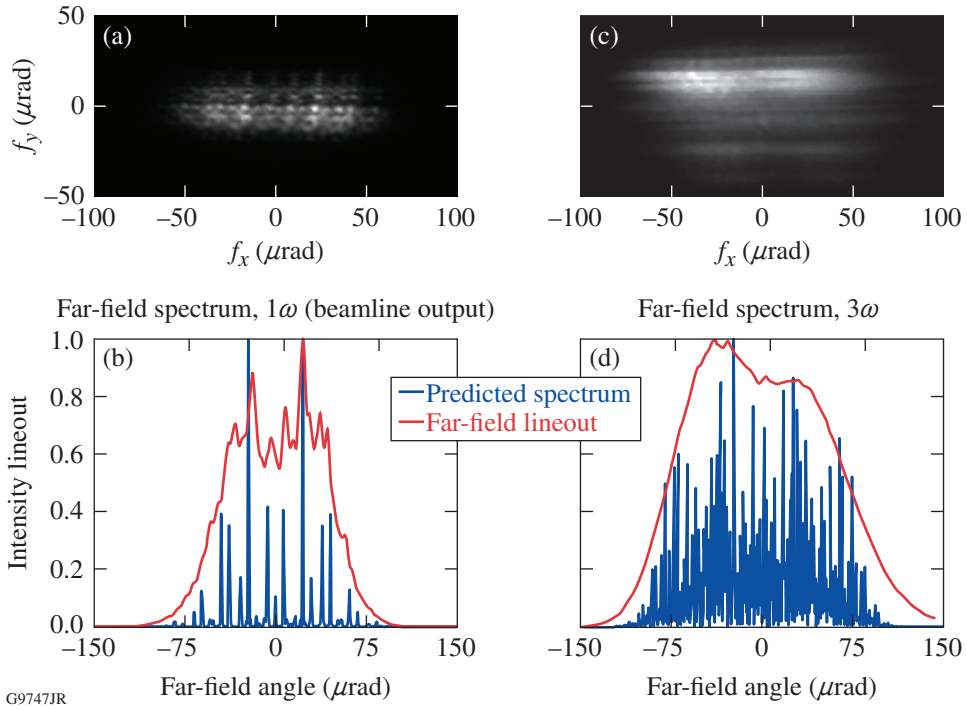

Figure 134.7
Far-field measurements at the [(a) and (b)] IRDP and [(c) and (d)] UVDP for a multi-FM picket shot. [(a) and (c)] The raw images are shown with the scale calibrated to the far-field angle in μrad. [(b) and (d)] The simulated optical spectra are plotted (in blue) along with lineouts from the camera images (red).

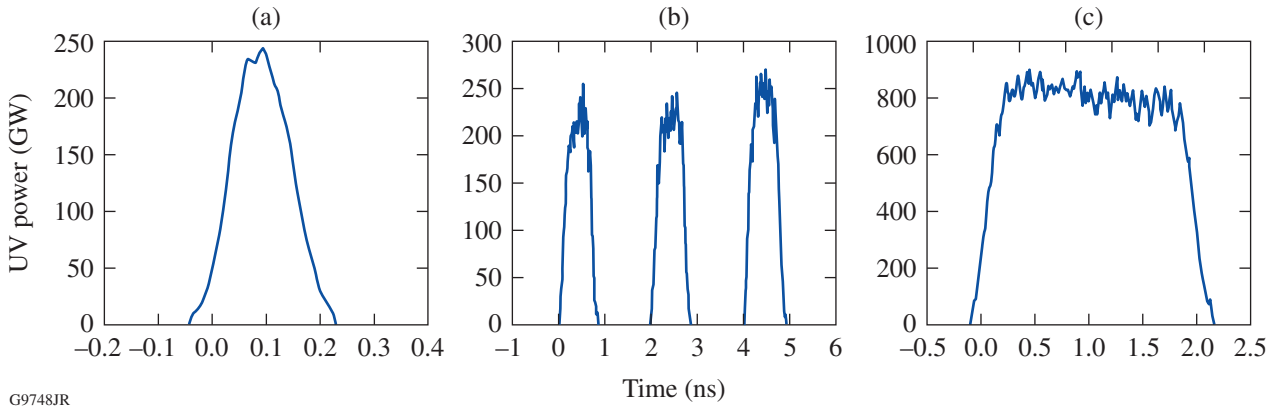

Figure 134.8
UV streak-camera measurements of a variety of multi-FM pulse shapes used during commissioning. (a) A single 150-ps full-width-at-half-maximum (FWHM) picket, (b) a sequence of three 650-ps FWHM pickets, and (c) a 2-ns square pulse.

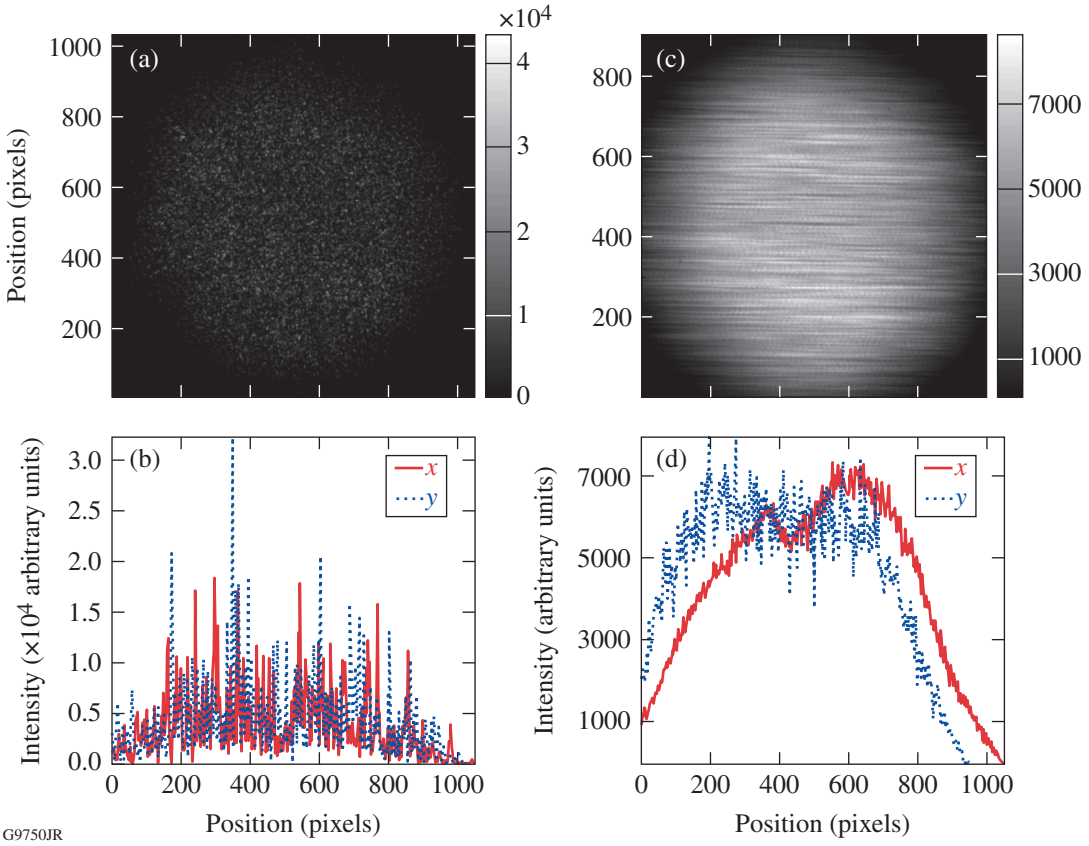

Figure 134.9
Equivalent-target-plane fluence measurements showing beam smoothing caused by multi-FM SSD applied to a 650-ps picket pulse. [(a) and (c)] Fluence profiles and [(b) and (d)] fluence lineouts in the horizontal and vertical directions are plotted for a narrowband main-channel pulse and a multi-FM SSD pulse, respectively.

Conclusion

A prototype multi-FM SSD demonstration system has been successfully commissioned on a long-pulse beamline of the OMEGA EP Laser System. The system utilizes a fiber-based front end with a NIF PAM to deliver dispersed, phase-modulated pulses to the beamline, where the beam is amplified, converted to the third harmonic, and focused on the target after a DPP. A 0.85-TW limit for the peak power delivered to the target using the multi-FM SSD system was derived from a combination of simulating pulsed beam propagation through the UV optics, modeling the beamline gain processes, and budgeting for other potential sources of amplitude modulation. The multi-FM system was operated up to the system power limit using a variety of pulse shapes, and no evidence of spectral loss or beam degradation was observed on the available diagnostics. The beam-smoothing improvement obtained with the multi-FM SSD system was characterized using equivalent-target-plane fluence-profile measurements.

Since commissioning on OMEGA EP, the multi-FM system has been used in a number of target campaigns with the goal of validating the predicted effect on target physics. This work is ongoing, and the system will continue to provide useful data critical to future OMEGA EP experiments and potentially future polar-drive fusion experiments.

ACKNOWLEDGMENT

This work was supported by the U.S. Department of Energy Office of Inertial Confinement Fusion under Cooperative Agreement No. DE-FC52-08NA28302, the University of Rochester, and the New York State Energy Research and Development Authority. The support of DOE does not constitute an endorsement by DOE of the views expressed in this article.

REFERENCES

1. S. Skupsky, R. W. Short, T. Kessler, R. S. Craxton, S. Letzring, and J. M. Soures, J. Appl. Phys. **66**, 3456 (1989).

2. Y. Kato *et al*., Phys. Rev. Lett. **53**, 1057 (1984).

3. *LLE Review Quarterly Report* **114**, 73, Laboratory for Laser Energetics, University of Rochester, Rochester, NY, LLE Document No. DOE/NA/28302-826, OSTI ID 93524 (2008).

4. J. H. Kelly, L. J. Waxer, V. Bagnoud, I. A. Begishev, J. Bromage, B. E. Kruschwitz, T. J. Kessler, S. J. Loucks, D. N. Maywar, R. L. McCrory, D. D. Meyerhofer, S. F. B. Morse, J. B. Oliver, A. L. Rigatti, A. W. Schmid, C. Stoeckl, S. Dalton, L. Folnsbee, M. J. Guardalben, R. Jungquist, J. Puth, M. J. Shoup III, D. Weiner, and J. D. Zuegel, J. Phys. IV France **133**, 75 (2006).

5. G. H. Miller, E. I. Moses, and C. R. Wuest, Opt. Eng. **43**, 2841 (2004).

6. T. J. B. Collins, J. A. Marozas, K. S. Anderson, R. Betti, R. S. Craxton, J. A. Delettrez, V. N. Goncharov, D. R. Harding, F. J. Marshall, R. L. McCrory, D. D. Meyerhofer, P. W. McKenty, P. B. Radha, A. Shvydky, S. Skupsky, and J. D. Zuegel, Phys. Plasmas **19**, 056308 (2012).

7. "Fiber Front End with Multiple Phase Modulations and High-Bandwidth Pulse Shaping," published in this volume.

8. M. Bowers *et al*., in *Solid State Lasers XVI: Technology and Devices*, edited by H. J. Hoffman, R. K. Shori, and N. Hodgson (SPIE, Bellingham, WA, 2007), Vol. 6451, p. 64511M.

9. J. E. Rothenberg, D. F. Browning, and R. B. Wilcox, in *Third International Conference on Solid State Lasers for Application to Inertial Confinement Fusion*, edited by W. H. Lowdermilk (SPIE, Bellingham, WA, 1999), Vol. 3492, pp. 51–61.

10. "Simulations of the Propagation of Multiple-FM Smoothing by Spectral Dispersion on OMEGA EP," published in this volume.

11. O. Morice, Opt. Eng. **42**, 1530 (2003).

Simulations of the Propagation of Multiple-FM Smoothing by Spectral Dispersion on OMEGA EP

Introduction

Smoothing by spectral dispersion[1] (SSD) is a technique that, when coupled with the use of a distributed phase plate (DPP), smoothes on-target laser illumination. The principle is shown in Fig. 134.10. Frequency modulation (FM) at a frequency ω_M is applied to the laser beam. After transiting a diffraction grating, the beam is angularly deflected at ω_M as its instantaneous frequency varies. In the far field of the beam, where the target is positioned, the focal spot is laterally deflected. If the deflection is sufficiently greater than the far-field feature size of a DPP located before the focusing lens, significant smoothing is obtained on a time-averaged basis.

The selection of the appropriate ω_M, grating dispersion $d\theta/d\lambda$, asymptotic smoothing time τ_{asymp}, and DPP feature size is subject to an optimization that depends on the target hydrodynamics and the particular Legendre modes to be reduced.[2] For the work described here, three simultaneous modulation frequencies were optimum,[3] therefore the "multi-FM" nomenclature.

The actual implementation of SSD puts the modulator(s) and the grating in the front end of the laser where the apertures and energies are small, thereby avoiding optical-damage issues and the high cost of large specialty optics such as gratings. This requires, however, the propagation of dispersed FM beams through the amplifier and frequency-conversion sections of the laser. Conversion of this dispersed FM to amplitude modulation (AM) becomes a concern, particularly in the high-energy/high-intensity sections of the laser. There are numerous mechanisms for the conversion of FM to AM,[4] particularly in fiber components. The conversion of FM to AM inherent in free-space propagation is the mechanism of exclusive concern in this article.

FM-to-AM Conversion from Free-Space Propagation

1. Geometrical-Optics Model

Undispersed FM beams, by definition, have no AM. This condition is readily seen by examining the Bessel-function expansion of a single-tone FM signal,[5] $E(t)$:

$$E(t) = A\exp\left[i\omega_0 t + i\delta\sin\left(\omega_M t\right)\right]$$
$$= A\sum_{n=-\infty}^{+\infty} J_n(\delta)\exp\left[i\left(\omega_0 + n\omega_M\right)t\right], \quad (1)$$

where J_n is the nth-order Bessel function, δ is the modulation depth, ω_0 is the optical frequency, ω_M is the modulation (tone) frequency, and A is a constant. Taking the magnitude of Eq. (1) leads to $|E(t)| = A$. Note that this result depends critically on maintaining the phase relationship[6] of each sideband in the

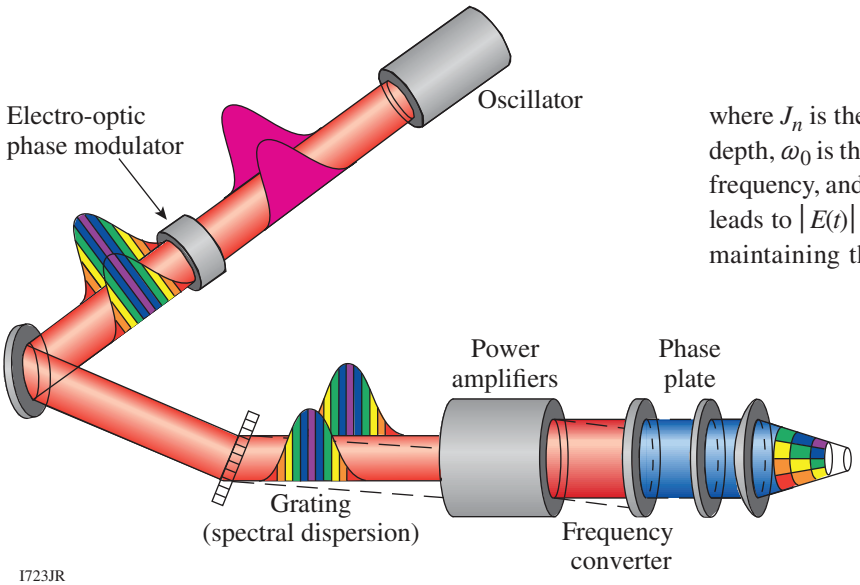

Figure 134.10
The smoothing by spectral dispersion (SSD) concept. Frequency modulation from one or more sequential electro-optic phase modulators is applied to the beam in the front end of the laser system prior to lateral magnification, amplification, and frequency conversion.

Bessel-function expansion. This result may be readily extended to two-tone modulation:

$$E(t) = A\exp\left[i\omega_0 t + i\delta_1\sin\left(\omega_1 t\right) + i\delta_2\sin\left(\omega_2 t\right)\right]$$
$$= A\sum_{n=-\infty}^{+\infty}\sum_{m=-\infty}^{+\infty} J_n\left(\delta_1\right)J_m\left(\delta_2\right)$$
$$\times\exp\left[i\left(\omega_0 + n\omega_1 + m\omega_2\right)t\right] \quad (2)$$

and so on for multitone modulation. The result is the same: as long as the sideband phases are maintained, there is no AM.

The effect of diffraction from the grating is to introduce a dephasing of the sidebands that depends on the sideband frequency, the dispersion of the grating, and the distance from the grating plane. Rewriting Eq. (1) with the grating dispersion in the y direction of a beam propagating in the z direction included yields

$$E(t) = A\sum_{n=-\infty}^{+\infty} J_n(\delta)\exp\left[i\left(\omega_0 + n\omega_{\mathrm{M}}\right)t - i\mathbf{k}_n\bullet\mathbf{r}\right], \quad (3)$$

where $\mathbf{k}_n \bullet \mathbf{r}$ is given by

$$\mathbf{k}_n\bullet\mathbf{r} = \frac{\omega_0 + n\omega_{\mathrm{M}}}{c}\left[\sin\left(\theta_n\right)\mathbf{j} + \cos\left(\theta_n\right)\mathbf{k}\right]\bullet\left(y\mathbf{j} + z\mathbf{k}\right)$$
$$= \frac{\omega_0 + n\omega_{\mathrm{M}}}{c}\left[y\sin\left(\theta_n\right) + z\cos\left(\theta_n\right)\right] \quad (4)$$

with the z direction taken along the propagation direction of the fundamental frequency ($n = 0$, $z = 0$ at the grating), $\mathbf{j}$ and $\mathbf{k}$ being the unit vectors in the y and z directions, the $\mathbf{r}$ vector being the distance from the grating to a point on the beam at coordinates (y,z), and θ_n being the propagation angle of the nth sideband. The angle θ_n is given by

$$\theta_n = \frac{\mathrm{d}\theta}{\mathrm{d}\omega}n\omega_{\mathrm{M}}. \quad (5)$$

Equation (3) demonstrates that for any finite distance from the grating, the sideband n becomes dephased from the pure-FM phasing by the quantity $\mathbf{k}_n \bullet \mathbf{r}$.

In the case of two-tone modulation, Eq. (3) becomes

$$E(t) = A\sum_{n=-\infty}^{+\infty}\sum_{m=-\infty}^{+\infty} J_n\left(\delta_1\right)J_m\left(\delta_2\right)$$
$$\times\exp\left[i\left(\omega_0 + n\omega_1 + m\omega_2\right)t - \mathbf{k}_{n,m}\bullet\mathbf{r}\right], \quad (6)$$

where $\mathbf{k}_{n,m} \bullet \mathbf{r}$ is given by

$$\mathbf{k}_{n,m}\bullet\mathbf{r} = \frac{\omega_0 + n\omega_1 + m\omega_2}{c}\left[y\sin\left(\theta_{n,m}\right) + z\cos\left(\theta_{n,m}\right)\right] \quad (7)$$

and $\theta_{n,m}$ is given by

$$\theta_{n,m} = \frac{\mathrm{d}\theta}{\mathrm{d}\omega}\left(n\omega_1 + m\omega_2\right) \quad (8)$$

and so on for multitone modulation.

Because this dephasing is a function of $\mathbf{r}$, it leads to not only temporal AM but also spatial AM. Chuang[7] developed an analytic expression for the spatiotemporal AM from a single modulator in the geometrical-optics approximation. In the case of free-space propagation, the intensity $I(y,z,t)$ in a plane at a distance z from the grating is given by[7]

$$I\left(y,z,t\right) = \frac{I_0}{\left\{1 + \dfrac{\delta\beta^2 z}{k_0}\sin\left[\omega_{\mathrm{M}}t + \beta y_0\left(y,z,t\right)\right]\right\}}, \quad (9)$$

where I_0 is the intensity at the grating plane (assumed to be at $z = 0$) and y_0 is the y location of the ray being traced at $z = 0$. Note that since the beam has not yet propagated any distance, I_0 will have no SSD-induced time variation or y- (dispersion) direction variation. The quantity β is the grating-induced shear in radians per unit transverse length in the dispersion direction at the modulation frequency ω_{M}. A straightforward calculation of the shear[8] yields

$$\beta = 2\pi\frac{\mathrm{d}\theta}{\mathrm{d}\lambda}\frac{\omega_{\mathrm{M}}}{\omega_0}. \quad (10)$$

The result in Eq. (9) is valid where diffraction effects are negligible. Since some regions of I_0 will have positive phase curvature (i.e., be focusing), there will exist a critical distance z_r at which the intensity goes to infinity (i.e., a caustic exists) in

the geometrical-optics approximation and Eq. (9) is no longer valid. This is trivially seen by inspecting the denominator in Eq. (9). At

$$z = z_r = \frac{k_0}{\delta\beta^2} \tag{11}$$

the denominator of Eq. (9) is equal to zero where the sine function is equal to –1. The distance z_r is termed the "critical distance."

It is more physically intuitive to derive this result from a wavefront curvature standpoint. This is shown in Fig. 134.11. From Eq. (4) we may write the expression for the wavefront in terms of either the phase ϕ or the optical path difference (OPD) z as:

$$\begin{aligned} \phi &= \delta \sin\left(\omega_{\mathrm{M}} t + \beta y\right), \\ z &= \frac{\delta}{k_0} \sin\left(\omega_{\mathrm{M}} t + \beta y\right). \end{aligned} \tag{12}$$

The critical distance z_r is calculated by applying the expression for the radius of curvature of an arc at the point $\omega_{\mathrm{M}} t + \beta y = -\pi/2$ where the wavefront is focusing:

$$z_r = \left. \frac{\left[1 + \left(\mathrm{d}z/\mathrm{d}y\right)^2\right]^{3/2}}{d^2 z/dy^2} \right|_{\omega_{\mathrm{M}} t + \beta y = -\pi/2}. \tag{13}$$

Inserting the expression in Eq. (12) for the OPD z into Eq. (13) yields

$$\begin{aligned} z_r &= \left. \frac{k_0 \left\{ 1 + \left[\frac{\delta\beta}{k_0} \cos\left(\omega_{\mathrm{M}} t + \beta y\right) \right]^2 \right\}^{3/2}}{-\delta\beta^2 \sin\left(\omega_{\mathrm{M}} t + \beta y\right)} \right|_{\omega_{\mathrm{M}} t + \beta y = -\pi/2} \\ &= \frac{k_0}{\delta\beta^2} \end{aligned} \tag{14}$$

for the critical distance. The critical distance z_r plays the same role as a focal length in geometrical optics. As such, the usual geometrical-optics formulae may be applied to it.

For distances $z < z_r$, the model in Eq. (9) can be used to visualize the spatiotemporal modulation related to the propagation of SSD. The case of a 1.054-μm-wavelength, 0.75-ns × 10-cm FWHM (full width at half maximum) Gaussian pulse modulated at 10 GHz, $\delta = 4$ rad with 60-Å/μrad dispersion is shown in Fig. 134.12. Note that a similar plot of the intensity versus

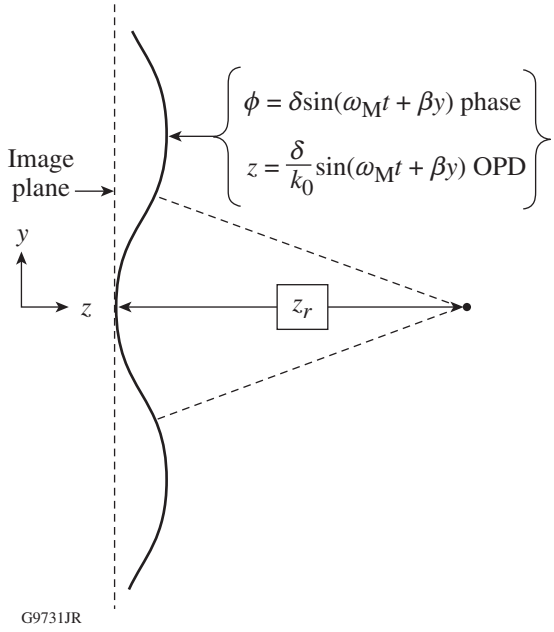

Figure 134.11
Schematic of the calculation of the critical distance z_r, from the local radius of curvature of the phase front. The usual formula for the curvature of an arc is applied to the expression for the optical path difference (OPD) at the location of positive phase curvature or $\omega_{\mathrm{M}} t + \beta y = -\pi/2$.

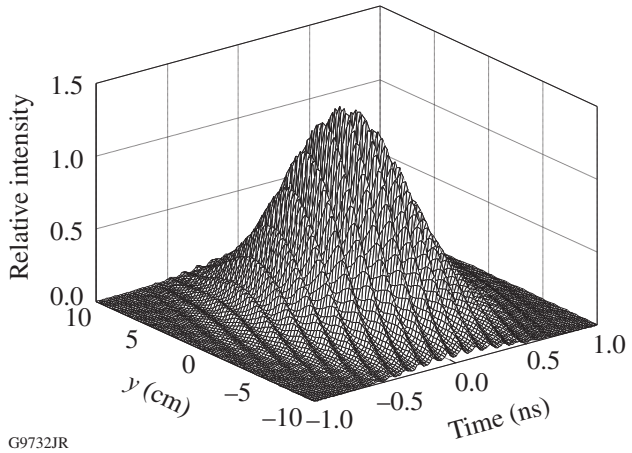

Figure 134.12
Relative intensity 2000 cm from the grating for a 0.75-ns × 10-cm FWHM Gaussian pulse phase modulated with δ = 4 rad at 10 GHz with 60-Å/μrad dispersion. This is a replot of Fig. 6-2 in Chuang's thesis.[7]

x,t rather than y,t would show no modulation. It is worth noting that for this particular example, $z = 2000$ cm and $z_r = 6800$ cm; therefore the geometrical-optics condition for validity is well satisfied. The ratio of $z/z_r \sim 0.3$ is typical of the ranges of interest for large laser systems. Figure 134.13 displays lineouts in the temporal and spatial dispersion directions. The intensification relative to the unmodulated beam becomes of concern in those regions of a laser where the beam is close to the coating-damage, self-focusing, or stimulated-scattering limits.

From Eq. (9) an expression may be written for the normalized peak-to-valley amplitude modulation α, assuming that the slowly varying envelope is removed:

$$\alpha(z) = \frac{I_{\max} - I_{\min}}{(I_{\max} + I_{\min})/2} = \frac{2\delta\beta^2 z}{k_0}. \tag{15}$$

From Eq. (15) it is seen that the normalized peak-to-valley modulation, in the geometrical-optics limit, is proportional to the propagation distance z, the modulation index δ, and the square of the shear β.

2. Linear-Dispersive-Filter Model

Hocquet *et al.*[9] developed a similar metric termed a "distortion criterion" for temporal AM caused by SSD propagation away from a grating. Starting with the concept of free-space propagation as a linear dispersive filter,[10] the temporal Fourier transform of the electric field, $E(z,\omega)$, at a distance z from a grating is written as

$$E(z,\omega) = E_0(\omega)\, H(z,\omega), \tag{16}$$

where $H(z,\omega)$ is a Fourier-domain transfer function. In the case of a grating, this transfer function is a phase-only filter. The phase can be expanded in a Taylor series in ω of which the quadratic component ϕ_2, the quadratic spectral phase, is the first term of interest for AM calculation. Assuming ϕ_2 is small, the transfer function is written as

$$H(z,\omega) = \left[1 - \frac{i}{2}\phi_2(z)\,\omega^2\right]. \tag{17}$$

Substituting Eq. (17) into Eq. (16) and using Eq. (1) for $E_0(\omega)$ and then inverse transforming and taking the magnitude of the resulting inverse transform yields

$$I(z,t) \approx 1 - \phi_2(z)\,\delta\omega_M^2 \cos(\omega_M t). \tag{18}$$

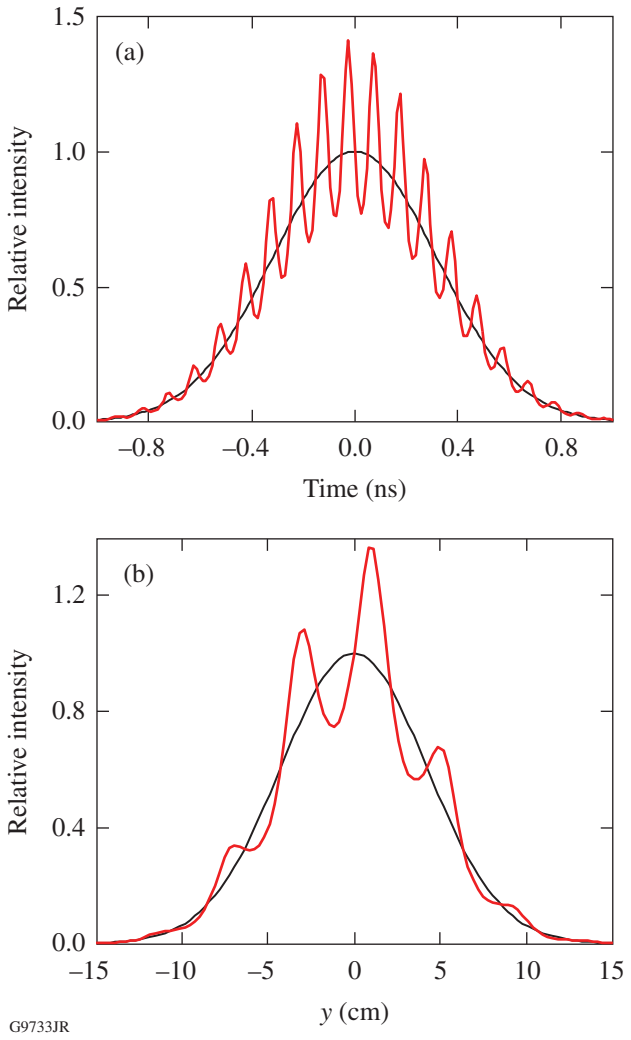

Figure 134.13
Lineouts (red line) in the temporal direction at $(x,y) = (0,0)$ and in the y (dispersion) direction at $x = 0$ and $t = 0$ of the relative intensity shown in Fig. 134.12. In both plots the unmodulated beam profile is also shown to illustrate the local intensification (black line).

Hocquet defines the "distortion criterion" α as in Eq. (15). The values of $I_{\max}$ and $I_{\min}$ obtained by substituting ±1 for the extrema of the cosine function in Eq. (18) lead to

$$\alpha(z) = 2\frac{1 + \phi_2(z)\,\delta\omega_M^2 - 1 + \phi_2(z)\,\delta\omega_M^2}{1 + \phi_2(z)\,\delta\omega_M^2 + 1 - \phi_2(z)\,\delta\omega_M^2}$$

$$= 2\phi_2(z)\,\delta\omega_M^2. \tag{19}$$

Substituting Chanteloup's[11] expression for the quadratic part of the spectral phase $\phi_2(z)$ at $y = 0$, the center of the beam, into Eq. (19) yields

$$\alpha(z) = \frac{2(2\pi)^2 cN^2}{\omega_0^3 \cos^2(\theta_0)} \delta\omega_M^2 z, \tag{20}$$

where a grating at Littrow angle θ_0 and a linear groove density of N per unit length have been assumed. Applying the expression for the dispersion of a grating at the Littrow angle

$$\left.\frac{d\theta}{d\lambda}\right|_{\theta=\theta_0} = \frac{N}{\cos(\theta_0)} \tag{21}$$

in Eq. (10) and substituting $k_0 = \omega_0/c$, Eq. (20) is seen to be identical to Eq. (15), which is Chuang's result.[7] The geometrical-optics and linear-dispersive-filter models, using completely different approaches, lead to the same result for the normalized peak-to-valley amplitude modulation. We choose to continue with Chuang's result since it provides a spatiotemporal description of the pulse intensification resulting from SSD propagation that may be readily compared to numerical models.

3. *B*-Integral Considerations

The so-called *B*- or "breakup" integral is an important measure of the transverse stability of a high-intensity beam. Physically, it is the integral of the local phase pushback in radians caused by propagation of the beam through media of thickness L with a positive χ^3. By definition, it is

$$B \triangleq \frac{2\pi}{\lambda}\int_0^L \gamma I(x,y,z,t)\,dz, \tag{22}$$

where γ is a characteristic of the material.[12] In large laser systems, values of B in excess[13] of 2.0 to 2.2 rad between spatial filters can lead to catastrophic small-scale self-focusing of the beam. Laser-performance limits, particularly for temporally short pulses that do not experience significant gain saturation, are determined by the requirement to limit B. This is known as the "peak-power limit."

During laser design, the *B*-integral is calculated using the average local intensity; that is, transverse small-scale features that would be eliminated in a spatial-filtering operation are averaged out prior to computing B. In a system with SSD applied, the pinholes are carefully sized to ensure passage of the dispersed beam (at least to the Carson[14] limit = $2\delta\omega_M$) through the system. The local intensification on any optical component induced by the propagation of SSD therefore needs to be carefully included in the calculation of the system's peak-power limit.

Modeling

LLE's OMEGA EP laser is a multipass-architecture laser similar to that of the National Ignition Facility (NIF)[15] with important differences to optimize it for its primary mission of radiography of cryogenic implosions on the OMEGA laser[16] and separate flat-target experiments. The laser is shown schematically in Fig. 134.14. The multipass cavity formed by the end mirror and the deformable mirror is identical to that of the NIF. The input–output arm containing the booster amplifier is different, however, than that of the NIF. Because the beam-path distance to OMEGA EP's UV target chamber is significantly shorter than that to the NIF's (80 m versus ~140 m from the fold mirror to the target), the transport spatial filter is shorter. OMEGA EP's frequency-conversion crystals (FCC's) are located 8.1 m in front of the *f*/6.5, UV focus lens with a 3.4-m effective focal length. The most-damage-threatened component, the 4.0-cm-thick fused-silica vacuum window, is located 25 cm downstream of the focus lens in the converging beam. The distributed phase plate (DPP) is located 20 cm in front of the focus lens.

Unlike on the NIF, the 11-mm-/9-mm-thick, type-I/type-II, KDP/KD*P frequency-conversion crystals are located on the floor upstream of the focus lens. The IR input polarization is vertical. The SSD dispersion direction is in the sensitive direction of the doubler (horizontal) at the FCC's.[17] The sign of the dispersion is chosen to compensate the frequency detuning[18] at the FCC's. A more-optimal choice, in terms of conversion efficiency, would have the dispersion direction in the sensitive direction of the tripler. The two UV transport mirrors immediately following the UV diagnostic beam splitter (DBS) are dichroic and strip residual 1ω and 2ω light from the beam so that only UV light is delivered to the focus lens.

Frequency conversion is an intensity-dependent nonlinear process that can increase amplitude modulation, particularly if operating in an unsaturated input intensity regime like the 11-mm-/9-mm-thick OMEGA EP FCC's. Since amplitude modulation from SSD propagation is minimized at the actual SSD grating and its image planes, the FCC's are located at a grating image plane. In the simulation, this is accomplished by translating the SSD grating in the front end of the system in the axial direction to make use of the large longitudinal magnification[19] $M \sim 400$ ($M = m^2$, where m is the lateral magnification) of the system to shift the image. Magnification differs in the horizontal and vertical directions at least in part because of the large number of multipass tilted slabs.[20] Detailed ray-trace models of the system were used to set the SSD grating image on the FCC's.

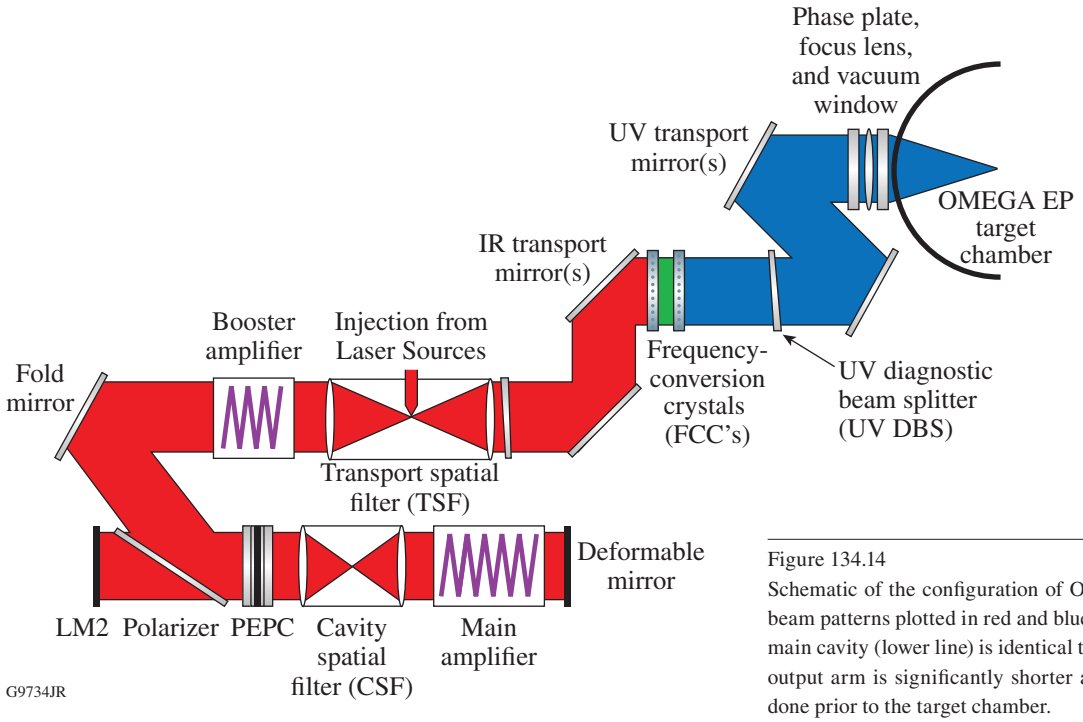

Figure 134.14
Schematic of the configuration of OMEGA EP with IR and UV beam patterns plotted in red and blue respectively. The multipass main cavity (lower line) is identical to that of the NIF. The input–output arm is significantly shorter and frequency conversion is done prior to the target chamber.

The multi-FM temporal pulse shape consists of one to three "pickets" in front of a main compression "drive" pulse. A typical shape is shown in Fig. 134.15. Multi-FM SSD is applied to only one or more of the pickets; the system is capable of applying 17-GHz, single-FM SSD modulation to the drive pulse.[21] Although the available 17-GHz, single-FM SSD was not applied to the drive pulse for the majority of the demonstration shots, δ = 5.5 of 3.0-GHz stimulated Brillouin scattering suppression (SBSS) modulation was applied to the drive pulse for all the demonstration shots. The bulk of the on-target smoothing benefit is obtained prior to the second picket.[2] The pickets themselves have a UV FWHM of 150 ps.

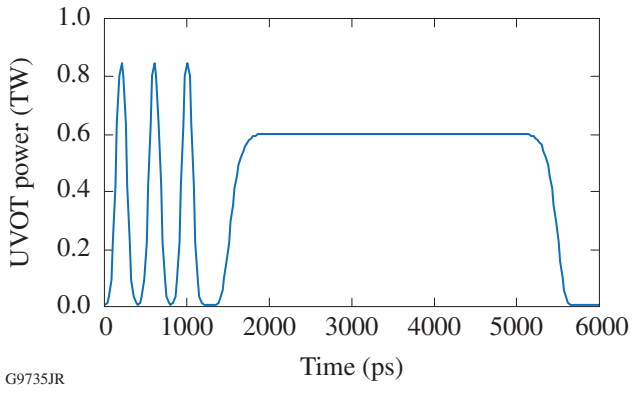

Figure 134.15
Unsheared UV on-target (UVOT) pulse shape. The three pickets are followed by a main drive pulse.

The pickets shown in Fig. 134.15 are temporally short (150-ps FWHM in the UV, ~175 ps in the IR) compared to the main pulse. Because of their short pulse width, as these pickets increase in energy, they represent a peak-power threat to the system rather than an optical coating damage–fluence threat. It is therefore necessary to calculate the maximum *B*-integral attained at any spatiotemporal point in the pulse to assess the threat to the system. In order to do that for the complicated actual case of three modulators and laser system components including frequency conversion, the propagation code Miró is used.

Miró is a comprehensive laser design and simulation code developed[22,23] at CEA/CESTA, France. Miró models typical high-peak-power laser components and operations such as (but not limited to) free-space propagation, amplifiers, frequency converters, and gratings. Consistent with the progressively increasing levels of sophistication in the typical design process of high-peak-power lasers, Miró offers increasing levels of modeling sophistication in the form of "modes" of calculation starting with basic one-dimensional (1-D) ray tracing up to full diffraction calculation that includes broad-spectrum propagation with group-velocity dispersion.

For these simulations of multi-FM SSD, Miró's "broad spectrum" mode and "inhomogeneous wave" grid transformation are used to render the problem computationally tractable. (For

more details, refer to the Miró V5$_\varepsilon$ Reference Manual.[24]) To ensure that the SSD model was being set up correctly in Miró, the analytical case of Chuang in Fig. 134.13, was first simulated. The results are shown in Fig. 134.16. The close agreement between the Miró prediction and the analytical treatment of Chuang gives confidence that the Miró SSD model has been constructed correctly and can be confidently used to predict AM in the region where $z < z_r$.

Since the expected picket energies are low (~100 J) and the beam areas are large (~1200 cm^2), the picket fluence (~0.08 J/cm^2) is low compared to the equivalent (beam-normal) saturation fluence of the system (~5.7 J/cm^2). The pickets are therefore in the small-signal–gain regime and their highest intensities are attained after the booster (final) amplifier, which has a small-signal gain of ~6. The highest B-integral, which is essentially an intensity/length product, is in the section of OMEGA EP downstream from the transport spatial filter to the target with the most-threatened component being the vacuum window on the target chamber. The relevant part of OMEGA EP is shown in Fig. 134.17.

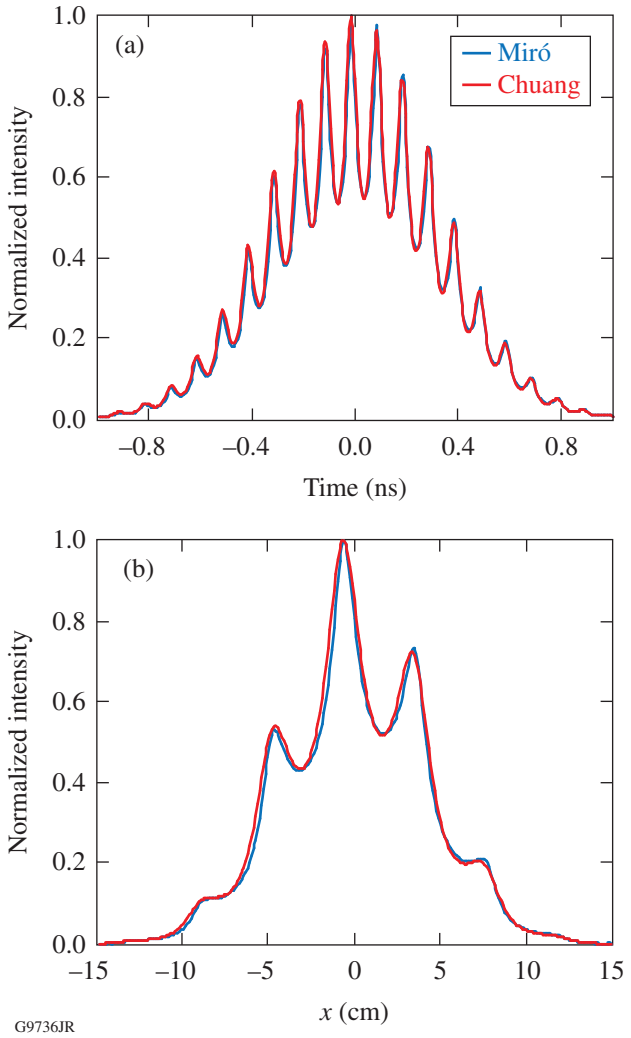

Figure 134.16
Lineouts of the relative intensity predicted by Miró (blue line) in the (a) temporal and (b) spatial directions for the case of Fig. 134.13 compared to the predictions of the Chuang model (red line) with δ = 4 rad at 10 GHz and 60-Å/μrad dispersion. This is at a distance from the grating of 2000 cm compared to z_r = 6800 cm.

The three modulation frequencies applied to the beam are detailed in Table 134.III. These modulation frequencies and their modulation depth have been chosen for optimal smoothing.[25] If the grating-induced beam shear across the nominal w = 35-cm beam width is given by

$$\Delta t = w \frac{2}{c} \tan(\theta), \tag{23}$$

where θ is the angle of incidence on the grating (assumed to be at Littrow), then writing tan(θ) in terms of the dispersion dθ/dλ yields

$$\Delta t = \frac{w\lambda}{c} \frac{\mathrm{d}\theta}{\mathrm{d}\lambda} = 360 \text{ ps} \tag{24}$$

for the temporal shear introduced by an 1800-lines/mm diffraction grating.

The phasing of the modulators in the Miró model is important to ensure that the *maximum* intensification is calculated. The 22.8- and 31.9-GHz modulators impart the most bandwidth to the beam and therefore the most local phase curvature. These modulators have a 9.1-GHz frequency difference, so near-maximum local wavefront curvatures can be expected in any pulse longer than ~110 ps. For this reason the modulators are modeled as *co*-sinusoidal modulators with zero relative phase and t = 0 is centered on the picket.

Table 134.III: FM parameters for the multi-FM SSD system on OMEGA EP.

Modulator	1	2	3
Frequency (GHz)	21.165	22.838	31.881
IR modulation depth (radians)	0.450	1.040	2.071
IR bandwidth (Å)	0.7	1.8	4.9
IR dispersion (μrad/Å)	29.3	29.3	29.3
β (m^{-1})	136.9	147.7	206.3
z_r (m)	707.9	263.1	67.8

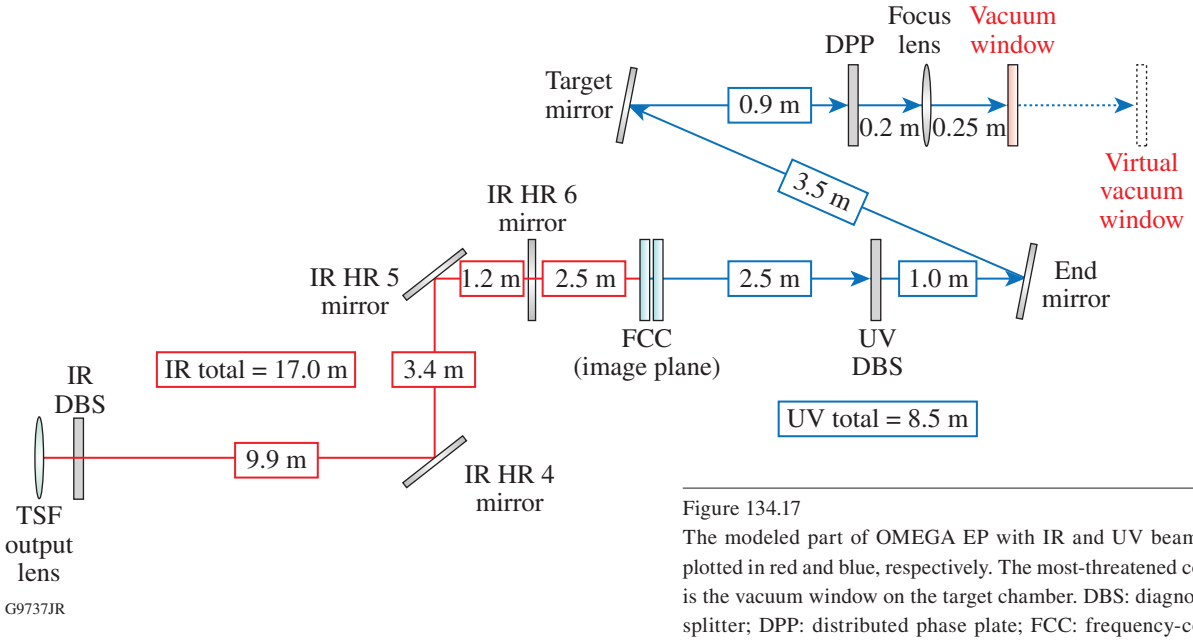

Figure 134.17
The modeled part of OMEGA EP with IR and UV beam patterns plotted in red and blue, respectively. The most-threatened component is the vacuum window on the target chamber. DBS: diagnostic beam splitter; DPP: distributed phase plate; FCC: frequency-conversion crystal; TSF: transport spatial filter; HR: high reflector.

To minimize amplification of AM in the frequency-conversion process, the SSD grating was carefully imaged onto the FCC's.[26] The component located the farthest from the image plane of the grating will experience the greatest intensification as a result of propagation. From Fig. 134.17 it is clearly seen that these components are the IR diagnostic beam splitter and the transport spatial filter's (TSF's) output lens upstream of the image plane and the vacuum window downstream of the image plane. The TSF output lens is ~17 m from the image plane. When calculating the expected intensification, it is useful to first estimate how close the caustic is approached. To do that, the concept of critical distance z_r must be extended to a multifrequency-modulated beam. Recall from the discussion surrounding Fig. 134.11 that z_r is the radius of curvature of the wavefront caused by one modulation. At points in space and time where the frequency modulations are in phase, the resulting phase curvature is the sum of the individual phase curvatures. The thin-lens law[27] for two thin lenses in contact may be applied to add the phase curvatures where $1/f$ is the power of a lens of focal length f

$$\frac{1}{f_1}+\frac{1}{f_2}+\frac{1}{f_3}=\frac{1}{f_{\text{total}}} \tag{25}$$

to obtain

$$\frac{1}{z_{r,1}}+\frac{1}{z_{r,2}}+\frac{1}{z_{r,3}}=\frac{1}{z_{r,\text{total}}}, \tag{26}$$

where $z_{r,i}$ is the critical distance corresponding to the ith modulation. Using Eq. (26) it is immediately found that $z_{r,\text{total}}$ for this system is 50.1 m and the TSF output lens, 17 m from the image plane, is far from the caustic and in the region ($z/z_r \sim 0.34$) where the Miró SSD model has been tested.

The vacuum window is in the UV section of OMEGA EP. The critical distance for the UV beam is required. Recall from Fig. 134.11 that

$$z_r=\frac{k_0}{\delta\beta^2}=\frac{k_{0,\text{IR}}}{\delta_{\text{IR}}\beta_{\text{IR}}^2}=\frac{k_{0,\text{UV}}/3}{\left(\delta_{\text{UV}}/3\right)\beta_{\text{UV}}^2}=\frac{k_{0,\text{UV}}}{\delta_{\text{UV}}\beta_{\text{UV}}^2} \tag{27}$$

because the propagation vector k_0 triples after tripling to the UV ($k_{0,\text{UV}} = 3k_{0,\text{IR}}$), the modulation index δ is increased by a factor of 3 ($\delta_{\text{UV}} = 3\delta_{\text{IR}}$), and the grating-induced shear in radians β at the modulation frequency is unchanged ($\beta_{\text{UV}} = \beta_{\text{IR}}$). Equation (27) implies that for a single modulation, z_r is unchanged under frequency conversion. This is expected since the local wavefront radius of curvature is not expected to be changed by frequency conversion.[28] By Eq. (26) this also holds

for z_{total}. The vacuum window is located a physical distance of 8.5 m from the image plane and is therefore also far from the caustic and in the region where the Miró SSD model has been tested.

A screen shot of the Miró model used for these simulations is shown in Fig. 134.18 with the source shown in the lower left. The modeled beam was temporally 450 ps long and had an experimentally measured temporal profile. This is longer than the actual pickets propagated in the system and was chosen to ensure that multiple cycles of all three modulators were at the maximum intensity of the pulse shape. The spatial shape of the 1ω beam was a 20th-order, square super-Gaussian with 35-cm FWHM. The grid size for these simulations was $16 \times 384 \times 1024\,(x \times y \times u)$, where y is the dispersion direction and u is the "inhomogeneous wave"[29] transformed grid coordinate.

The IR phase modulators and the reflection grating used in the model to disperse the beam are in the lower left. To reduce the model's complexity and therefore computation time, the model's phase modulation and SSD dispersion were applied at the 40-cm aperture (35-cm-sq beam). This required a model grating with 289.57 lines/mm used at its Littrow angle of 8.78° for λ = 1.054 μm. The distance in the model from the reflection grating to the cavity end mirror was adjusted to ensure the grating was imaged onto the mid-plane of the FCC's.

Although the booster amplifier disks are included in the Miró model for future work, they are modeled as zero-B-integral, unity-gain optics to reduce computation time. The main laser cavity, including the cavity spatial filter (CSF), is modeled as a two-pass instead of the actual four-pass to model the imaging of the cavity while again reducing model computation time. All components in this early part of the laser have their nonlinear coefficient γ set to zero. All components from the TSF pinhole onward have their γ's specified to ensure B is accurately calculated. The γ's for the optical materials in OMEGA EP at their use wavelengths are detailed in Table 134.IV.

Three components have more than one wavelength on them simultaneously: the KDP doubler, the KD*P tripler, and the fused-silica UV diagnostic beam splitter. The IR B contributed by the doubler consists of the B as a resuslt of the IR beam itself and the cross-phase-modulation contribution caused by the 2ω beam on the IR beam. Similarly, its 2ω B contribution is the B attributed to the 2ω beam itself plus the cross-phase–modulation term contribution attributed to the IR beam. Where there are three wavelengths present as in both the tripler and the UV diagnostic beam splitter, the calculation is generalized for three waves. The actual calculation proceeds by finding the temporal maximum of the intensity and then calculating the B through the crystal by a split-step method.

The preceding calculates the *contribution* of the particular crystal to the B-integral. The B-integral at each harmonic does not start at a zero value and must be initialized.[30] For the doubler, the conservative assumption is made that the initially small divergence added to the fundamental frequency beam by nonlinear ripple growth (B) is completely transferred to

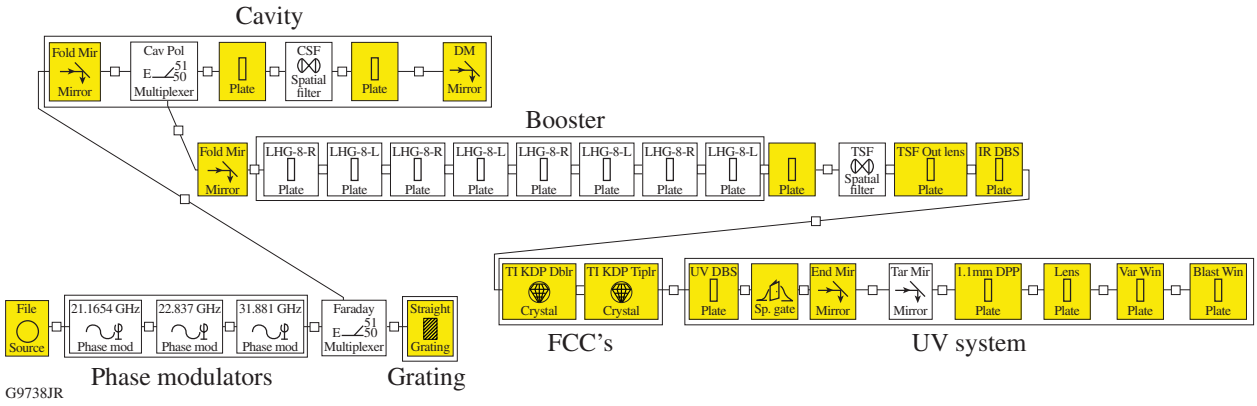

Figure 134.18
The OMEGA EP Miró model. The IR phase modulators are in the lower left. A reflection grating was used in the model to disperse the beam at the 40-cm aperture. Although the booster amplifier disks are included in this model, they are modeled as zero-B-integral, unity-gain plates to reduce running time.

Table 134.IV: Nonlinear coefficients (γ) for OMEGA EP components.

Component	Wavelength	Material	Thickness (cm)	γ (cm^2/GW)
TSF output lens	IR	fused silica	5.6	2.7×10^{-7}
Diagnostic beam splitter	IR	fused silica	1.0	2.7×10^{-7}
KDP doubler	IR and 2ω	KDP	1.1	2.5×10^{-7}
KD*P tripler	IR, 2ω, and UV	KD*P	0.9	3.0×10^{-7}
Diagnostic beam splitter	IR, 2ω, and UV	fused silica	1.0	3.88×10^{-7}
Distributed phase plate	UV	fused silica	4.0	3.88×10^{-7}
Focus lens	UV	fused silica	4.0	4.00×10^{-7}[(a)]
Vacuum window	UV	fused silica	4.0	4.86×10^{-7}[(a)]
Free space	IR or UV	air	various	5.0×10^{-10}

[(a)]The component values have been increased to account for other effects.

the harmonic beam(s). By this assumption the initial B of the second harmonic (2ω) is simply set equal to the B of the fundamental beam.

The case of frequency tripling, which involves the mixing of two different frequencies, is more complicated. In this case Miró makes use of a phenomenological expression for the transmission T of a spatial filter[31] as a function of the B-integral B, and an experimentally determined "noise parameter" ε, for the system under consideration:[32]

$$T(B) = 1 - \frac{\varepsilon}{2}\left[\left(1 + 2B^2\right) + \cosh\left(2B\right)\right]. \tag{28}$$

The loss L in transiting the spatial filter is from Eq. (27):

$$L(B) = \frac{\varepsilon}{2}\left[\left(1 + 2B^2\right) + \cosh\left(2B\right)\right]. \tag{29}$$

Miró postulates that these losses, weighted by frequency (energy), are conserved in frequency conversion. This is roughly equivalent to postulating that the energy-weighted modulations on the beams to be mixed appear on the harmonic. Mathematically, the equation

$$3\omega\left[1 + 2B_{3\omega}^2 + \cosh\left(2B_{3\omega}\right)\right] = \sum_{n=1}^{2} n\omega\left[1 + 2B_{n\omega}^2 + \cosh\left(2B_{n\omega}\right)\right] \tag{30}$$

is solved numerically for $B_{3\omega}$, given $B_{1\omega}$ and $B_{2\omega}$.

The focus lens is modeled as a 4-cm-thick plane-parallel plate of fused silica. The vacuum window is located 25 cm downstream of the 3.4-m effective-focal-length focusing lens in the converging beam. This portion of the UV system can be efficiently modeled by making use of the Talanov[33] transformation. To determine the beam modulation on the vacuum window, the beam is propagated the transformed distance z' with coordinates (x', y') given by

$$z' = \frac{z}{1 - z/f}, \tag{31}$$

$$(x', y') = \frac{(x, y)}{1 - z/f}. \tag{32}$$

This transformation yields the beam profile at the vacuum window by propagating the 40-cm aperture beam $z' = 27$ cm instead of $z = 25$ cm. Since only the resulting increase of the B-integral is of interest, rather than applying the transverse grid transformation in Eq. (32), the value of γ for the vacuum window was simply increased by the square of $1/(1–z/f)$ to model the beam area's reduction and therefore intensity increase. This changed the value of γ from $3.88 \times$ to 4.52×10^{-7} cm^2/GW.

An additional complication of the model is the presence of the DPP 20 cm in front of the focusing lens. The DPP's spatial-phase modulation will itself be converted into spatial-amplitude modulation by propagation. The DPP's spatial phase will add and subtract from the SSD-induced phase in a complicated way. In the worst case, converging phase features from SSD and the DPP will increase the intensification. The DPP used for the OMEGA EP demonstration experi-

ments was designed at LLE[34] to produce a 1.1-mm-diam focal spot. Adequately resolving the phase features generated by this optic required very large spatial-grid resolutions (>1024 × 1024). Over the 47 cm of equivalent propagation distance from the DPP to the vacuum window, no caustics are generated. A simulation generated by propagating the design phase map of the DPP over the distances in question is shown in Fig. 134.19. In the absence of any other modulation, the peak intensity increase caused by modulation from the DPP on the focus lens and the vacuum window would be 3.2% and 7.6%, respectively. As a zero-order approximation to the effect of the DPP on B, the γ's for the focus lens and the vacuum window were further increased by 3.2% and 7.6%, respectively, to 4.00×10^{-7} cm^2/GW and 4.86×10^{-7} cm^2/GW.

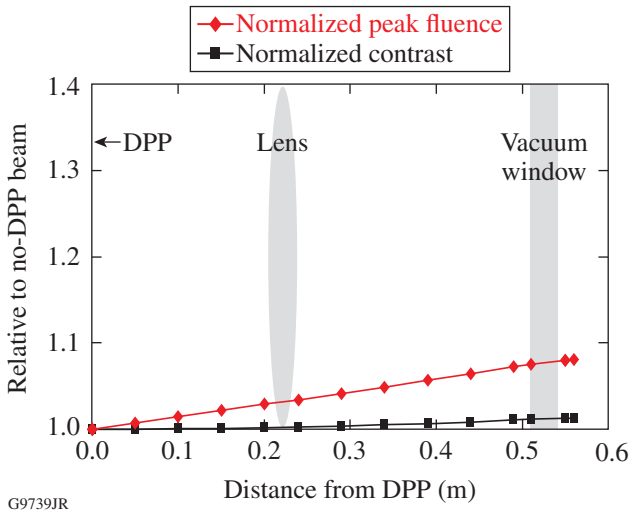

Figure 134.19
The normalized peak fluence and the normalized contrast caused by modulation from the 1.1-mm-spot DPP as a function of distance from the DPP.

Results

The temporal shape used in the model is shown in Fig. 134.20, along with the modulators' waveform. This shape was taken from an early measurement of one of the IR pickets in the front end. The pickets generated for the OMEGA EP demonstration shot campaign were closer to Gaussian with a shorter (~150-ps) temporal width. The advantage of wider pickets for these simulations is to ensure that the peak temporal intensity extends over the time the modulators are co-phased. Since OMEGA EP operates in the small-signal regime for these pickets, it is an excellent representation of the picket at the TSF lens output.

The B-integral as a function of distance from the FCC's for the maximum power determined by a B-integral limit equals 2.0, as shown in Fig. 134.21. The UV B-integral starts at 0.5 rad at the FCC's largely because of the IR contribution from the TSF output lens and the IR DBS. This result was obtained by adjusting the peak input intensity until a B-integral of 2.0 was obtained. This was achieved at a peak UV power measured at the vacuum window of 1.6 TW, which represents an upper bound for the picket power.

This result is the B-integral due only to AM resulting from the propagation of multi-FM SSD in the OMEGA EP Laser System. Many other effects have been neglected in this analysis including, but not limited to, gain narrowing in the amplifiers, etaloning in beamline components, etc. Therefore, this result is *not* the ultimate peak-power limit of OMEGA EP with multi-

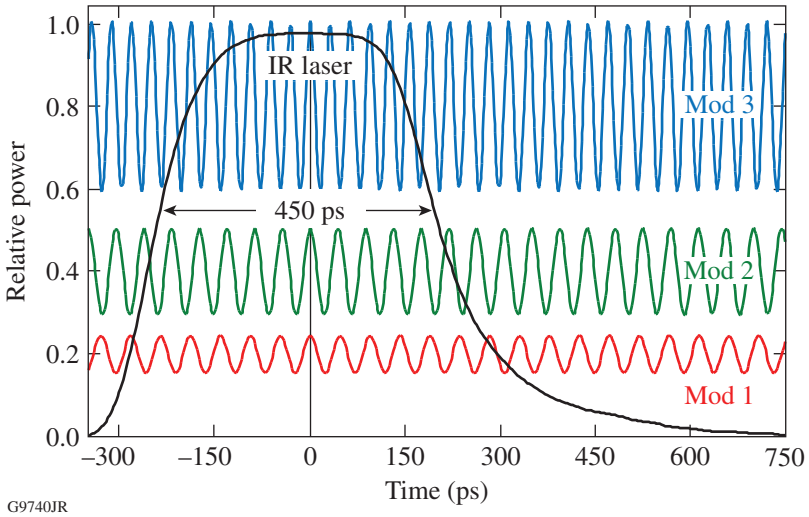

Figure 134.20
The IR pulse shape used in the modeling along with the modulator waveforms.

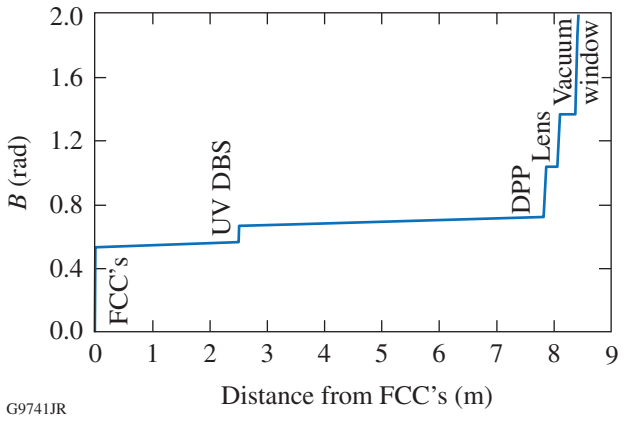

Figure 134.21
B-integral as a function of distance from the FCC's for a 710-J, 444-ps pulse of 1.60-TW peak power. The *B*-integral at the output of the vacuum window for this pulse is 2.0 rad.

FM SSD applied. Indeed, there is significant uncertainty in this calculation simply caused by the knowledge of the γ's of each of the materials.

Conclusions and Additional Work

An estimate of the peak-power limit resulting from the addition of multi-FM SSD to the OMEGA EP Laser System has been calculated. A connection was made between the work of Chuang[7] and the work of Hocquet,[9] and it was shown that their predictions are the same. The advanced laser design code Miró was then applied to first computationally replicate the results of Chuang and then compute the OMEGA EP peak-power limit in the presence of multi-FM SSD. This peak-power limit then becomes one part of a budget that determines the actual on-target peak-power limit of the system.

The *B*-integral is a convenient metric to rapidly estimate the damage threat to a system from self-focusing. The actual threat to the final optic is most accurately assessed[35] by comprehensive modeling that includes the phase contributions of all the system optics to directly model the beam filamentation at the vacuum window. Further work would involve high-resolution simulations to compute these effects. The issue of the longitudinal magnification should be addressed by an actual measurement on the system of the AM as a function of transverse beam location in the dispersion direction. Additional amplitude modulation caused by gain narrowing in the amplifiers can be added to the existing Miró model.

ACKNOWLEDGMENT

This work was supported by the U.S. Department of Energy Office of Inertial Confinement Fusion under Cooperative Agreement No. DE-FC52-08NA28302, the University of Rochester, and the New York State Energy Research and Development Authority. The support of DOE does not constitute an endorsement by DOE of the views expressed in this article.

REFERENCES

1. S. Skupsky, R. W. Short, T. Kessler, R. S. Craxton, S. Letzring, and J. M. Soures, J. Appl. Phys. **66**, 3456 (1989); in *LLE Review Quarterly Report* **78**, 62, Laboratory for Laser Energetics, University of Rochester, Rochester, NY, LLE Document No. DOE/SF/19460-295 (1999).

2. T. J. B. Collins, J. A. Marozas, K. S. Anderson, R. Betti, R. S. Craxton, J. A. Delettrez, V. N. Goncharov, D. R. Harding, F. J. Marshall, R. L. McCrory, D. D. Meyerhofer, P. W. McKenty, P. B. Radha, A. Shvydky, S. Skupsky, and J. D. Zuegel, Phys. Plasmas **19**, 056308 (2012).

3. J. A. Marozas, T. J. B. Collins, and J. D. Zuegel, "Multiple-FM Smoothing by Spectral Dispersion—An Augmented Laser Speckle Smoothing Scheme," to be submitted to the Journal of the Optical Society of America B.

4. J. E. Rothenberg, D. F. Browning, and R. B. Wilcox, in *Third International Conference on Solid State Lasers for Application to Inertial Confinement Fusion*, edited by W. H. Lowdermilk (SPIE, Bellingham, WA, 1999), Vol. 3492, pp. 51–61.

5. A. B. Carlson, *Communication Systems: An Introduction to Signals and Noise in Electrical Communication*, McGraw-Hill Electrical and Electronic Engineering Series (McGraw-Hill, New York, 1968), p. 228.

6. The correct phasing of the sidebands is such that all of the odd-order lower *sidebands* are π out of phase. For a very illustrative phasor representation of why this particular phasing eliminates AM and leads to pure frequency modulation, see Ref. 5, pp. 228–232.

7. Y.-H. Chuang, "Amplification of Broad-Bandwidth Phase-Modulated Laser Counterpropagating Light Waves in Homogeneous Plasma," Ph.D. thesis, University of Rochester, 1991.

8. Note that this result is independent of a grating being upstream from the modulator used to pre-shear the pulse.

9. S. Hocquet *et al*., Appl. Opt. **47**, 3338 (2008).

10. J. W. Goodman, *Introduction to Fourier Optics* (McGraw-Hill, New York, 1968), p. 53.

11. J.-C. Chanteloup *et al*., J. Opt. Soc. Am. B **17**, 151 (2000).

12. D. C. Brown, in *High-Peak-Power Nd:Glass Laser Systems*, edited by D. L. MacAdam, Springer Series in Optical Sciences (Springer-Verlag, Berlin, 1981), Vol. 25, Chap. 1, p. 45.

13. J. Trenholme, *Laser Program Annual Report 1974*, Lawrence Livermore National Laboratory, Livermore, CA, Report UCRL-50021-74, 197 (1975).

14. J. R. Carson, Proc. IRE **10**, 57 (1922).

15. C. A. Haynam *et al*., Appl. Opt. **46**, 3276 (2007). In particular, see Fig. 4 in this reference.

16. Non-Major System Acquisition, NNSA Division of Secondaries and Inertial Fusion, NA-113.1, U.S. Department of Energy National Nuclear Security Administration, Washington, DC (1 May 2003).

17. The dispersion direction is horizontal in laser sources, is vertical in the main laser chain, and is horizontal again at the frequency-conversion crystals.

18. M. D. Skeldon, R. S. Craxton, T. J. Kessler, W. Seka, R. W. Short, S. Skupsky, and J. M. Soures, IEEE J. Quantum Electron. **28**, 1389 (1992).

19. R. S. Longhurst, *Geometrical and Physical Optics*, 3rd ed. (Longman, London, 1973).

20. R. Korniski and J. K. Lawson, in *International Optical Design Conference*, 2002 OSA Technical Digest Series (Optical Society of America, Washington, DC, 2002), Paper ITuD5.

21. It does, however, have a modest FM modulation to suppress stimulated Brillouin scattering in the UV optics.

22. O. Morice, Opt. Eng. **42**, 1530 (2003).

23. LLE makes use of Miró through the kind permission of CEA/CESTA.

24. Ph. Donnat *et al*., MIRÓ V5$_\varepsilon$ Reference Manual (1998).

25. J. A. Marozas, J. D. Zuegel, and T. J. B. Collins, Bull. Am. Phys. Soc. **55**, 294 (2010).

26. Since there are two FCC's, the grating was imaged to the midplane between them.

27. R. S. Longhurst, *Geometrical and Physical Optics*, 3rd ed. (Longman, London, 1973), p. 14.

28. This assumes, of course, that the normal to the wavefront remains within the tuning acceptance angle of the crystals.

29. O. Morice, X. Ribeyre, and V. Rivoire, in *Third International Conference on Solid State Lasers for Application to Inertial Confinement Fusion*, edited by W. H. Lowdermilk (SPIE, Bellingham, WA, 1999), Vol. 3492, pp. 832–838.

30. Ph. Donnat *et al*., MIRÓ V5$_\varepsilon$ Reference Manual (1998), Chap. 3, Sec. 3.12.6, pp. 162–164.

31. J. Trenholme *et al*., *Shiva Nova CP&D Interim Report, Laser Fusion Program*, Lawrence Livermore National Laboratory, Misc. 107, 2-3–2-324 (1977); for a fuller discussion of this expression and its derivation, see D. C. Brown, in *High-Peak-Power Nd:Glass Laser Systems*, edited by D. L. MacAdam, Springer Series in Optical Sciences (Springer-Verlag, New York, 1981), Vol. 25, Chap. 7, Sec. 7.5, p. 216.

32. Here the fraction of noise power in the two frequency ranges of large ripples and fast-growing ripples has been assumed to be equal.

33. V. I. Talanov, JETP Lett. **11**, 199 (1970); for a discussion of the applicability of this transformation, see J. B. Trenholme and E. J. Goodwin, *Laser Program Annual Report 1976*, Lawrence Livermore National Laboratory, Livermore, CA, Report UCRL-50021-76, 2-339−2-344 (1976).

34. *Final Proposal for Renewal Award for Cooperative Agreement DE-FC52-92SF-19460* Between the U.S. Department of Energy and the Laboratory for Laser Energetics of the University of Rochester, Part 1: Technical Program (Rochester, NY, 2007).

35. P. J. Wegner *et al*., in *Optical Engineering at the Lawrence Livermore National Laboratory II: The National Ignition Facility*, edited by M. A. Lane and C. R. Wuest (SPIE, Bellingham, WA, 2004), Vol. 5341, pp. 180–189.

Fiber Front End with Multiple Phase Modulations and High-Bandwidth Pulse Shaping

Introduction

Since their first demonstration, lasers have led to incredible progress in many scientific and technological fields. High-intensity lasers have allowed researchers to explore new regimes for the interaction of light with matter. One far-reaching potential application of lasers is inertial confinement fusion (ICF), where nuclear fusion reactions are initiated by heating and compressing a deuterium–tritium (DT) target with laser beams. Large-scale laser facilities are in operation or in construction with the goal of demonstrating ignition,[1,2] following decades of research.[3] One difficulty of ICF is to maintain a high degree of spherical symmetry when the target is compressed: a spatially nonuniform on-target illumination can seed Rayleigh–Taylor instabilities at the target surface and detrimentally impact the fuel compression.[4] Smoothing by spectral dispersion (SSD) is an approach to reduce the spatial nonuniformities of the illumination generated by high-energy laser beams.[5] SSD lowers the coherence of the beams by frequency modulating them (i.e., increasing the optical-frequency content), spatially dispersing them with a diffraction grating (i.e., introducing a relation between optical frequency and wave vector), and focusing them after a random phase plate (i.e., creating a broad range of wave vectors in the near field and a speckle distribution in the far field).[6,7] The time-integrated far-field fluence of individual beams is smoothed because the phase plate generates randomly distributed speckles with a frequency-dependent distribution; consequently, the frequency-modulated optical pulse leads to a time-varying speckle field that averages out. SSD is routinely used at facilities such as the National Ignition Facility (NIF)[1] and the OMEGA Laser System.[8] The required amount of smoothing and the architecture of the laser systems determine the implementation of SSD: the NIF uses one-dimensional (1-D) SSD with modulation at ~17 GHz and a single diffraction grating in the front end, while OMEGA uses two-dimensional (2-D) SSD with modulation along two axes at ~3 GHz and 10 GHz and multiple gratings.[9] Phase modulation is also required in large-scale, high-energy laser systems to prevent stimulated Brillouin scattering (SBS): a high-intensity monochromatic beam can create acoustic waves in a physical medium (e.g., a fused-silica lens) that will scatter the beam, resulting in instability, losses, and optical damage.[10] Phase modulation generates sidebands that are individually below the threshold for SBS, suppressing its detrimental effect. This modulation is typically performed at a frequency of 3 GHz with a modulation index of ~5 rad on the NIF, resulting in approximately ten sidebands in an ~30-GHz bandwidth.

The NIF is currently configured for indirect drive, where the UV laser beams are incident on the internal sides of a gold hohlraum and generate x-ray radiation that compresses the target. SSD is performed at 17 GHz with a modulation index equal to a few radians. Simulations of direct drive, where the UV beams directly compress the target, on the NIF show that SSD must be implemented on the initial part of the pulse shape with three distinct modulation frequencies (multi-FM).[11] These modulations are approximately at 21.2 GHz, 22.8 GHz, and 31.9 GHz, i.e., at significantly higher frequencies than what is currently being used on existing laser systems for SSD and SBS suppression (SBSS). The main part of the pulse shape, which produces most of the on-target energy, uses SSD at 17 GHz and SBSS. With the parameters of Table 134.V, the multi-FM optical spectrum (98% of the energy in a 200-GHz bandwidth) is ~50% broader than the main-pulse spectrum (98% of the energy in a 133-GHz bandwidth). A fiber front-end prototype demonstrating the required technologies has been developed. It relies on high-bandwidth $LiNbO_3$ phase modulators and Mach–Zehnder modulators for phase modulation and pulse shaping, respectively. Large-scale laser systems operate close to the technological limits of optical components, and amplitude modulation caused by spectral distortion of frequency-modulated signals must be understood and controlled to avoid optical damage. Subsystems that compensate and characterize for frequency-modulation-to-amplitude-modulation (FM-to-AM) conversion have been developed. The front end has supported multiple shot campaigns on the OMEGA EP Laser System[12] to demonstrate the laser and beam-smoothing performance.[13]

In this article, we first describe the architecture of the fiber front end with an emphasis on the modulators used for phase modulation (SSD/SBSS) and amplitude modulation (pulse

Table 134.V: Characteristics of the phase modulations applied in the front end. All the frequencies were multiples of the reference frequency f_{Ref} = 37.998935 MHz. The first two modulations were performed in the main channel; the three other modulations were performed in the picket channel.

Modulation	Frequency (GHz)	Multiple of f_{Ref}	Modulation Index (rad)
Stimulated Brillouin scattering suppression (SBSS)	f_{SBSS} = 3.002	79	5.5
Smoothing by spectral dispersion (SSD)	f_{SSD} = 16.986	447	2.6
Multi-FM 1	f_1 = 21.165	557	0.45
Multi-FM 2	f_2 = 22.837	601	1.04
Multi-FM 3	f_3 = 31.881	839	2.07

shaping) and the subsystems developed to reduce FM-to-AM conversion and safely operate the laser system. The experimental characterization of the fiber front-end performance is then presented, in particular, phase modulation, pulse shaping, and amplitude noise, followed by the conclusions.

Front-End Architecture

1. Requirements

The front-end requirements for this demonstration on the OMEGA EP Laser System have been set based on simulations of polar-drive ignition on the NIF and the requirement that the new front end be integrated into the existing laser systems. The typical pulse shape in the ultraviolet (UV), i.e., after amplification in the full laser system and frequency conversion, is shown in Fig. 134.22. It is composed of two sections:

- Between 0 and 4.5 ns, three short pulses (named "pickets") launch shocks into the target.[14] Each picket has a duration of a few hundred picoseconds and must be phase modulated at three noncommensurate microwave frequencies (multi-FM modulation) to provide optimal beam smoothing on target. The three modulation frequencies in this design are approximately 21.2 GHz, 22.8 GHz, and 31.9 GHz (Table 134.V).

- After 4.5 ns, a rectangular high-energy pulse preceded by a low-intensity step pulse between 4.5 ns and 6 ns is required. The step pulse launches an additional shock into the target before compression by the main high-energy pulse. The main pulse lasts for several nanoseconds but has rise/fall times that are in the hundreds-of-picoseconds range. This pulse must be phase modulated at 3 GHz for SBSS and at 17 GHz for SSD (Table 134.V).

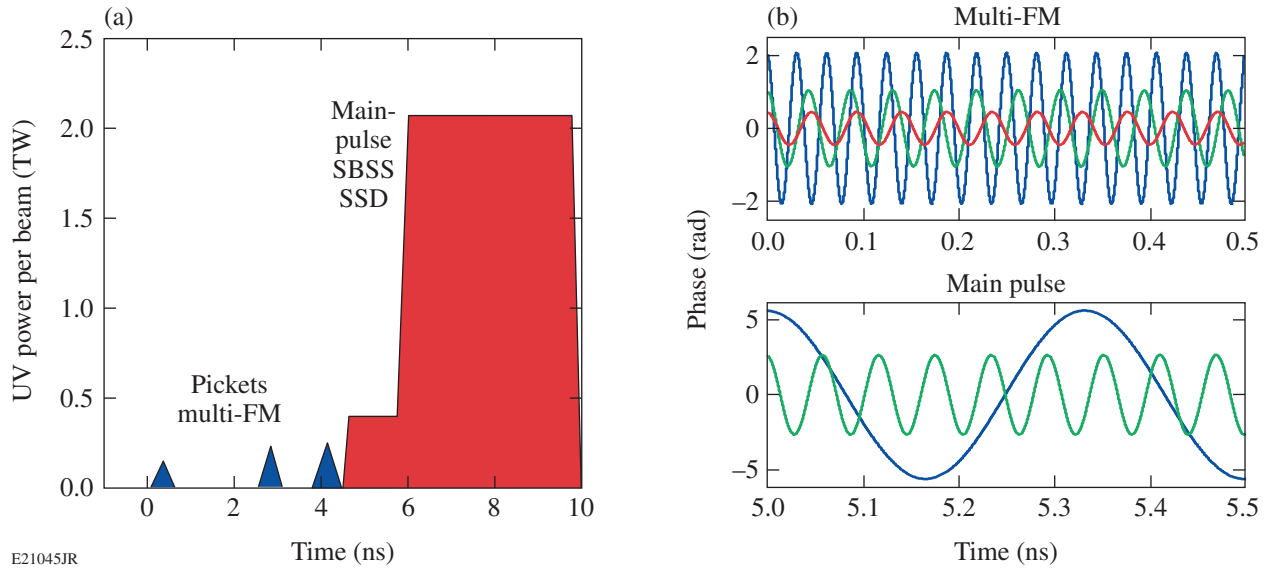

Figure 134.22

(a) Schematic of the pulse shape (power versus time) after frequency conversion at the end of the laser system, composed of three short, low-energy pickets and a main high-energy pulse. (b) Plots of the phase modulations required at the fundamental wavelength on the pickets (f_1, f_2, f_3) and on the main pulse (f_{SSD} and f_{SBSS}), with parameters given in Table 134.V. FM: frequency modulation; SBSS: stimulated Brillouin scattering suppression; SSD: smoothing by spectral dispersion.

The front end must operate at ~1053 nm, which is the peak of the gain for neodymium-doped phosphate glass. It is designed as a proof-of-concept of a system that could be used in the NIF Master Oscillator Room[15,16] and has been built around technologies that are either compatible with its environment and requirements or can be upgraded to suitable technologies for an actual deployment. It must contain fail-safe systems that will interrupt the amplification so that no high-energy pulse propagates in the laser system if such propagation could lead to damage. The output pulses must have low variations in energy and pulse shape, and have sufficient energy to seed the preamplifier module (PAM), a sequence of amplifiers used on the NIF to boost the energy before amplification in the main beamline.[17]

2. General Structure

The front end optically combines two distinct optical channels operating at wavelengths close to 1053 nm—one generating the main pulse and one generating the pickets (Fig. 134.23). The two channels have a symmetric architecture, combining programmable pulse shaping by $LiNbO_3$ Mach–Zehnder modulators driven by arbitrary waveform generators (AWG's), phase modulation by $LiNbO_3$ phase modulators, and two stages of amplification to compensate for propagation and insertion losses. Fail-safe systems protecting the high-energy beamline and components operate in real-time and can interrupt the propagation of an improperly modulated pulse before amplification to high-energy levels. The two channels are combined by a fiber coupler with a fixed coupling ratio. The relative level of the two channels is adjusted via the gain of fiber amplifiers (there are two amplifiers in each channel and one amplifier in the combined section of the front end). Most pulse shapes of interest require similar output levels for the two channels, which is facilitated by the symmetric structure. All components are fiber coupled up to the PAM.

Birefringent optical fibers maintain the polarization state throughout the system. Most components use polarization-maintaining (PM) fibers that support two orthogonal propagation modes. The fibers connecting components and chassis are polarizing (PZ) fibers that support only one propagation mode at 1053 nm: linearly polarized light launched along the guiding direction is nominally transmitted without loss but light polarized along the orthogonal direction is strongly attenuated. The absence of crosstalk in such fibers helps to reduce the FM-to-AM conversion caused by delayed self-interference when successive PM fibers are used.[18] An extinction ratio (ratio of the guided-mode transmission to the blocked-mode transmission) higher than 30 dB is nominally obtained with 4-m patchcords.

The phase-modulation drive voltages are synchronized to the reference frequency $f_{Ref} = 37.998935$ MHz used throughout the OMEGA EP Laser System. The phase modulations at the required five microwave frequencies (Table 134.V) are obtained using commercial phase-locked oscillators, ensuring that the output frequency is an exact integer multiple of the reference frequency. A phase shifter on each phase-modulation drive allows for independent temporal tuning of the phase modulation relative to the optical pulse. The performance of on-target smoothing does not depend significantly on the relative phases of the three sinusoidal modulations.[11] Tuning of the relative phases is included because it could be used to control the amplitude of the power modulation caused by FM-to-AM conversion, although this has not been studied in detail. All

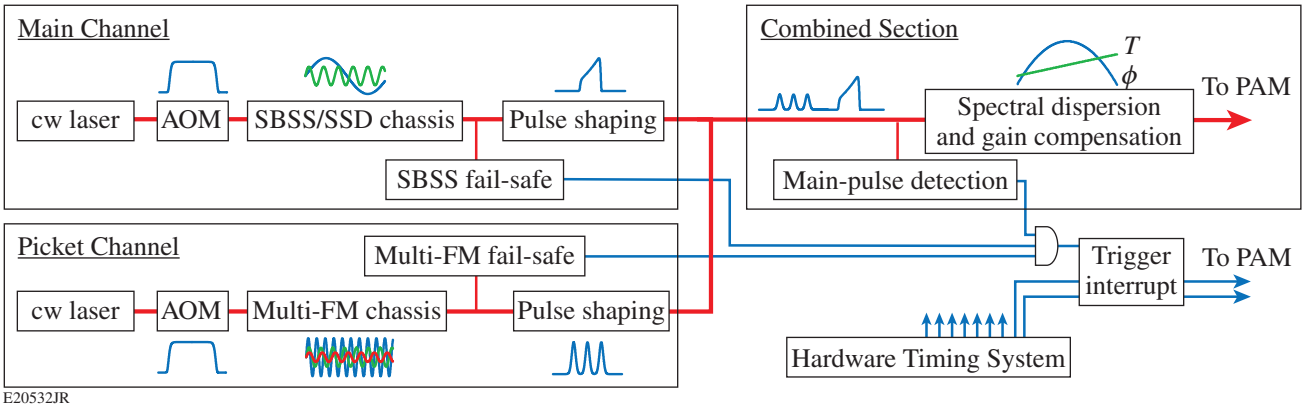

Figure 134.23

General layout of the front end. The picket and main channel are independently phase modulated and shaped after gating of a continuous-wave (cw) seed source by an acousto-optic modulator (AOM). Dispersion and amplitude compensations are performed after optical combination. Three fail-safe systems are used to ensure safe operation. Five fiber amplifiers (two in each independent section and one in the combined section) have not been represented. PAM: preamplifier module.

components in the front end are synchronized to the Hardware Timing System (HTS) used throughout the laser facility, which is also synchronized to f_{Ref}. The fiber front end operates at 300 Hz. All electronic components (including the fail-safe systems described in the following subsections) can operate at 960 Hz, the repetition rate of the NIF front end. The ytterbium-doped fiber amplifiers have not been tested at 960 Hz, which corresponds to operation close to the fluorescence lifetime of ytterbium, but similar amplifiers are operated in the NIF front end at that rate. The timing of the two channels relative to each other and to the laser facility is adjusted by controlling the delay of all the corresponding trigger signals from the HTS.

3. Main Channel

The main channel (Fig. 134.23) uses a cw (continuous-wave) laser operating at ~1053 nm gated by an acousto-optic modulator (AOM) to a duration of 100 ns. The gated pulse is phase modulated by the custom three-section phase modulator shown in Fig. 134.24. The phase modulator has three consecutive sections of $LiNbO_3$ that can be independently driven. Each section is externally terminated to allow for the use of high-power drives that could damage an internal 50-Ω termination. A single device with three phase-modulation sections is advantageous compared to the cascaded sequence of three distinct phase modulators: the modulator is more compact and easier to mount, and the optical losses from input to output are lower than 5 dB. In the main channel, phase modulation is provided in only two of the three sections. In one section, phase modulation at 3 GHz is induced with a modulation index of 5.5 rad for SBSS. In the second section, phase modulation at 17 GHz with an index of 2.6 rad is performed for on-target beam smoothing. The resulting optical spectrum is plotted in Fig. 134.25(a).

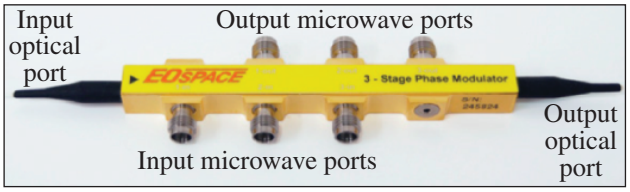

Figure 134.24
The three-section phase modulator, with distinct input and output ports for the three phase-modulating sections.

Pulse shaping is implemented in a custom two-section modulator comprised of two consecutive $LiNbO_3$ Mach–Zehnder modulators (MZM's). One of the MZM's is driven by a shaped voltage from the amplified output of a 10-GS/s AWG

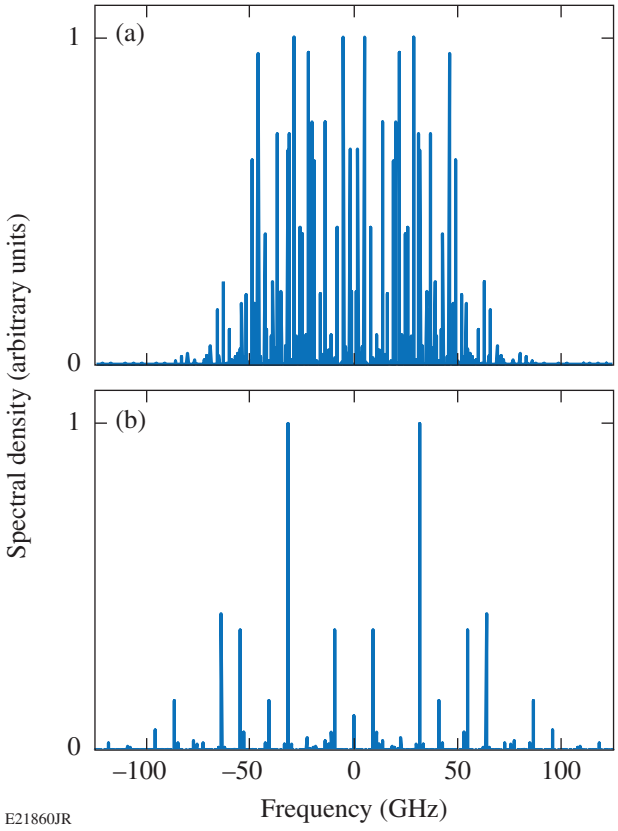

Figure 134.25
(a) Optical spectrum of the pulse after phase modulation in the main channel; (b) optical spectrum of the pulse after phase modulation in the picket channel.

(Kentech AWG-10). This modulator is used for precise pulse shaping, ensuring that the channel output meets the requirements imposed by the target physics and the safety of the laser system. The other MZM is driven by an unshaped square pulse with programmable duration. This MZM acts as a gate on the shaped pulse: when the duration of the square pulse is set appropriately, the modulator does not shape the optical pulse but enhances the temporal contrast (ratio of the power at full transmission to the power at extinction). For example, with two MZM's having a nominal extinction ratio of ≥20 dB, the overall extinction ratio is ≥40 dB. High extinction ratios are particularly important when optically combining optical pulses from two distinct sources because leakage from one source can detrimentally interfere with the pulse from the other source.

A fraction of the main channel is sent to a fail-safe system to monitor the 3-GHz phase modulation and avoid optical damage from SBS.[10] The SBSS fail-safe is a unit provided by Lawrence Livermore National Laboratory.[15] The unit intentionally induces FM-to-AM conversion on the monitored signal with a spectral filter to convert the 3-GHz phase modulation into a

3-GHz amplitude modulation that can be measured with an AM detector. The unit monitors in real-time the phase-modulation amplitude and duration on the optical pulse, i.e., it ensures that the phase modulation is sufficient and applied during the total length of the ~100-ns pulse gated by the AOM. It also detects undesirable characteristics of the optical pulse, spurious amplitude modulation not intentionally generated by the fail-safe system, and sudden changes in the input energy that could prevent the fail-safe from adequately detecting a fault. Its output is a 5-V logic trigger that is high if the duration and amplitude of the phase modulation are nominal and low if at least one of the safe operating conditions is not met. This trigger is sent to the PAM Trigger Interrupt Safety System (PTISS) to prevent unsafe high-energy amplification if there is a fault.

4. Picket Channel

The picket channel (Fig. 134.23) uses a set of optical components identical to the one deployed on the main channel. The three sections of the phase modulator are driven by the three distinct phase modulations at 21.2 GHz, 22.8 GHz, and 31.9 GHz with respective modulation indices of 0.45 rad, 1.04 rad, and 2.07 rad. The resulting optical spectrum is plotted in Fig. 134.25(b). Pulse shaping is performed by driving one section of a two-section MZM with the output of a Tektronix 7122 AWG operating at 24 GS/s amplified by a broadband amplifier. The other section is driven by a square pulse to increase the extinction ratio.

The pickets are nominally short optical pulses, i.e., with a spectrum relatively broad compared to the typical nanosecond pulses shot on high-energy laser systems, therefore reducing concern for SBS in the absence of phase modulation, but a fail-safe system was designed to prevent high-energy amplification in the absence of significant phase modulation on this channel. The fail-safe system measures the power in two spectral bands of the phase-modulated pulse, one on each side of the carrier frequency, to infer the amount of phase modulation. A diffraction grating disperses the optical pulse, and a focusing lens generates a Fourier plane in which spectral components are spatially separated and individually focused. Multimode optical fibers mounted on a V-groove array are used at the Fourier plane to couple light from the two bands of the optical spectrum to two amplified photodiodes. The system is designed to detect the optical power in two bands centered 127.6 GHz apart, i.e., on the sidebands of the carrier at twice the modulation frequency f_3. These two bands correspond to the spectrally dispersed light from the diffraction gratings on two fibers separated by 500 μm at the Fourier plane. Each 105-μm-diam fiber integrates the optical power over 26.8 GHz. Thresholds for the measured powers are set when the system operates at the default phase-modulation amplitudes so that the fail-safe trips when the modulation at f_3 does not have sufficient amplitude, regardless of the presence of the modulation at f_1 and f_2. This would detect malfunction of the entire phase-modulation unit for the picket channel and malfunction of the sub-unit responsible for phase modulation at the frequency f_3. A precise analysis of the different failure modes and their impact on SBS has not been conducted at this point, but operation with f_3 operating at its nominal modulation index was thought to be safe for the system because the corresponding spectrum is spread over more than 100 GHz with each sideband broadened to several GHz because of the short picket duration. Simultaneous failure of the two sub-units responsible for phase modulation at f_1 and f_2 is highly unlikely because of the architecture of the phase-modulation unit; therefore, the detection of the frequency f_3 indicates that at least one other modulation frequency is also present, further contributing to SBS reduction. The fail-safe 5-V logic output (high for the nominal modulation and low for insufficient bandwidth) is sent to the PTISS to prevent high-energy amplification in the latter case.

5. Combined Section

The picket and main channels are combined with identical polarization states by a fiber coupler after timing and amplitude adjustments. Chromatic dispersion and nonuniform spectral gain are compensated identically after the combiner for economy of scale and minimized complexity. A rack-mounted device combining dispersion and amplitude compensation has been built (Fig. 134.26). Spectral distortion (i.e., phase and/or amplitude) of a phase-modulated pulse leads to amplitude modulation in the time domain. FM-to-AM conversion is detrimental to the operation of high-energy laser systems because amplitude modulation leads to higher peak power for a given pulse energy.[19,20] Amplitude modulations are also a concern when the propagation is nonlinear. The chromatic dispersion of optical fibers and other optical components at 1053 nm corresponds to a positive second-order dispersion ($d^2\varphi/d\omega^2 > 0$, where φ is the phase accumulated by propagation as a function of frequency). The total length of fiber for each channel (calculated from the output of the phase modulator to the last fiber amplifier) is ~130 m. A frequency-dependent amplitude modulation arises from gain tilt in the ytterbium-doped fiber amplifiers and the Nd:glass regenerative amplifier. The fiber amplifiers are broadband, but their gain varies over the spectral range of interest, with a typical gain slope of 5% per 100 GHz (i.e., the difference between the gain at f_0 + 50 GHz and f_0 – 50 GHz normalized to the gain at f_0 is 5%). The regenerative amplifier gain is approximately Gaussian with a

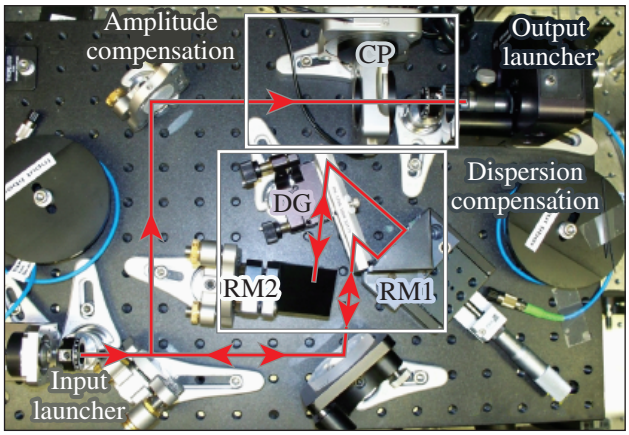

Figure 134.26
The amplitude/dispersion compensator. The dispersion compensator is composed of two roof mirrors, for horizontal (RM1) and vertical (RM2) beam displacement and inversion, and a transmission diffraction grating (DG). The amplitude compensator is composed of a calcite plate (CP) mounted on two rotation stages.

full width at half maximum (FWHM) of 400 GHz. The front end is configured to seed the regenerative amplifier on the long-wavelength slope of the Gaussian gain curve, for which the gain slope is approximately 40% per 100 GHz. The uncompensated gain slope over the fiber front end and regenerative amplifier would lead to large-amplitude modulation. Spectral distortions have been compensated with fiber-coupled free-space subsystems that were combined in a single enclosure to minimize losses: without any spectral amplitude modulation, the input-to-output loss is ~5 dB.

Dispersion compensation ($d^2\varphi/d\omega^2 < 0$) is performed with a compact compressor using a single transmission grating in a four-pass configuration. The transmission grating is a 1700-l/mm fused-silica grating used in the Littrow configuration. The diffracted beam is sent back to the same grating after a lateral displacement and horizontal beam inversion by a roof mirror; it is then diffracted again by the grating, displaced vertically by another roof mirror, and sent back to the grating, first roof mirror, and grating. The dispersion is controlled by a translation stage on the first roof mirror modifying the distance between the first and second diffractions on the grating and identically between the third and fourth diffractions. The compensator was designed to overcompensate the dispersion of the front end because of its future use in a system mimicking the front end of the NIF. In that system, the front end is in a different room from the NIF PAM's, resulting in the shaped phase-modulated optical pulse traveling in several hundred meters of PZ fibers. This compensator is built for ~100 m of additional PZ fiber between the front end and the PAM, even if these two systems are physically separated by only a few meters in our system. Translation of the first roof mirror allows for an increase in the magnitude of the introduced negative second-order dispersion to compensate for longer fiber lengths.

The optical source is linearly polarized, allowing for spectral amplitude modulation using a Lyot-type filter implemented with a birefringent calcite plate.[21] The plate can be rotated relative to a vertical rotation axis (Axis 1) and relative to an axis perpendicular to its surface (Axis 2) to adjust the spectral modulation. At normal incidence, rotation around Axis 2 changes the relative ratio of the two polarization components traveling along the two axes of the plate, which controls the depth of the spectral modulation. Rotation around Axis 1 changes the retardance of the plate, which controls the location of the spectral modulation along the frequency axis. The calcite plate is followed by a zeroth-order half-wave plate and a PZ fiber acting as a polarizer. Calcite plates with thicknesses from 1 mm to 4 mm have been used during a testing phase, with similar results, and a 4-mm calcite plate has been installed for operation.

The pickets are nominally short pulses that can reach high peak powers if the system is configured for the generation of a high-energy main pulse but the latter pulse is absent—for example, because of an equipment failure, triggering issue, or operator error. A fail-safe system ("main-pulse detection fail-safe") prevents amplification and subsequent damage when the main pulse is absent. This system uses photodetection and integration of the combined output to generate a signal representative of the front-end output energy, which must be higher than a user-set threshold for safe operation. The system output is a 5-V logic signal that is high when operation is safe and low otherwise. This signal is sent to the PTISS.

The three fail-safe systems (SBSS fail-safe operating on the main channel; picket-bandwidth fail-safe operating on the picket channel; and main-pulse detection fail-safe operating on the combined output) provide three logical signals to the PTISS. The latter system is fed with two triggers: the switch-out trigger to the Pockels cell in the regenerative amplifier and the slicer-on trigger for the Pockels cell located after the regenerative amplifier. In safe operation, the front end delivers a seed pulse to the regenerative amplifier; this pulse is amplified after multiple round-trips in the cavity; the amplified pulse is ejected by the Pockels cell located inside the amplifier; and the output pulse is gated by an external Pockels cell (the slicer) that is turned on to let the ejected pulse go through. In the absence

of trigger signals from the three fail-safe systems, the PTISS interrupts the two triggers. The pulse being amplified in the regenerative amplifier remains in the laser cavity and is not ejected by the intracavity Pockels cell. The slicer is not turned on, further decreasing the transmission.

Front-End Performance

1. Pulse Shaping

Temporal characterization of the shaped optical pulses was performed with a 45-GHz, 120-GS/s Teledyne LeCroy Wavemaster oscilloscope and a fiber-coupled 60-GHz Discovery Semiconductors DSC10 InGaAs photodetector. The impulse response of this diagnostic had a FWHM lower than 20 ps. Various algorithms and procedures were tested to correct the frequency-dependent response of the photodetection system (for example, isolating one frequency component and adjusting its spectral amplitude by the known spectral response at that particular frequency to compare its amplitude to a prediction made using known system parameters). It was decided to not use post-processing of the measured waveforms when reporting amplitude noise, although the reported noise values correspond to averages of the noise values over multiple waveforms, as described below. Most measurements have been performed in the front end at 300 Hz and after the regenerative amplifier since that amplifier has the largest amount of square-pulse distortion in our demonstration (the gain on the pulse is a decreasing function of the time because the leading edge of the pulse propagates in the amplifying medium before the trailing edge and experiences more gain). It also has the most-significant impact on the optical spectrum because of its relatively narrow amplification bandwidth and large gain slope. Finally, it operates at a repetition rate of 1 Hz, allowing for the acquisition of statistically meaningful sets of data: the rod amplifier in the PAM after the regenerative amplifier typically operates at one shot every 20 min, significantly impacting the experimental ability to collect multiple data sets for statistical analysis.

The impulse response of the picket and main pulse-shaping systems has been determined by setting one electrical sample of the corresponding AWG to full voltage and measuring the optical output as a function of time. The measured responses have a FWHM of 55 ps and 115 ps for the picket channel and main channel, respectively. The corresponding 10/90 rise and fall times, measured on the impulse responses, are similar to the FWHM for the two systems. These values correspond to to the pulses shaped by the fiber front end. Because of the pulse-front tilt introduced by the SSD grating (~230 ps across the full beam), the on-target pulse duration is significantly longer. The choice of the faster AWG for the picket channel stems from the technical requirements for pulse shaping in these two channels, although generating pickets shorter than ~100 ps is not required.

A wide range of pulse shapes has been generated with the two channels, including single and multiple pickets, long square pulses, and shaped pulses. Figure 134.27(a) displays an example of a pulse shape with three pickets and a long shaped pulse measured at the output of the regenerative amplifier. Figures 134.27(b) and 134.27(c) show close-ups of the measured pulse shape with shaded areas, indicating the root-mean-square (rms) and peak-to-valley variations at each acquisition time, obtained by measuring 50 successive pulses. The rms and peak-to-valley energy variations over 50 measurements are 1.9% and

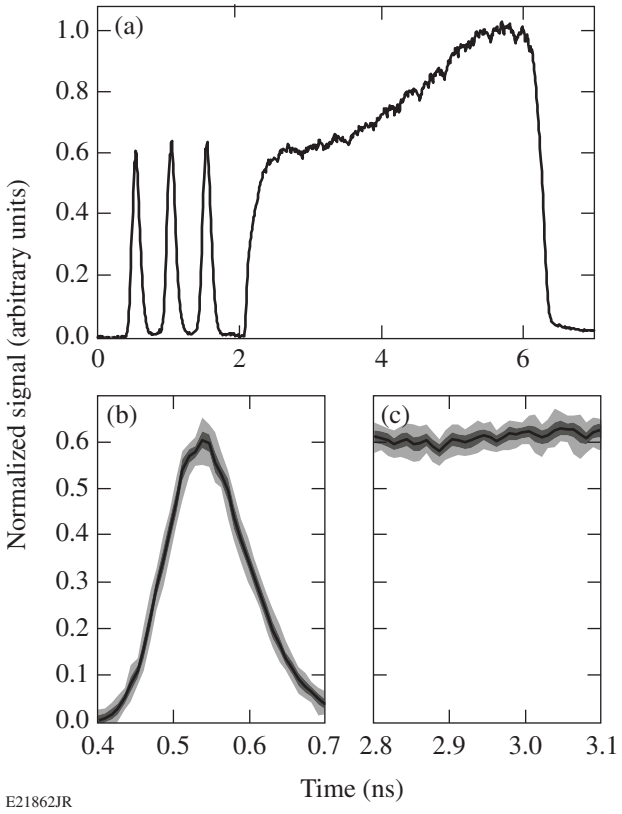

Figure 134.27

(a) Example of pulse shape $P(t)$ measured at the output of the regenerative amplifier. The plotted pulse is an average of 50 successive measurements. [(b) and (c)] Close-ups of the first picket (time between 0.4 and 0.7 ns) and the main pulse (time between 2.8 and 3.1 ns). The black line corresponds to the average of 50 measurements; the dark-gray–shaded region corresponds to the power range $[P(t)-\sigma(t), P(t)+\sigma(t)]$, where $\sigma(t)$ is the standard deviation of P at time t over the 50 measurements, and the light-gray–shaded region corresponds to the power range $[M_-(t), M_+(t)]$, where $M_-(t)$ and $M_+(t)$ correspond to the lowest and highest value of the power measured at time t over the 50 measurements.

9.8%, respectively, for one picket and 1.2% and 5.1%, respectively, for the main pulse. These are overestimates of the actual energy variations because of the oscilloscope analog-to-digital conversion noise, particularly for the picket with a FWHM of ~100 ps for which the energy is obtained by summation over a small number of acquired samples. A 1-ns pulse generated by the picket channel in the same conditions has rms and peak-to-valley energy variations equal to 1.8% and 6.6%, respectively, while the energy variations calculated in a 1-ns window for the monochromatic laser chopped by the AOM before phase modulation are 0.5% and 2.0%. The energy statistics are in agreement with the energy statistics independently measured with an energy meter that indicates a rms variation lower than 2% after the regenerative amplifier seeded by either channel.

The jitter and timing drift between the two channels have been measured over 300 waveforms produced by the front end acquired in a short time window (1.5 min) or long time window (150 min) by estimating the location of the 50% points of the picket-channel trailing edge and main-channel leading edge. The relative timing between the two channels has a rms jitter of 15 ps and a monotonic drift of 20 ps over 2.5 h. The timing drift is attributed to drifts in the pulse-shaping electronics (e.g., triggers) and small temperature changes (although the front end operates in a temperature-controlled environment, each channel contains more than 100 m of optical fibers that are physically distinct). The timing of the picket channel and main channel relative to the oscilloscope time base has rms jitter values of 13 ps and 9 ps, respectively. These are overestimates of the jitter of the front end relative to the reference frequency, i.e., the remainder of the laser system, since they include the oscilloscope jitter. These values are within the required range for this demonstration. The jitter and the finite rise and fall times of the shaped pulses constrain the relative timing between the channels to values greater than 125 ps (delay between the 50% points of the picket-channel trailing edge and main-channel leading edge). Random amplitude modulation related to interference of the two optical pulses is observed for shorter separations.

2. Phase Modulation

Precise characterization of the phase modulators and resulting phase modulation is important. The modulators must first be characterized to ensure that they are suitable for this application, i.e., that they can be driven adequately at the five different microwave frequencies with the required modulation index. During operation, the phase-modulation index must be characterized to ensure that it matches the required specifications. A cw laser field at the optical frequency f_0 phase modulated at the frequency f_m with modulation index m has the temporal electric field

$$E(t) = E_0 \exp(2\pi i f_0 t) \exp[im \sin(2\pi f_m t)]. \quad (1)$$

In the frequency domain, the field is given by

$$\tilde{E}(f) = \sum_n J_n(m)\,\delta(f - f_0 - n f_m), \quad (2)$$

where J_n is the Bessel function of the first kind of index n. The optical spectrum is composed of an infinite number of sidebands at the frequencies $f_0 + nf_m$ with spectral density $|J_n(m)|^2$, but 98% of the energy is concentrated in a $2mf_m$ bandwidth centered at f_0 according to Carson's rule.

Fitting the measured spectrum with the calculated spectrum of a phase-modulated field, where m is the single parameter, makes use of all the measured data and is computationally efficient; this was chosen for modulation-index determination at frequencies corresponding to sidebands that can be resolved. The spectral modes corresponding to f_{SSD} = 17 GHz, f_1 = 21.2 GHz, f_2 = 22.8 GHz, and f_3 = 31.9 GHz are easily resolved with a commercial scanning grating monochromator. The modes corresponding to 3 GHz cannot be individually resolved because the response of the monochromator broadens the individual spectral modes, resulting in a smoothed spectrum. One experimental solution is to develop a dedicated diagnostic measuring the optical spectrum with a resolution suitable to resolve spectral modes separated by 3 GHz (typically sub-GHz); for example, using a scanning Fabry–Perot etalon. It was chosen to use numerical post-processing to estimate the modulation index in this case.

For modulator characterization, a microwave signal generator was used to generate drives with frequency ranging from 15 GHz to 40 GHz. The power of the drive was calibrated at each modulation frequency. The modulation index was determined for each of the three sections of the phase modulators. The corresponding V_π was calculated by scaling the phase-versus-voltage measurement, where the phase is related to the modulation index and the voltage is proportional to the square root of the power. The characterization of the V_π is shown in Fig. 134.28 for one of the modulators. The three sections behave similarly, and the V_π increases from ~5 V to ~7 V in the measurement range. V_π values lower than 7 V are acceptable since the voltages required to reach the requested modulation indices are within the range of medium-power solid-state microwave amplifiers. Similar performance was measured on three other phase modulators.

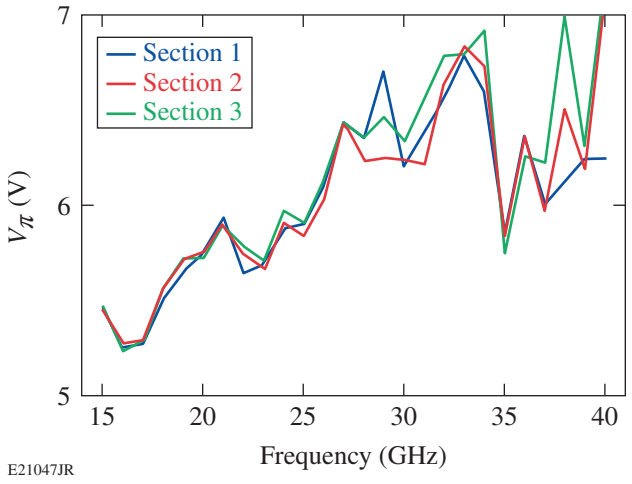

Figure 134.28
Determination of V_π on the three sections of a phase modulator.

For operational characterization of the frequency modulation induced by one modulator, the other drive voltage(s) is (are) turned off, e.g., the drives at f_1 and f_2 are turned off when characterizing the modulation at f_3. An optical spectrum is measured and fitted to determine the modulation index. The drive voltage is increased or decreased via a continuous attenuator, and the measurement is repeated until the measured index matches the requested index within an acceptable uncertainty. Figure 134.29(a) shows the agreement between the measured spectral modes at frequency f_3 with the modes obtained after fitting. Figure 134.29(b) shows the measured optical spectrum when the three drives to the picket-channel phase modulator are turned on. This spectrum agrees very well with the calculated spectrum. For operational characterization of the modulation index at f_{SBSS}, which leads to spectral modes that cannot be distinguished with the available monochromator, an indirect approach was used. The archived spectrum of a cw source, e.g., the spectrum of the same source with all modulations turned off, was used as the instrument response to calculate the optical spectrum that should be measured for a given modulation index. Figure 134.30(a) shows that the bandwidth of the convolved spectrum increases monotonously with the modulation index and is within 1 GHz of the actual bandwidth for modulation indices between 5 and 6 rad. The drive for f_{SSD} is turned off and the modulated spectrum with f_{SBSS} turned on is measured. The modulation drive is precisely set by comparing the measured bandwidth to the bandwidth of the theoretical spectrum corresponding to 5.5 rad convolved with the measured response function. The theoretical spectrum, measured response function, and convolved spectrum are shown in Fig. 134.30(b). The excellent agreement between the measured and convolved spectrum, demonstrated in Fig. 134.30(c), and the monotomic relation between actual bandwidth and measured bandwidth, demonstrated in Fig. 134.30(a), allow us to conclude that the modulation index is adequately set.

3. Extinction of Mach–Zehnder Modulators

MZM extinction is a critical parameter of the pulse-shaping systems because interference between the co-polarized optical waveforms after combination of the picket and main channel can generate large amounts of amplitude modulation. The combined field from the two pulse-shaping channels is

$$p(t) = p_1(t) + b_1(t) + p_2(t) + b_2(t), \tag{3}$$

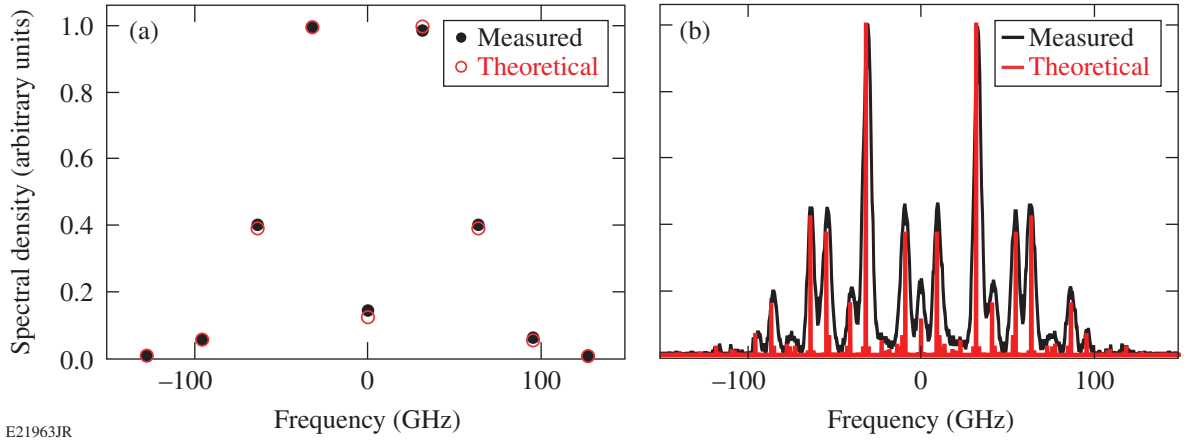

Figure 134.29
(a) Example of a measured spectrum (solid black circles) and fit (open red circles) for the modulation frequency f_3, (b) measured and theoretical optical spectra when the three multi-FM drives are turned on.

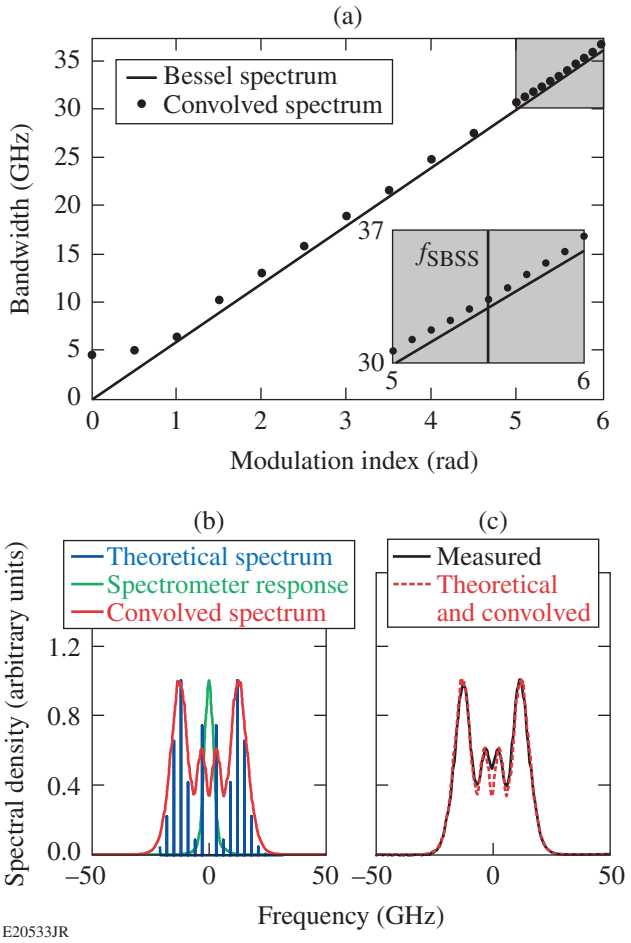

Figure 134.30

(a) Plot of the FWHM of the spectrum obtained by convolution of the measured monochromator response with the theoretical spectrum of a monochromatic source after phase modulation at f_{SBSS}. The inset shows a close-up of the range of modulation index between 5 and 6 rad. (b) Theoretical spectrum of a phase-modulated field at 3 GHz with a modulation index of 5.5 rad, measured response function of the spectrometer, and spectrum obtained by convolution of these two spectra. (c) Comparison of the measured spectrum with the convolved spectrum calculated with the nominal SBSS specifications.

where p_1 and p_2 are the fields of the two shaped pulses, b_1 is the field leakage of channel 1, and b_2 is the field leakage of channel 2. p_1 and p_2 are finite-duration pulses that are not overlapping because the two channels are timed to generate distinct pulse shapes; p_1 and p_2 are equal to zero during b_1 and b_2, respectively. With these definitions, the power is

$$P(t) = P_1(t) + P_2(t) + 2\mathrm{Re}\left[p_1(t)b_2^*(t)\right] + 2\mathrm{Re}\left[p_2(t)b_1^*(t)\right] + 2\mathrm{Re}\left[b_1(t)b_2^*(t)\right] + B_1(t) + B_2(t), \quad (4)$$

where P_1 and P_2 are the shaped pulses of interest, $p_1 b_2^*$ and $p_2 b_1^*$ are the interference of each shaped pulse with the background leakage from the other channel (the main source of noise), and the other terms correspond to the power and interference of the backgrounds (usually negligible). A channel with extinction ratio R leads to a modulation with peak-to-valley amplitude equal to $4\sqrt{R}$ at times when the pulse generated by the other channel has a power equal to 1. This modulation can be highly detrimental: for $R = 20$ dB, the resulting noise is 40%, and increasing R to 40 dB decreases the peak-to-valley noise to 4%, still negatively impacting the system performance. If the same monochromatic laser is used in the two channels, the self-interference will manifest itself as an energy variation from shot to shot, owing to the slow phase drift between the two channels. If two distinct lasers with an optical frequency difference Δf_{12} are used, the interference is a time-varying amplitude modulation of the optical pulse at the frequency Δf_{12}.

The two cascaded MZM's in each channel ensure that the intrinsic extinction ratio is higher than 40 dB, assuming that the corresponding voltage biases are adequately set. The pulse-shaping systems are calibrated for optimal biasing on each MZM. The front end is built with two distinct monochromatic lasers that are spectrally tuned to make the frequency of their interference easily measurable, i.e., distinct from all the microwave frequencies potentially present in the system (all the frequencies in Table 134.V and the sum and differences of all the frequencies present in a given channel), within the bandwidth of the photodetection system (lower than 45 GHz). The frequency of the offset must be small enough that the two channels essentially have the same central wavelength to avoid impacting amplification and frequency conversion to the UV and allow for identical dispersion compensation. The beams corresponding to the two channels are spatially offset in the far field after the SSD grating because of the angular dispersion. The beam corresponding to the broadest spectrum was chosen for alignment because of the more-stringent alignment requirement to avoid spectral clipping by pinholes in the far field. A frequency approximately equal to 5 GHz was chosen. The seed lasers are spectrally tuned by temperature-controlled fiber Bragg gratings with a spectral drift much smaller than 1 GHz over extended periods of time. The frequency offset is quite stable once set. Figure 134.31 shows examples of waveforms measured with proper biasing and with an intentional bias offset. The bias voltage of the two MZM's in each channel is optimized daily by measuring their transmission as a function of the voltage and determining the voltage for minimal transmission. Bias drift caused by charge accumulation is avoided by temporal alternation of the bias between the

optimal value in a time interval encompassing the shaped pulse and another value to set the time-averaged voltage to zero. No interference between channels has been observed with these pulse-shaping systems and procedures and no fail-safe system actively detecting the interference was implemented because of the reliability and stability of this approach, which is also used for pulse shaping on OMEGA[8] and OMEGA EP.[12]

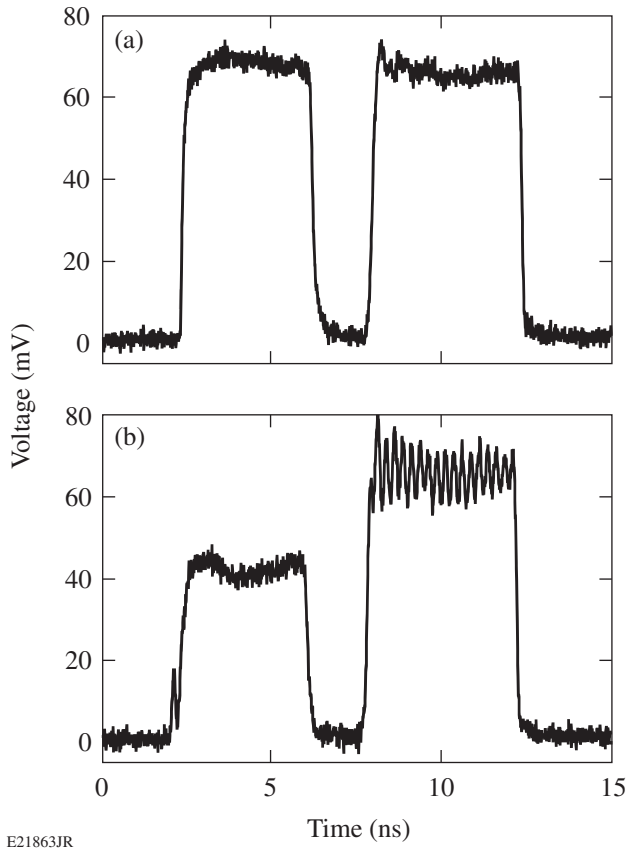

Figure 134.31
Measurement of the pulse shape obtained by combining the picket channel (first pulse) and the main channel (second pulse) in (a) optimal biasing conditions and (b) when the bias of the gate MZM of the picket channel is purposely offset by $\sim V_{\pi}/10$. In the latter case, the amplitude of the first pulse is reduced because of the lower transmission, and AM at ~5 GHz is present on the second pulse because of the increased background.

4. Dispersion Compensation

Dispersion compensation is optimized by first accounting for all sources of chromatic dispersion in the full laser system, from the fiber-coupled phase modulators to the end of the large Nd:glass amplifiers, with optical fibers in the front end being the largest contributor. The two channels in the front end are symmetric, and optimal compensation is expected to be reached for these two systems for the same setting of the dispersion compensator. A 100-m PZ patchcord was initially installed between the front end and the NIF PAM, based on an estimate of the dispersion of the fiber in the front end and the single-grating compressor. Various lengths of PZ fiber were added between the output of the regenerative amplifier and the temporal diagnostic, and the resulting amplitude noise was estimated on a pulse from the picket channel with the three multi-FM modulations turned on (Fig. 134.32). Dispersive propagation has the same effect on the AM whether it occurs before or after the regenerative amplifier in the absence of nonlinearity in that amplifier. Once the optimal fiber length was determined, the corresponding patchcords were placed between the front end and the amplifier to optimize the the amplified signal propagating in the laser system. It is not known if the propagation in the regenerative amplifier is perfectly linear, but no siginificant difference in the measured AM was found when dispersion compensation was adjusted before or after the amplifier.

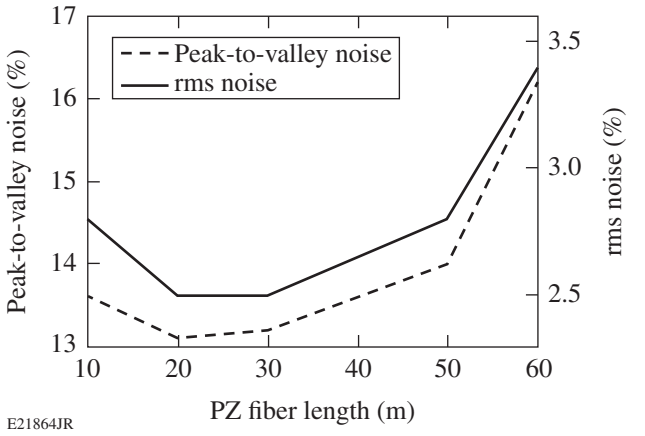

Figure 134.32
Amplitude noise [dashed line: peak-to-valley noise; solid line: rms (root-mean-square) noise] measured as a function of the length of the polarizing (PZ) fiber added before photodetection.

5. Amplitude Compensation

Spectral amplitude compensation is performed by tuning the two angles of the birefringent calcite plate relative to the incident beam. Initial tests and setup used measurements obtained with a spectrometer: the spectrum at the output of the regenerative amplifier is monitored as the plate is tuned by an operator, and the match between the measured spectrum and the expected spectrum (e.g., the spectrum of the pulse with f_1, f_2, and f_3 on) is used as feedback. Figure 134.33 compares the optical spectrum measured after the phase modulator and after the regenerative amplifier. These two optical spectra are indistinguishable and are in excellent agreement with the

theoretical spectrum. Although some amplitude modulation of the spectrum might still be present (beyond the measurement capability in the spectral domain), the time-domain amplitude-noise measurements presented in the next section indicate that the spectral gain tilt in the fiber amplifiers and the regenerative amplifier are adequately compensated. During operation, the amplitude noise measured in the time domain is used as the feedback mechanism. The rf spectrum of the measured waveform (e.g., a square pulse with all multi-FM frequencies turned on at the output of the regenerative amplifier) is calculated in real-time and an operator minimizes the observed rf tones. The amplitude noise on the waveform is then determined. The measured amplitude noise must be below 20% peak-to-valley, as required by a noise budget made for the entire OMEGA EP Laser System. Values of the order of 15% are typical for the peak-to-valley noise, corresponding to rms noise of the order of 3%. The amplitude compensator is stable enough for operation without active stabilization: the amplitude noise was observed over several days without significant increase.

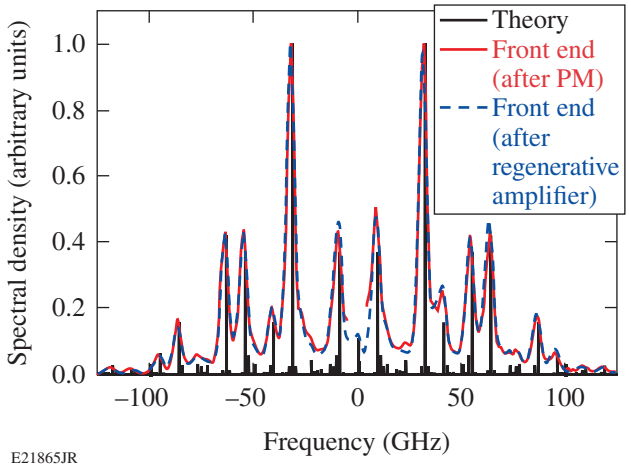

Figure 134.33
Optical spectrum corresponding to a pulse with the three multi-FM frequencies calculated (solid black line), measured after the phase modulator (PM) (solid red line), and measured after the regenerative amplifier (dashed blue line). The measurements were performed with a grating spectrometer having a resolution of 5 GHz. The spectral density data between –5 GHz and +5 GHz after the phase modulator have been removed because the data in that range are corrupted by the cw leakage from the AOM integrated by the detector at the Fourier plane of the spectrometer.

6. Amplitude-Noise Measurements

Amplitude-noise measurements were routinely performed at the output of the regenerative amplifier in the PAM. Quantifying the amplitude noise is crucial for the operation of a large-scale laser system because AM increases the peak power incident on the optical components for a given energy. A power increase can lead to higher nonlinearity experienced by the optical pulse and to optical damage. This amplifier operates at 1 Hz, allowing for the acquisition of a sufficient set of data for statistical analysis. Data similar to that presented in Fig. 134.27 are used: a set of 50 successive waveforms is measured, a temporal range where the pulse shape is not rapidly varying (i.e., avoiding the sharp leading and trailing edges) is isolated, the pulse shape over that range is normalized by a low-order fit, the rms and peak-to-valley variations of the normalized pulse are determined, and the global rms and peak-to-valley noise are obtained by averaging the values determined for each pulse. Using this procedure, the data of Fig. 134.27(a) for the main pulse lead to rms and peak-to-valley noise of 2.3% and 13.2%, respectively. Using the same procedure on a 1-ns pulse from the picket channel leads to similar values for the rms and peak-to-valley noise, 2.8% and 13.5%, respectively. The remaining noise can be attributed to measurement noise, imperfect amplitude and dispersion compensation, propagation effects in polarization-maintaining fibers, and etaloning in optical components. Amplitude noise caused by broadband analog-to-digital conversion by the oscilloscope is likely to be the largest contributor: direct measurement of a cw laser with the same photodetection led to rms and peak-to-valley amplitude noise of 1.6% and 9.6%, respectively, in a 3-ns time window. The measured noise is acceptable, considering the noise budget for the entire laser system, which requires less than a 20% peak-to-valley noise in the front end. Apart from the broadband noise from the photodetection system, the spectrum of the measured waveforms typically has low-density tones at the modulation frequencies. A parabolic spectral-amplitude modulation and high-order spectral phase modulations can lead to intermodulation components, i.e., sidebands of equal amplitude at the sum and difference of the modulation frequencies. The sum terms (e.g., $2f_3 \sim 63.8$ GHz and $f_1 + f_3 \sim 53.1$ GHz for the picket channel) are beyond the photodetection bandwidth, but the difference terms (e.g., $f_3 - f_1 \sim 10.7$ GHz) correspond to a high value of the detection frequency reponse. No significant spectral components at the difference frequencies have been observed when the amplitude compensator is adequately set, giving confidence in the spectral-amplitude compensation and showing that the impact of high-order terms in the spectral phase is negligible. These aspects will be studied in detail in the future. These experiments confirm that AM compensation to an acceptable noise level can be obtained simultaneously on the two channels.

A diffraction grating mounted inside the PAM is required for SSD: the angular dispersion (frequency versus wave vector

in the near field) of a phase-modulated pulse leads to a time-varying speckle distribution in the far field of the focusing lens after frequency conversion and random spatial-phase modulation from a phase plate.[6] The current system has a 1700-l/mm diffraction grating mounted in the Littrow configuration. The groove density is a trade-off between smoothing, pulse-shape, and laser requirements. A larger angular dispersion leads to more smoothing in the far field, but it temporally broadens the pulse shape. Angular dispersion widens the far field of the optical pulse, which can disrupt the propagation of the amplified pulse in vacuum spatial filters that re-image the beam throughout the laser system. Pinholes in vacuum spatial filters are designed to spatially filter the high spatial frequencies of the beam as it propagates in the laser system, but they can lead to spectral clipping of the spectrum of angularly dispersed phase-modulated pulses, which adds amplitude modulation in the time domain.

The tightest pinhole in the entire laser system is located in the PAM. The full optical spectrum was observed in the far field after that pinhole,[13] but amplitude noise was measured at an image plane of the diffraction grating after this pinhole to confirm that no amplitude noise is added to the front-end pulses. A PZ fiber was used to probe the laser beam, which has an ~2-cm size in that plane. Figure 134.34 displays the amplitude noise as a function of the longitudinal distance relative to a reference position. The noise is expected to be minimal at the image plane and to increase before and after the image plane.[20] The minimum noise should be equal to the noise before angular dispersion. The measured rms and peak-to-valley noise at the output of the regenerative amplifier (i.e., before the diffraction grating) were 2.8% and 14.2%, respectively, in good agreement with the minimum values observed at the image plane, 2.5% and 13.5%. The lower noise observed at the image plane is not fully understood, but it could be a result of a slight mismatch in the dispersion compensation: propagation away from the image plane is equivalent to second-order dispersion;[20] therefore a signal with a small amount of dispersion has lower amplitude noise when measured at a longitudinal distance slightly offset from the image plane.

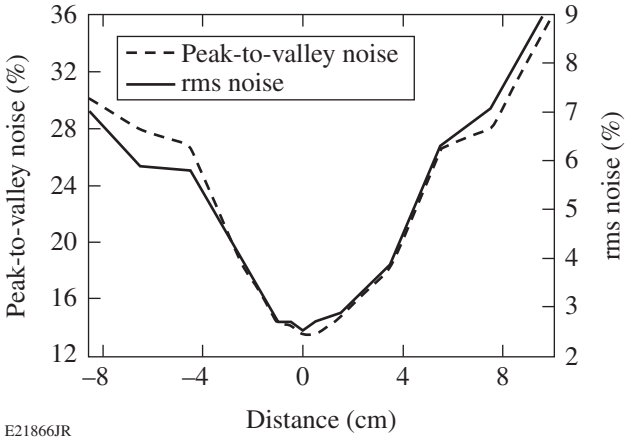

Figure 134.34
Amplitude noise (dashed line: peak-to-valley noise; solid line: rms noise) measured as a function of the longitudinal distance close to an image plane of the diffraction grating.

Conclusion

The front end demonstrates the use of high-bandwidth pulse shaping and phase modulation for high-energy laser systems. In particular, high-bandwidth, three-section phase modulators have been calibrated at microwave frequencies up to 40 GHz and routinely used at frequencies ranging from 3 to 32 GHz. The optical combination of optical pulses with different pulse shapes and phase modulations has made it possible to generate complex optical fields. Fail-safe systems have been used to detect the presence of adequate phase modulation and sufficient optical power at the output of the front end. A grating compressor and a Lyot filter have been used to decrease the FM-to-AM conversion caused by dispersive propagation and spectrally dependent amplifier gain. Pulse shape and noise measurements at frequencies up to 45 GHz have confirmed the accuracy of the compensation and adequacy of the system for seeding a high-energy laser system.

The front end has been used to generate seed pulses with a variety of shapes and phase modulations for the OMEGA EP Laser System to study the amplification, frequency-conversion, and beam-smoothing properties of these pulses.[13] The front end and associated technologies have made it possible to validate the multi-FM approach for beam smoothing and its application to a large-scale laser system. Implementation on a multibeam system will require significant multiplexing of the resources in the front end (particularly cw lasers, AWG's, and modulators) to minimize the associated space and cost. The 48 PAM's on the NIF might require seeding with optical pulses that have different shapes and central wavelength[1,11] requiring different front-end outputs, but building 48 front ends identical to the one described here would be prohibitive.

ACKNOWLEDGMENT

The authors thank M. W. Bowers, D. F. Browning, and G. V. Erbert (Lawrence Livermore National Laboratory) for fruitful discussions and assistance with NIF-related equipment, and T. J. B. Collins, J. H. Kelly, B. E. Kruschwitz, J. A. Marozas, and A. Shvydky (LLE) for fruitful discussions. This work was supported by the U.S. Department of Energy Office of Inertial Confinement Fusion under Cooperative Agreement No. DE-FC52-08NA28302, the Univer-

sity of Rochester, and the New York State Energy Research and Development Authority. The support of DOE does not constitute an endorsement by DOE of the views expressed in this article.

REFERENCES

1. C. A. Haynam *et al*., Appl. Opt. **46**, 3276 (2007).
2. N. Fleurot, C. Cavailler, and J. L. Bourgade, Fusion Eng. Des. **74**, 147 (2005).
3. J. D. Lindl, Phys. Plasmas **2**, 3933 (1995).
4. J. D. Kilkenny, S. G. Glendinning, S. W. Haan, B. A. Hammel, J. D. Lindl, D. Munro, B. A. Remington, S. V. Weber, J. P. Knauer, and C. P. Verdon, Phys. Plasmas **1**, 1379 (1994).
5. R. L. McCrory, D. D. Meyerhofer, R. Betti, R. S. Craxton, J. A. Delettrez, D. H. Edgell, V. Yu Glebov, V. N. Goncharov, D. R. Harding, D. W. Jacobs-Perkins, J. P. Knauer, F. J. Marshall, P. W. McKenty, P. B. Radha, S. P. Regan, T. C. Sangster, W. Seka, R. W. Short, S. Skupsky, V. A. Smalyuk, J. M. Soures, C. Stoeckl, B. Yaakobi, D. Shvarts, J. A. Frenje, C. K. Li, R. D. Petrasso, and F. H. Séguin, Phys. Plasmas **15**, 055503 (2008).
6. S. Skupsky, R. W. Short, T. Kessler, R. S. Craxton, S. Letzring, and J. M. Soures, J. Appl. Phys. **66**, 3456 (1989).
7. J. E. Rothenberg, J. Opt. Soc. Am. B **14**, 1664 (1997).
8. T. R. Boehly, D. L. Brown, R. S. Craxton, R. L. Keck, J. P. Knauer, J. H. Kelly, T. J. Kessler, S. A. Kumpan, S. J. Loucks, S. A. Letzring, F. J. Marshall, R. L. McCrory, S. F. B. Morse, W. Seka, J. M. Soures, and C. P. Verdon, Opt. Commun. **133**, 495 (1997).
9. S. Skupsky and R. S. Craxton, Phys. Plasmas **6**, 2157 (1999).
10. J. R. Murray *et al*., J. Opt. Soc. Am. B **6**, 2402 (1989).
11. T. J. B. Collins, J. A. Marozas, K. S. Anderson, R. Betti, R. S. Craxton, J. A. Delettrez, V. N. Goncharov, D. R. Harding, F. J. Marshall, R. L. McCrory, D. D. Meyerhofer, P. W. McKenty, P. B. Radha, A. Shvydky, S. Skupsky, and J. D. Zuegel, Phys. Plasmas **19**, 056308 (2012).
12. D. N. Maywar, J. H. Kelly, L. J. Waxer, S. F. B. Morse, I. A. Begishev, J. Bromage, C. Dorrer, J. L. Edwards, L. Folnsbee, M. J. Guardalben, S. D. Jacobs, R. Jungquist, T. J. Kessler, R. W. Kidder, B. E. Kruschwitz, S. J. Loucks, J. R. Marciante, R. L. McCrory, D. D. Meyerhofer, A. V. Okishev, J. B. Oliver, G. Pien, J. Qiao, J. Puth, A. L. Rigatti, A. W. Schmid, M. J. Shoup III, C. Stoeckl, K. A. Thorp, and J. D. Zuegel, J. Phys. Conf. Ser. **112**, 032007 (2008).
13. "Commissioning of a Multiple-Frequency–Modulation Smoothing by Spectral Dispersion Demonstration System on OMEGA EP," published in this volume.
14. V. N. Goncharov, T. C. Sangster, T. R. Boehly, S. X. Hu, I. V. Igumenshchev, F. J. Marshall, R. L. McCrory, D. D. Meyerhofer, P. B. Radha, W. Seka, S. Skupsky, C. Stoeckl, D. T. Casey, J. A. Frenje, and R. D. Petrasso, Phys. Rev. Lett. **104**, 165001 (2010).
15. P. J. Wisoff *et al*., in *Optical Engineering at the Lawrence Livermore National Laboratory II: The National Ignition Facility*, edited by M. A. Lane and C. R. Wuest (SPIE, Bellingham, WA, 2004), Vol. 5341, pp. 146–155.
16. M. Bowers *et al*., in *Solid State Lasers XVI: Technology and Devices*, edited by H. J. Hoffman, R. K. Shori, and N. Hodgson (SPIE, Bellingham, WA, 2007), Vol. 6451, p. 64511M.
17. J. K. Crane *et al*., in *Solid State Lasers for Application to Inertial Confinement Fusion: Second Annual International Conference*, edited by M. L. André (SPIE, Bellingham, WA, 1997), Vol. 3047, pp. 601–609.
18. D. Penninckx *et al*., J. Lightwave Technol. **24**, 4197 (2006).
19. J. E. Rothenberg, D. F. Browning, and R. B. Wilcox, in the *Third International Conference on Solid State Lasers for Application to Inertial Confinement Fusion*, edited by W. H. Lowdermilk (SPIE, Bellingham, WA, 1999), Vol. 3492, pp. 51–61.
20. S. Hocquet *et al*., Appl. Opt. **47**, 3338 (2008).
21. B. Lyot, C. R. Acad. Sci. (Paris) **197**, 1593 (1933).

Mitigation of Two-Plasmon Decay in Direct-Drive Inertial Confinement Fusion Through the Manipulation of Ion-Acoustic- and Langmuir-Wave Damping

Introduction

Two-plasmon decay[1–6] (TPD) is a three-wave–decay instability in which an electromagnetic (EM) wave parametrically decays into two longitudinal (Langmuir) waves. Experimentally, signatures of TPD have been observed in the ionosphere[7] and in laser–plasma interaction experiments.[8,9] In the context of laser fusion, TPD has been identified in both the indirect-[10] and direct-drive[11] approaches.In these schemes, TPD is undesirable because of the anomalous absorption of laser light at densities below the critical density and the potential to accelerate electrons to high energies.[12–16] High-energy electrons can preheat the target and severely degrade performance since efficient implosions require the fuel to remain on a low adiabat.

The linear stability of a single-plane EM wave subject to TPD has been studied for quite some time,[1–6,17,18] although not without controversy regarding its absolute/convective nature in inhomogeneous plasma.[16,19,20] In TPD, a photon decays into two plasmons, fulfilling the frequency- and wave-number–matching conditions, $\omega_0 = \omega + \omega'$, $\vec{k}_0 = \vec{k} + \vec{k}'$, where ω_0 and $\vec{k}_0 \left(k_0 \equiv \left| \vec{k}_0 \right| = \omega_0 \big/ c\sqrt{1 - n_e \big/ n_c} \right)$ are the frequency and wave vector, respectively, of an EM wave in a plasma having an electron number density n_e relative to the critical density $n_c \left[= m_e \omega_0^2 \big/ (4\pi e^2) \right]$ at which EM waves are evanescent. Here, e and m_e are the electron charge and mass, respectively, and c is the speed of light. The quantities ω, ω', $\vec{k}$, and $\vec{k}'$ are the frequencies and wave vectors of the two decay Langmuir waves (LW's) (note that in the literature, the terms "Langmuir wave," "plasma wave," and "plasmon" are used interchangeably). The essential features are described by the temporal TPD growth rate γ (in the presence of LW damping rate ν_e):

$$\gamma = \gamma_0 - \nu_e = \frac{\vec{k} \cdot \vec{v}_{osc}}{4} \frac{\left[\left(\vec{k}_0 - \vec{k} \right)^2 - k^2 \right]}{k \left| \vec{k}_0 - \vec{k} \right|} - \nu_e , \qquad (1)$$

where $\vec{v}_{osc} = e\vec{E}_0 \big/ \omega_0 m_e$ is the oscillation velocity of an electron in the electric field of the plane EM wave $\vec{E}_0$. The relation between $k_\parallel$ and $k_\perp$ (parallel and perpendicular components of $\vec{k}$ with respect to $\vec{k}_0$) corresponding to maximum growth defines a hyperbola in k space, $\vec{k}_\perp^{\,2} = k_\parallel (k_\parallel - k_0)$. From Eq. (1) it can be seen that two-plasmon decay cannot be studied in one spatial dimension (since $\vec{k}_0 \cdot \vec{v}_{osc} = 0$ for EM waves). For this reason most, if not all, numerical calculations to date have been performed in 2-D in the plane of maximum growth, i.e., the plane of polarization (such is the case here).

In experiments utilizing multiple overlapping laser beams, the instability is believed to be driven cooperatively by several beams[21] through the sharing of common TPD waves.[22–24] To retain this feature in two spatial dimensions, all calculations were performed with two EM waves arranged symmetrically about the density gradient with angles of ±23° (as in previous work[25–28]).

Parametric instabilities occur when the pump amplitude exceeds a threshold that depends on collisional effects, Landau damping, and plasma inhomogeneity. The effect of collisional damping of LW's was not emphasized in earlier theoretical works. This was either for simplicity or motivated by the dominance of inhomogeneity in experiments. In this work, all three effects are included.

In several previous studies of the nonlinear saturation of electromagnetically driven parametric instabilities, the level of LW excitation was seen to depend on the ion-acoustic–wave (IAW) damping rate. This was reported in detail in simulations of the nonlinear stage of stimulated Raman scattering (SRS) in laser hot spots,[29] in regimes of low Landau damping of the Langmuir wave. It was found that the SRS reflectivity increased linearly with the IAW damping rate. In general, the development of Langmuir turbulence and collapse physics is known to depend on the ion-acoustic damping rate.[30–32] These earlier results suggest that TPD could be less severe in materials with high collisional damping of LW and weak collisional damping of IAW (experimental evidence suggests TPD suppression in mid-Z targets[33,34]). More importantly, there could be practical implications for directly driven inertial confinement fusion (ICF) since Betti[35] and Lafon[36] have shown that igniting targets

can be designed using mid-Z ablators at the megajoule (MJ) scale. These could provide an alternate path to ignition should TPD preheat be too high in directly driven designs using plastic (CH) ablators.[37]

The following sections describe the numerical "*QZAK*" model and explain in detail the approximations that have been made; the properties of linear stability; and the anomalous absorption of hot-electron production that is characteristic of the nonlinearly saturated state, emphasizing the sensitivity to plasma conditions, followed by a summary and discussion.

Numerical Simulation of TPD Growth and Saturation in Inhomogeneous Collisional Plasma

Zakharov models[38,39] have been used extensively to study the evolution of Langmuir waves and their nonlinear coupling with ion-acoustic waves, particularly LW self-focusing and collapse. The Zakharov model describes both three- and four-wave interactions,[40] which have been used to study strong Langmuir turbulence[41,42] relevant to laboratory plasmas,[43,44] ionospheric modification experiments,[30,31,45] laser-plasma experiments,[32,46,47] and pulsar radio emissions.[48] The weak turbulence regime[40] assumes random phase interactions between the linear modes and does not accurately describe the results from Zakharov models[49] because of strong turbulence effects. The strong turbulence regime[41,42] involves phase-coherent interactions including self-focusing, cavitation, and collapse, which can coexist[50] with wave–wave processes such as the Langmuir decay instability (LDI).[40,51] The key approximation of the model is that of temporal enveloping. The fast variations ($\partial/\partial t \sim \omega_{pe}$) of the LW electrostatic field are explicitly removed, and the slow variations ($\partial/\partial t \ll \omega_{pe}$) are followed by the complex-valued function, or "envelope" $\vec{E}_1(\vec{x},t)$. For example, the physical LW electrostatic field $\vec{E}$ is given by $\vec{E} = 1/2\left[\vec{E}_1(\vec{x},t)\exp\left(-i\omega_{pe}t\right) + \text{c.c.}\right]$, which is centered at the reference plasma frequency $\omega_{pe} = (4\pi n_0 e^2/m_e)^{1/2}$.

In the extended quasi-linear Zakharov model of TPD,[32,46] multiple envelopes are defined by an expansion in harmonics of the reference electron plasma frequency ω_{pe} (which is itself defined in terms of a reference density n_0). This is useful since TPD is localized between a narrow range of densities in the neighborhood of $n_c/4$. Two envelopes and a low-frequency term are sufficient for the present analysis,[52] shown below for the plasma current:

$$\vec{J}(\vec{x},t) = \vec{J}_0(\vec{x},t) + \frac{1}{2}\left[\vec{J}_1(\vec{x},t)\exp\left(-i\omega_{pe}t\right) + \vec{J}_2(\vec{x},t)\exp\left(-i2\omega_{pe}t\right) + \text{c.c.}\right], \quad (2)$$

where $\left|\partial\vec{J}_1/\partial t\right| \ll \omega_{pe}\left|\vec{J}_1\right|$, etc. The term proportional to $\vec{J}_1$ is centered at the plasma frequency ω_{pe} and therefore close to one half of the laser frequency. The longitudinal component of $\vec{J}_1$ drives the first Zakharov equation (LW response), while the transverse component is responsible for the $\omega_0/2$ radiation[53–56] (including SRS[29] and the mixed-polarization, high-frequency hybrid instability[18]). The term $\vec{J}_2$, near twice the plasma frequency $2\omega_p$ and therefore close to the laser frequency ω_0 (with mismatch $\Delta\omega \equiv \omega_0 - 2\omega_{pe} \ll 2\omega_p$), modifies the laser propagation and is the source of pump depletion. [The subscript "0" denoting the laser frequency ω_0 throughout is not to be confused with the subscript "0" in Eq. (2), where it denotes terms with a frequency far below the electron plasma frequency.] The plasma response to low-frequency terms is assumed to be quasi-neutral $\delta n = \delta n_e \approx Z\delta n_i$, where Z is the ion charge and δn_e and δn_i are the electron- and ion-density perturbations, respectively. Inhomogeneous plasmas with a weak density gradient are investigated by the addition of a static term describing density perturbations from the reference density (as described in Russell *et al.*[46]) and by a constant flow velocity $\vec{u}_0$.

The primary disadvantage of a fluid-moment model such as the Zakharov model[32,46] is the lack of nonlinear kinetic saturation mechanisms. Although often derived from the plasma fluid equations,[57] *ZAK*[25,26,32,46] and also the *QZAK* (described below) and RPIC numerical codes (described in Vu *et al.*[25]) can be shown to be direct consequences of the Vlasov equation by the use of a multiple time-scale analysis and the requirement that certain parameters remain "small," e.g., $|\vec{E}_1|^2/(4\pi n_0 T_e) < 1$, $\delta n_0/n_{e0} < 1$, and $k\lambda_{De} < 1$ (Ref. 58), where

$$\lambda_{De} = \sqrt{T_e/(4\pi n_0 e^2)}$$

is the electron Debye length. The *ZAK* model of TPD[25,26,32,46] [which includes linear wave–particle interactions (Landau damping)] is improved upon by *QZAK*, which evolves the electron-distribution function in the quasi-linear approximation. RPIC is a time-enveloped particle-in-cell (PIC) code that improves on *QZAK* since it does not make the quasi-linear approximation.[25] When the proper conditions are met, the predictions of RPIC and *QZAK* should agree. Since PIC codes generally make no small-parameter assumptions, they can be used to check the validity of *QZAK* calculations. This was discussed in a recent paper by Vu *et al.*[27] using the code RPIC and also briefly in **Confirmation of the Sensitivity to**

Ion-Acoustic Damping Using RPIC Calculations (p. 122) (unlike typical PIC codes, RPIC assumes that a separation of time scales exists, which could in some sense be considered as an expansion parameter).

The Extended Quasi-Linear Zakharov (QZAK) Model of TPD

The harmonic decomposition in ω_{pe} suggested by Eq. (2) leads to the following equation for EM waves having frequencies of $2\omega_{pe}$ (i.e., near that of the laser pump):

$$\left\{-2i\left(2\omega_p\right)\left(\partial_t+\nu_{2,T}\right)+c^2\nabla^2+\left(2\omega_{pe}\right)^2 \times\left[1-\left(n_0+\delta N+\delta n\right)\Big/\left(4n_0\right)\right]\right\}\vec{E}_{2,T} =\left(e\big/m_e\right)\left[\left(\nabla\bullet\vec{E}_1\right)\vec{E}_1\right]_T. \quad (3)$$

This equation describes the laser pump field, which is imposed as a boundary condition, together with other components resulting from nonlinearities. The relation of the laser electric field $\vec{E}_0$ to the transverse component of the second-harmonic envelope is given by $\vec{E}_0=\vec{E}_{2,T}\exp\left(i\Delta\omega t\right)$, where $\Delta\omega$ represents the slight frequency mismatch that arises because n_0 (= 0.23 n_c) is slightly less than $n_c\big/4$ (to allow for the density gradient). The subscript "T" denotes the transverse component, which is most easily expressed in Fourier space: $\vec{E}_{2,T}\left(\vec{k}\right)=\left(\vec{I}-\vec{k}\vec{k}\big/k^2\right)\bullet\vec{E}_2\left(\vec{k}\right)$. The quantity $\nu_{2,T}$ is the collisional damping rate of transverse waves $\nu_{2,T}\approx\left(n_0\big/n_c\right)\nu_{ei}$ that gives rise to inverse-bremsstrahlung absorption,[59] where

$$\nu_{ei}\approx 3\times10^{-6}\log\left(\lambda\right)\left(n_e\big/1\,\mathrm{cm}^{-3}\right)Z\Big/\left(T_e\big/1\,\mathrm{eV}\right)^{3/2}$$

is the usual electron–ion collision frequency (in s^{-1}), where $\log(\lambda)$ is the Coulomb logarithm and T_e is the electron temperature. The term $\delta N\left(\vec{x}\right)$ is a small, nonevolving density perturbation describing the weakly inhomogeneous density,[46] while $\delta n\left(\vec{x},t\right)$ is the quasi-neutral piece that is driven by the ponderomotive pressure of the high-frequency fluctuations. The total low-frequency density is given by $n_e\left(\vec{x},t\right)=n_0+\delta N\left(\vec{x}\right)+\delta n\left(\vec{x},t\right)$ with the assumption that both $\delta N/n_0\ll1$ and $\delta n/n_0\ll1$. In all calculations presented here, δN varies linearly in the x direction only (the "longitudinal" direction), while the initial density scale length $L_n\equiv\left[\mathrm{d}/\mathrm{d}x\,\ln(n_0+\delta N)\right]^{-1}=330\,\mu$m (at box center) unless otherwise noted. The right-hand side of Eq. (3) describes the depletion of $\vec{E}_{2,T}$ as a result of its decay into electrostatic waves $\vec{E}_1$.

In two-plasmon decay it is likely that the background particle-distribution functions are significantly changed during the nonlinear stage of the instability. High levels of LW's or IAW's can lead to important modifications of the electron and ion distribution functions; these modifications, in turn, affect the nonlinear levels of the wave excitation. A multiple time-scale analysis of the spatially averaged electron Vlasov equation, together with a quasi-neutral low-frequency response, leads to the same coupled envelope equations for the electrostatic response:

$$\nabla\bullet\left[2i\omega_{pe}\left(D_t+\nu_e\circ\right)+3v_e^2\nabla^2-\omega_{pe}^2\left(\delta n+\delta N\right)\big/n_0\right]\vec{E}_1 =\left(\frac{e}{4m_e}\right)\nabla\bullet\left[\nabla\left(\vec{E}_0\bullet\vec{E}_1^*\right)-\vec{E}_0\nabla\bullet\vec{E}_1^*\right]e^{-i\Delta\omega t}+S_E, \quad (4)$$

(described by $\vec{E}_1$) and for the low-frequency response

$$\left[D_t^2+2\nu_i\circ D_t-c_s^2\nabla^2\right]\delta n=\frac{Z}{16\pi m_i}\nabla^2\left(\left|\vec{E}_1\right|^2+\frac{1}{4}\left|\vec{E}_0\right|^2\right), \quad (5)$$

as described previously[32] [with the exception of the terms representing inhomogeneity (discussed in more detail below)]. The important difference is that the linear response [i.e., the coefficients on the left-hand side of Eqs. (4) and (5)] varies over times that are long compared with the variation of the envelopes. In both Eqs. (4) and (5), $D_t\equiv\left(\partial_t+\vec{u}_0\bullet\nabla\right)$ is the convective derivative and the term S_E is the time-random-phase Čerenkov noise source[60] for Langmuir waves as described in Russell *et al.*[46] Noise enters the acoustic-wave equation only through the LW ponderomotive force. In Eq. (4), $\nu_e=\nu_{coll}+\gamma_L$ is the sum of the collisional and Landau damping for LW's (which evolves in time) and whose dispersion depends on the electron thermal velocity $v_e=\sqrt{T_e\big/m_e}$. The first term on the right-hand side is the longitudinal part of the nonlinear current $\vec{J}_1$, which drives density perturbations with frequencies close to ω_{pe}. In Eq. (5), $c_s=\left(ZT_e\big/m_i\right)^{1/2}\left(1+\gamma_iT_i\big/ZT_e\right)$ is the speed of ion-acoustic waves that damp with the rate ν_i, where $\gamma_i\approx3$, m_i, and T_i are the ion ratio of specific heats, mass, and temperature, respectively. The first term on the right-hand side describes the low-frequency ponderomotive forces of Langmuir and electromagnetic fluctuations.

As in the work of Sanbonmatsu *et al.*,[61] the slow temporal evolution of the spatially averaged electron distribution func-

tion $\langle F_e \rangle$, which is a function of velocity $\vec{v}$ and time t only, is governed by a Fokker–Planck equation:

$$\partial_t \langle F_e \rangle + \nu(\vec{v})\left(\langle F_e \rangle - F_0\right) = \partial_{\vec{v}} \cdot \left[\hat{D}(\vec{v}) \cdot \partial_{\vec{v}} \langle F_e \rangle\right] + \partial_{\vec{v}} \cdot (\delta\hat{D} \cdot \vec{v}) \langle F_e \rangle / v_e^2 + \hat{\sigma}_{IB}\left[\left|\vec{E}_1\right|^2\right] + \hat{\sigma}_{IB}\left[\left|\vec{E}_2\right|^2\right]. \quad (6)$$

The diffusion coefficient $\hat{D}(\vec{v})$ is given by the usual quasi-linear form:

$$\hat{D}(\vec{v}) \approx D_{QL}(\vec{v}) = \frac{\pi e^2 |\Delta\vec{k}|}{2m_e^2 \Delta k_x \Delta k_y} \sum_{k:\left(\omega_{pe} - \vec{k}\cdot\vec{v} = 0\right)} \frac{\vec{k}\vec{k}}{|\vec{v}|} \left|\psi_1(\vec{k})\right|^2, \quad (7)$$

where $\psi_1(\vec{k})$ is the electrostatic potential $\vec{E}_1(\vec{k},t) = -i\vec{k}\psi_1(\vec{k},t)$. The quantity $\Delta\vec{k}$ is the wave-vector spacing along the line in k space defined (for given $\vec{v}$) by the constraint $\omega_{pe} - \vec{k}\cdot\vec{v} = 0$, while Δk_x and Δk_y are equal to $2\pi/L_x$ and $2\pi/L_y$, respectively. The quantities L_x and L_y are the lengths of the simulation domain in the x and y directions. The second term on the left-hand side of Eq. (6) involving the term $\nu(\vec{v}) \equiv s_x |v_x| / L_x + s_y |v_y| / L_y$, with s_x, s_y taking the values of either 0 or 1, is the result of spatially averaging the advective term in the kinetic equation for the distribution function over the domain in which Eqs. (4) and (5) are solved: $[0, L_x] \times [0, L_y]$ (Ref. 61). If the calculation is periodic in the y direction, for example, the corresponding contribution to this term vanishes (i.e., $s_y = 0$). It is assumed that the outgoing distribution of velocities at each spatial boundary is the same as the spatially averaged distribution function.[27] The term $\delta\hat{D}$ entering into Eq. (6) has the same definition as $\hat{D}$ in Eq. (7), but it is calculated with the initial LW noise spectrum to ensure that $\langle F_0 \rangle$ is a steady-state solution to the undriven Eqs. (4)–(7) as described in Sanbonmatsu *et al.*[61] *Ad hoc* differential operators $\hat{\sigma}_{IB}\left[\left|\vec{E}_1\right|^2\right]$, $\hat{\sigma}_{IB}\left[\left|\vec{E}_2\right|^2\right]$, which have been added to Eq. (6), are intended to correspond to the collisional absorption of LW and EM waves, described by the envelopes $\vec{E}_1$ and $\vec{E}_2$, respectively, since they can become important for collisional plasmas. The form of these operators is left unspecified.

The distribution function $\langle F_e \rangle(\vec{v},t)$, which evolves according to Eq. (6) starting from the initial condition $\langle F_e \rangle(\vec{v},t) = F_0$, redefines the linear response of the plasma in time through the linear susceptibilities that modify the frequencies (e.g., c_s and v_e) and damping rates (γ_L) of the linear modes. In the current implementation of *QZAK*, only the electron Landau damping [entering into ν_e of Eq. (4)] is evolved:

$$\gamma_L(\vec{k},t) \approx \frac{\pi\omega_{pe}^2}{k^2} \int d\vec{v}\vec{k} \cdot \partial_{\vec{v}} \langle F_e \rangle(\vec{v},t) \delta\left(\omega_{pe} - \vec{k}\cdot\vec{v}\right). \quad (8)$$

Equations (3)–(8) are solved in two spatial dimensions by a split-step method. Equation (3) is currently solved by neglecting collisional absorption, pump depletion, and nonlinear terms (i.e., trivially), while Eqs. (4) and (5) are advanced by a pseudospectral method:[62,63] All the linear propagation terms of Eqs. (4) and (5) are computed in Fourier space (Landau damping can be easily written in k space), while the nonlinear term in Eq. (4) is updated in real space. Both the transverse (y direction) and longitudinal (x direction) boundary conditions for the fields $\vec{E}_1$ and δn are assumed to be periodic. Physically, the longitudinal direction should be open. In the longitudinal direction the LW's are strongly damped, however, in the low-density region due to Landau damping, and they are evanescent beyond the quarter-critical density, so there is actually negligible cross-communication and differences between periodic and outgoing boundary conditions should be negligible. Ion fluctuations are strongly damped at both longitudinal boundaries by the addition of a "beach" to ensure there is no recirculation.[29] This can be important for weakly damped IAW.

The distribution function $\langle F_e \rangle$ is updated less frequently than the envelopes by evolving Eq. (6), neglecting the inverse bremsstrahlung operators, using an alternating-direction implicit (ADI) scheme.[64] At each update of Eq. (6), the Landau-damping term γ_L is updated according to Eq. (8). Although Eqs. (6)–(8) have been written here in the nonrelativistic approximation (for clarity), *QZAK* actually solves their relativistic generalization.

A major assumption used in the derivation of Eq. (6) was that the electron-distribution function is well approximated by its spatial average. It is not evident that this should be so, given that the plasma is (weakly) inhomogeneous. However, recent results using the time-enveloped particle-in-cell code RPIC indicate this to be a valid assumption.[27] This important simplification is very beneficial because it makes large-scale simulations of the nonlinear evolution of TPD using Eqs. (3)–(8) practical, particularly in three dimensions. Three-dimensional simulations are important

since it has been demonstrated that the TPD process is driven by the mutual interaction of multiple laser beams.[21,23,24]

The self-consistent set of equations [Eqs. (3)–(8)] reach, in many cases, a statistical steady state in which it is possible to associate a heat flux associated with suprathermal particles and an anomalous absorption because of all the dissipative processes. Solutions to the velocity-space diffusion equation [Eqs. (6) and (7)] allow one to estimate hot-electron production, which is important if connections are to be made with experiment[16,24,65] and other kinetic modeling.[25,27,28,66–68]

Aspects of Linear Stability

Two-plasmon decay in a strictly linearly varying density profile was first found to be convectively unstable using an analysis based on the spatial envelope approximation.[2] Later, Simon *et al*.,[6] arguing that the spatial envelope approximation becomes invalid near the LW turning point, showed that two-plasmon decay of a plane EM wave propagating in the direction of the density gradient is absolutely unstable.[3,6,17,69,70] The correct threshold intensity was obtained by Simon *et al*.[6] and is given approximately by

$$I_{14} \approx 1.4\left(T_e \big/ 2\ \text{keV}\right) \big/ \left(L_n \big/ 330\ \mu\text{m}\right) \qquad (9)$$

for conditions of current experiments,[16] where I_{14} is the laser intensity in units of 10^{14} W/cm^2 and L_n is the density scale length. This threshold condition is plotted in Fig. 134.35. The TPD instability extends to wave numbers outside the region of absolute instability to include modes that have been determined to be convectively unstable,[24,67] with the convective "threshold" intensity a factor of a few times higher for a single-plane EM wave pump.[67] These works[6,24,67] neglected the damping of the decay plasma waves. As can be seen in Fig. 134.35, this is a good approximation since the damping threshold intensity is much smaller than the inhomogeneity threshold at the scale accessible by ~10- to 20-kJ lasers (e.g., OMEGA[71]/OMEGA EP[72]) indicated by the yellow shaded region.

In the opposite (homogeneous) limit, the damping threshold (also shown in Fig. 134.35) is simply given by $\gamma_0 \gtrsim \nu_{ei}/2$ (cf., e.g., Goldman[1,73] or Kruer[74]) since collisional damping $\nu_{coll} \sim \nu_{ei}/2$ greatly exceeds Landau damping γ_L for wave numbers $k \lesssim 0.25\, k_D$ in a Maxwellian plasma $\left(\text{i.e.}, \nu_e \approx \nu_{ei}/2\right)$, where γ_0 is the temporal growth rate and $k_D = 1/\lambda_{De}$ is the Debye wave number. A stability analysis of Eq. (4) performed for a single-plane EM wave and taking $\delta N = 0$ can be shown to give

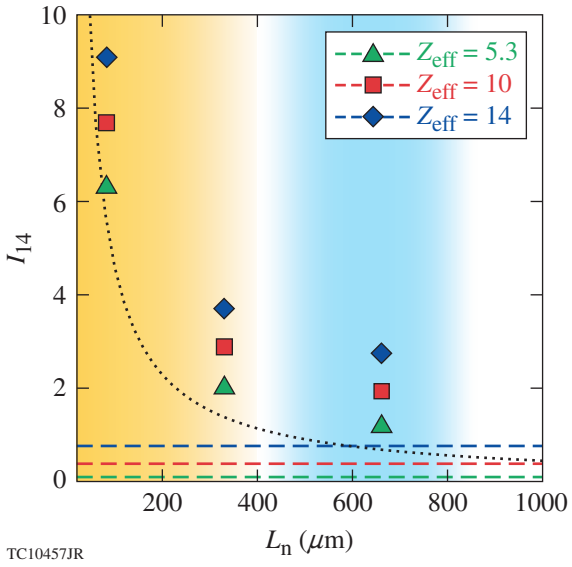

Figure 134.35
The markers show the numerically determined threshold for absolute two-plasmon–decay (TPD) instability of two plane electromagnetic (EM) waves incident at angles of ±23° with respect to a density gradient of scale length L_n for different values of Z_{eff} [and, therefore, collisional Langmuir-wave (LW) damping]. The plotted intensity is the sum of the single-beam intensities. For comparison, the dotted line shows the approximate absolute threshold intensity, in the absence of LW damping, for a single, normally incident plane EM wave[6] as a function of density scale length. The collisional threshold in the absence of plasma inhomogeneity is shown by the horizontal dashed lines for various Z_{eff}. In all cases, the electron temperature is given by $T_e = 2$ keV. The yellow-shaded region indicates scale lengths characteristic of OMEGA experiments, while the blue-shaded region indicates scale lengths for ignition-scale designs.

the expected growth rate [Eq. (1)] and can be simply generalized to the case of multiple EM plane-wave irradiation.[22,24] A similar analysis can be performed including a linear variation in density δN. This results in the same two coupled differential equations (in wave-number space) that have been shown by Simon *et al*. to lead to the approximate threshold condition of Eq. (9) [e.g., Eqs. (3) and (4) in Simon *et al*.[6]].

Equation (4) can be used to compute the properties of linear stability with the combined effect of a density gradient and LW collisional damping, which are described by the terms δN and ν_e in Eq. (4), respectively, together with the effects of multibeam irradiation through the boundary conditions applied to Eq. (3). Figure 134.35 shows the numerically determined absolute threshold containing both LW dissipation and plasma inhomogeneity by solving Eq. (4) for two overlapped plane EM waves (see Fig. 134.36). A more-complete stability analysis must take into account the geometry and polarization of laser irradiation for a given experiment[24]—a three-dimensional

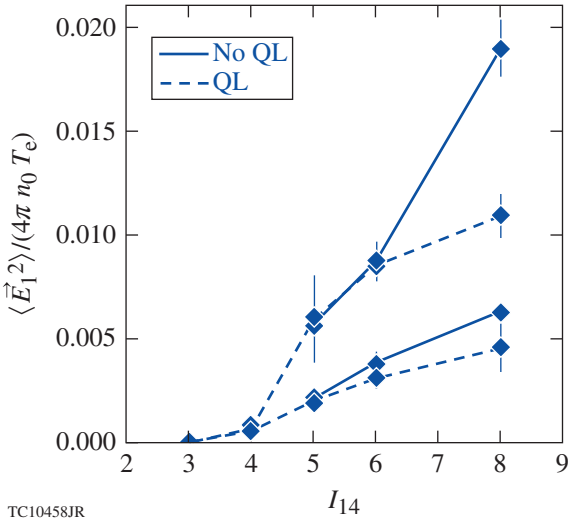

Figure 134.36
The electrostatic field intensity $\langle | \vec{E}_1 |^2 \rangle / (4\pi n_0 T_e)$ at nonlinear saturation as a function of laser intensity for a plasma with $Z_{eff} = 14$, $L_n = 330\ \mu$m, and $T_e = 2$ keV. The dashed (solid) curves show the results with (without) quasi-linear (QL) evolution of the electron-distribution function. The upper and lower sets of two curves correspond to strong $(\tilde{\nu}_i = 0.1)$ and weak $(\tilde{\nu}_i = 0.02)$ IAW damping, respectively. The error bars indicate the root-mean-square (rms) deviation from the average value at saturation.

problem. Currently, this is being investigated using a new code (*ZAK3D*) that solves Eqs. (4) and (5) in three dimensions.[75,76]

For ignition-class lasers with ~1 MJ of laser energy [e.g., the National Ignition Facility (NIF)[77]], the TPD threshold in direct-drive designs[37] is exceeded by a wider margin than in experiments on OMEGA/OMEGA EP, not because of a significant increase in laser intensity but because of the 2× to 3× increase in density scale length. As can be seen in Fig. 134.35, the inhomogeneity threshold is decreased by roughly a factor of 2 to 3. For such scale lengths, the collisional threshold can be made comparable to the inhomogeneity threshold by increasing the effective ionization state $Z_{eff} \equiv \langle Z^2 \rangle / \langle Z \rangle$ of the ablator material to $Z_{eff} \sim 14$ (e.g., silicon) (for multiple ion-species plasmas, the effective electron–ion collision frequency is obtained by replacing $Z \longrightarrow Z_{eff}$ in the usual expression for ν_{ei}). From the point of stability with respect to TPD, Fig. 134.35 suggests that increasing the Z_{eff} of the ablator is beneficial (for a fixed electron temperature), particularly if TPD is marginally unstable in CH, since satisfactory mid-Z ablators can be designed.[35,36]

All calculations presented in **Nonlinear Saturation** (p. 118) have assumed that the electromagnetic pump consisted of two plane EM waves incident at angles of ±23° with respect to the direction of the density gradient (see Fig. 134.37). The plasma parameters were chosen to be those of recent long-scale-length experiments in CH targets.[16,65] When Z_{eff} was varied, these hydrodynamic parameters were not changed: the electron temperature was $T_e = 2$ keV with $T_i = 1.5$ keV for ions. The density scale length was $L_n = 330\ \mu$m with the simulation box length L_x set to include densities from 0.19 n_c to 0.27 n_c, i.e. $L_x = (8/23)\, L_n$. [A separate analysis based on radiation–hydrodynamic simulations has been used to calculate the dependence of plasma parameters (e.g., density scale length and electron temperature) at the quarter-critical surface for different ablator materials with similar irradiation conditions[34] but this will not be discussed here.] When simulating a multiple-ion-species plasma, Eq. (5) was used to simulate an "effective" IAW such that Z and m_i were replaced by their averages (over ion species) except in the collisional LW damping rate as mentioned previously. Values of $Z_{eff} = 5.3$, 10, and 14 were obtained by modeling CH, SiO_2, and Si plasmas, respectively. The IAW damping rate ν_i is currently a fixed parameter that is initialized at the start of the calculation. This was equated with the expected Landau-damping rate of the least-damped IAW mode[78,79] for CH, SiO_2, and Si, except for the $Z_{eff} = 10$ and 14 strong damping cases, where $\tilde{\nu}_i$ was set to $\tilde{\nu}_i = 0.1$, where $\tilde{\nu}_i \equiv \nu_i / \omega_s$ is the dimensionless IAW damping rate and $\omega_s \simeq k c_s$ is the IAW frequency.

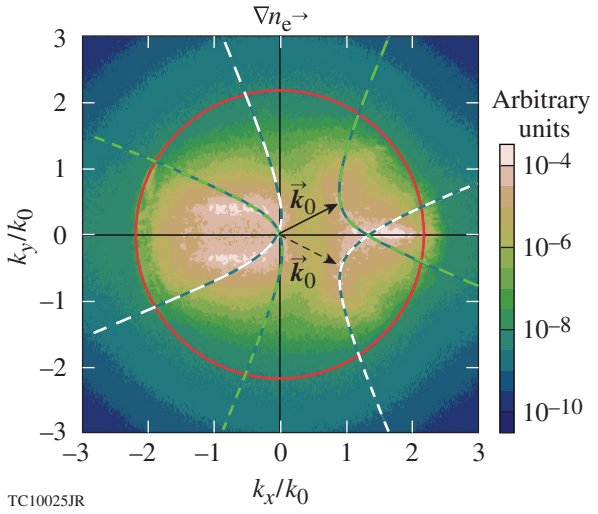

Figure 134.37
The time-averaged electrostatic field spectrum $\langle | \vec{E}_1(\vec{k}) |^2 \rangle_\tau$ (in arbitrary units) taken from a representative run at a time when nonlinear saturation has been attained. The instability is driven by two plane EM waves (black arrows) that are incident at an angle of ±23° with respect to the direction of the density gradient (x direction) and are polarized in the simulation (x,y) plane. The green (white) curves show the location of the maximum in growth rate as calculated by homogeneous theory [Eq. (1)]. The red circle indicates the location of the Landau cutoff $(| \vec{k} | \lambda_{De} = 0.25)$.

For non-negligible LW amplitudes, the *QZAK* model includes nonlinear coupling to ion fluctuations δn, which introduces a rich variety of nonlinear and turbulent phenomena. It also includes quasi-linear (kinetic) effects. Together, these effects will determine the long-time behavior of TPD relevant to experiment and the relative importance between absolute modes and convective modes in the nonlinear state.

Nonlinear Saturation

1. Anomalous Absorption
   (Heating of Near-Thermal Electrons)

Several diagnostics have been implemented to quantify the level of two-plasmon–decay instability and its dependence on plasma composition. Figure 134.37 shows the spatially averaged Langmuir-wave intensity $\left\langle \left| \vec{E}_1 \right|^2 \right\rangle \Big/ 4\pi n_0 T_e$ as a function of laser intensity for $Z_{eff} = 14$ at late time, when $\left\langle \left| \vec{E}_1 \right|^2 \right\rangle$ is judged to be steady. In all cases, spatial averaging is carried out over the whole simulation box that spans initial densities from 0.19 n_c to 0.27 n_c. It is convenient to define the energy (per unit length in the ignorable coordinate z) associated with electrostatic

$$W_1(t) \equiv \int \mathrm{d}x\mathrm{d}y \left| \vec{E}_1(x,y,t) \right|^2 \Big/ (4\pi)$$

and electromagnetic waves

$$W_2(t) \equiv \int \mathrm{d}x\mathrm{d}y \left| \vec{E}_2(x,y,t) \right|^2 \Big/ (8\pi)$$

[which are simply related to the above spatial averages

$$W_1 = A\left\langle \left| \vec{E}_1 \right|^2 \right\rangle \Big/ (4\pi),\ W_2 = A\left\langle \left| \vec{E}_2 \right|^2 \right\rangle \Big/ (8\pi),$$

where $A = L_x \times L_y$ is the area of the simulation box]. The effect of the quasi-linear evolution of the distribution function can be seen by comparing the saturated level of $\left\langle \left| \vec{E}_1 \right|^2 \right\rangle \Big/ 4\pi n_0 T_e$ with and without evolution of Eq. (6) for the spatially averaged electron-distribution function. Previously in Myatt *et al.*,[26] estimates of electron heating by TPD were based on the *ZAK* model using test particles; Fig. 134.37 demonstrates the importance of self-consistently evolving the electron-distribution function. The results are broadly consistent with those anticipated.[26] Figure 134.38 shows a contour plot of the self-consistently evolved electron-distribution function, where significant deviation from the initial Maxwellian distribution is evident.

Figure 134.39 illustrates the dependence of $\left\langle \left| \vec{E}_1 \right|^2 \right\rangle \Big/ 4\pi n_0 T_e$ (or equivalently W_1) on laser intensity for three values of Z_{eff} (5.3, 10, and 14) and for weak $\left(\tilde{\nu}_i = 0.02\right)$ and strong $\left(\tilde{\nu}_i = 0.1\right)$ ion-acoustic damping. It is evident that for a given ion-acoustic damping rate, the case of $Z_{eff} = 14$ has the lowest value of W_1. Regardless of the value of Z_{eff}, W_1 is smaller if ion-acoustic waves are weakly damped. The saturated value of W_1 can be connected to enhanced absorption of laser energy in the quarter-critical region in the following way: it can be shown

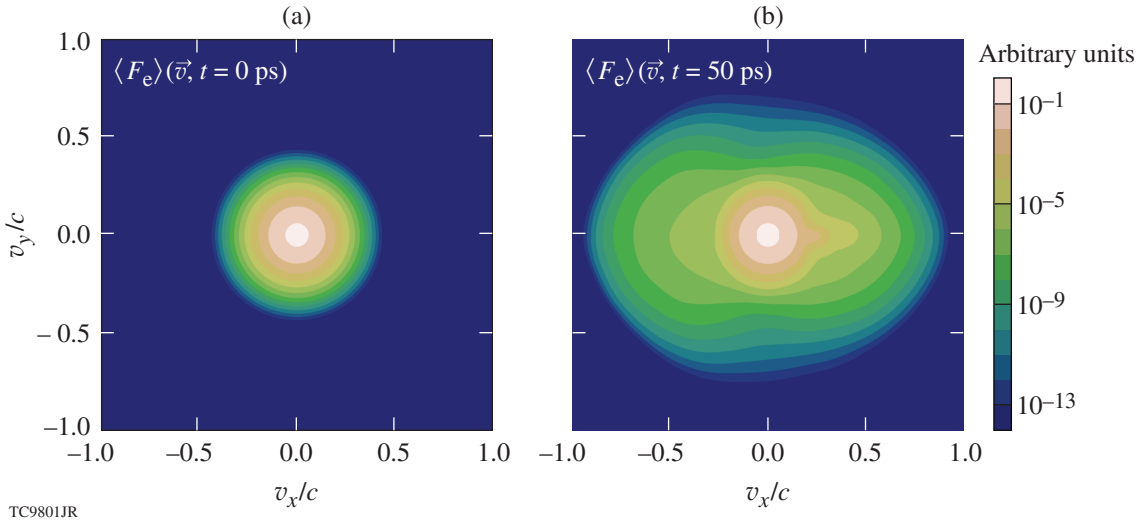

Figure 134.38
The electron distribution function $\left\langle F_e \right\rangle (\vec{v}, t = 0)$ is shown in velocity space at (a) $t = 0$ ps and (b) at a later time ($t = 50$ ps) after evolving according to the self-consistent quasi-linear diffusion equation [Eq. (6)].

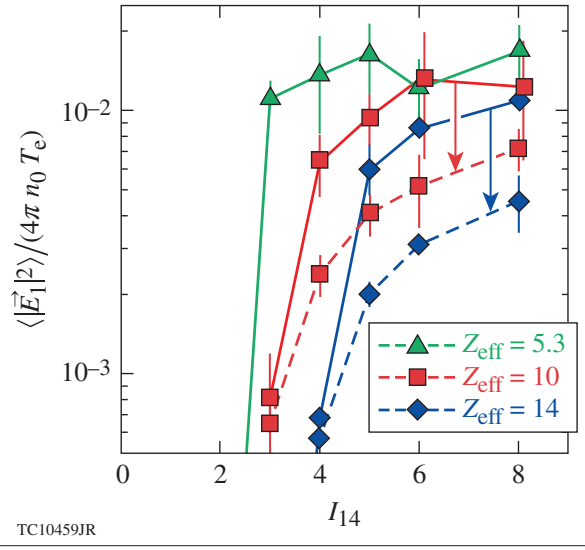

Figure 134.39
The electrostatic field intensity $\langle|\vec{E}_1|^2\rangle/(4\pi n_0 T_e)$ at nonlinear saturation as a function of total laser intensity for values of Z_{eff} = 5.3 (green), 10 (red), and 14 (blue), and for weak $(\tilde{\nu}_1 = 0.02)$ (dashed) and strong $(\tilde{\nu}_1 = 0.1)$ ion-acoustic wave (IAW) damping (solid curves). The error bars give the rms deviation from the mean values. The deviation can become quite significant for the most strongly driven cases.

that the field equations [Eqs. (3)–(5)] satisfy the energy conservation law

$$\partial_t\left[W_1 + W_2\right] = -2\sum_k\left[\nu_{coll} + \gamma_L(\vec{k})\right]\frac{\left|\vec{E}_1(\vec{k})\right|^2}{4\pi} - 2\nu_{2,T}W_2 - \int d\vec{s}\cdot\vec{\mathcal{P}}_2, \tag{10}$$

where $\vec{\mathcal{P}}_2$ is the Poynting vector

$$\vec{\mathcal{P}}_2 = \left(c^2/4\omega_p\right) i\left[\vec{E}_2^{\,*}\cdot\nabla\vec{E}_2 - \vec{E}_2\cdot\nabla\vec{E}_2^{\,*}\right]$$

and recalling that $\nu_{2,T} \approx \left(n_0/n_c\right)\nu_{ei}/2$ is the damping rate of the driving EM waves and $\nu_{coll} \approx \nu_{ei}/2$. Note that the dissipation associated with ion-acoustic waves does not enter in Eq. (10) because of the smallness of the mass ratio. In statistical steady state, defined by $\langle\partial_t[W_1 + W_2]\rangle_\tau = 0$, where $\langle\,\rangle_\tau$ implies a running time average,

$$-\left\langle\int d\vec{s}\cdot\vec{\mathcal{P}}_2\right\rangle_\tau = \frac{\nu_{ei}}{4}\left[1 + 4\frac{\langle W_1\rangle_\tau}{\langle W_2\rangle_\tau}\right]\langle W_2\rangle_\tau + 2\sum_k\left\langle\gamma_L(\vec{k})\frac{\left|\vec{E}_1(\vec{k})\right|^2}{4\pi}\right\rangle_\tau, \tag{11}$$

which, if $\gamma_L(\vec{k})$ is positive definite, gives the lower bound for the amount of power dissipated in the quarter-critical region, caused by electron–ion collisions, by the incident electromagnetic waves:

$$-\left\langle\int d\vec{s}\cdot\vec{\mathcal{P}}_2\right\rangle_\tau \gtrsim \frac{\nu_{ei}}{4}\left[1 + 4\frac{\langle W_1\rangle_\tau}{\langle W_2\rangle_\tau}\right]\langle W_2\rangle_\tau. \tag{12}$$

The term in the square brackets in Eq. (12) is a factor that multiplies the usual collisional energy absorption rate. This factor represents the anomalous (anom) enhancement of laser energy absorption caused by TPD $\eta_{anom} \equiv 1 + 4\langle W_1\rangle_\tau/\langle W_2\rangle_\tau$ (the assumption being that absorption is caused by electron–ion collisions and does not involve suprathermal electrons). A value of η_{anom} = 1 would give the usual amount of power dissipated that is associated with collisional absorption of light waves and corresponds to the usual terms present in ICF direct-drive hydrodynamic design codes. This can be estimated, for small absorption, as $(I_0 - I)/I_0 \approx \left(\nu_{ei}/4\right)\left(L_x/c\right) \sim 0.24$ (for CH). Figure 134.40 shows Fig. 134.39 replotted to illustrate the dependence of η_{anom} on laser intensity for materials of different ionization Z_{eff} and IAW damping rate. These results could be used to modify hydrocode predictions in a simple way by introducing a multiplier (η_{anom}) on the usual inverse bremsstrahlung term.

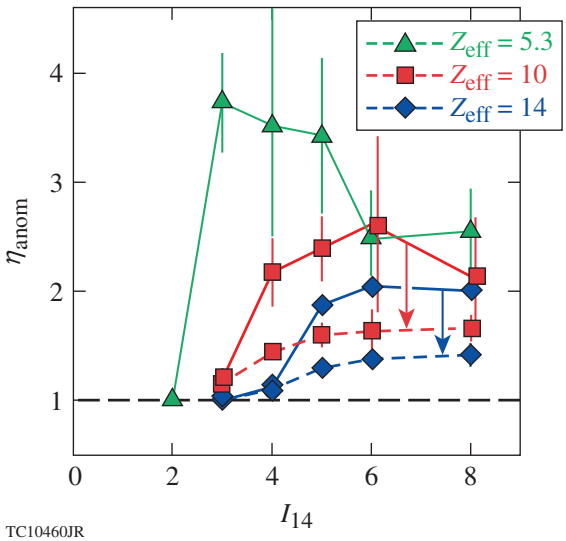

Figure 134.40
The anomalous absorption factor η_{anom} [see Eq. (12)] computed as a function of total laser intensity for values of Z_{eff} = 5.3 (green), 10 (red), and 14 (blue), for weak $(\tilde{\nu}_1 = 0.02)$ (dashed) and strong $(\tilde{\nu}_1 = 0.1)$ IAW damping (solid curves). The error bars show the rms deviation from the mean value computed at nonlinear saturation.

Figure 134.41 shows the dissipation spectrum

$$\left\langle \gamma_{\mathrm{L}}(\vec{k}) \left| \vec{E}_1(\vec{k}) \right|^2 \Big/ (4\pi) \right\rangle_{\tau}$$

that is associated with suprathermal electron production, i.e., the last term on the right-hand side of Eq. (11). It can be seen that features similar to the linearly unstable LW's exist, but dissipation extends to the Landau cutoff. Comparison of the size of the two terms on the right-hand side of Eq. (11) shows that the first (collisional term) is generally larger than the second, and that pump depletion is important for the more strongly driven runs presented here. It also suggests that the reference electron temperature T_{e} should be evolved. A future improvement of the code will be to evolve Eq. (3) self-consistently including pump depletion and collisional absorption. Evolution of the reference electron temperature T_{e} will also be considered.

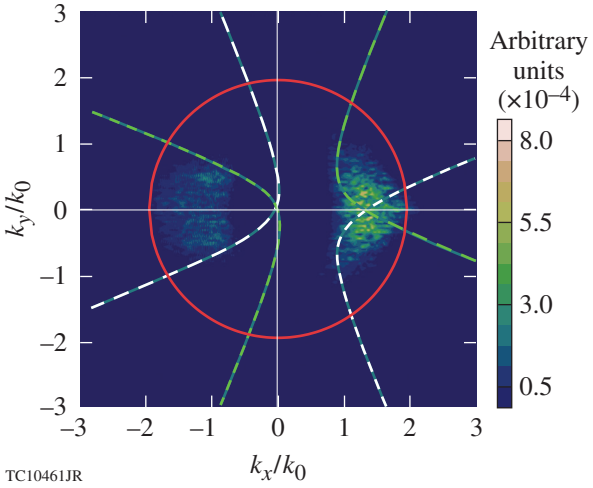

Figure 134.41
A snapshot of the dissipation spectrum $\gamma_{\mathrm{L}}(\vec{k}) \left| \vec{E}_1(\vec{k}) \right| / (4\pi)$ (in arbitrary units) that is associated with hot-electron generation and whose sum determines the power dissipated by collisionless processes [Eq. (11)]. As in Fig. 134.36, the green (white) curves show the spectral location of the maximum in TPD growth rate as calculated by homogeneous theory for each beam [Eq. (1)] and the red circle indicates the location of the Landau cutoff $\left(\left| \vec{k} \right| \lambda_{\mathrm{De}} = 0.25 \right)$.

2. The Production of Energetic Electrons

Velocity moments can be taken of Eq. (6) in the usual way to obtain evolution equations for the hydrodynamic variables. For example, an energy equation can be derived from Eqs. (6) and (7) for the spatially averaged electron-distribution function $\langle F_{\mathrm{e}} \rangle$ (by multiplying by $m_{\mathrm{e}} v^2/2$ and integrating over velocities) with the result

$$\partial_t W_{\mathrm{e}} + A \sum_{i=1}^{2} \frac{s_i}{L_i} \Delta Q_i = \sum_k \gamma_k \frac{\left| \vec{E}(\vec{k}) \right|^2}{16\pi} + \int \mathrm{d}\vec{v} \, \frac{1}{2} m v^2 \hat{\sigma}_{\mathrm{IB}} \left[\left\langle F_{\mathrm{e}} \right\rangle, \left| \vec{E}_1 \right|^2 \right] + \int \mathrm{d}\vec{v} \, \frac{1}{2} m v^2 \hat{\sigma}_{\mathrm{IB}} \left[\left\langle F_{\mathrm{e}} \right\rangle, \left| \vec{E}_{2,T} \right|^2 \right], \qquad (13)$$

where $W_{\mathrm{e}} = \left(m_{\mathrm{e}} / 2 \right) \int \mathrm{d}\vec{v} v^2 \left\langle F_{\mathrm{e}} \right\rangle$ is the total electron kinetic energy. The terms on the right-hand side of Eq. (13) can be identified as the dissipated power associated with the production of suprathermal electrons, the collisional absorption of Langmuir waves, and collisional absorption of the pumping laser (which is usually the only term included in radiation–hydrodynamic calculations). A statistical steady state can exist if these source terms balance the flux through the boundaries, where $\Delta Q_i \equiv \Delta Q_i^{>} - \Delta Q_i^{<} = \left(q_i^{>} - q_{i,0}^{>} \right) - \left(q_i^{<} - q_{i,0}^{<} \right)$ and the subscript i denotes each of the coordinate directions. The heat flux has its usual definition $\vec{q} \equiv \left(m_{\mathrm{e}} / 2 \right) \int_0^{\infty} \mathrm{d}\vec{v} \vec{v} v^2 \left\langle F_{\mathrm{e}} \right\rangle$ with the exception that the integral is split into two parts $q_i = q_i^{<} + q_i^{>}$, depending on the sign of the velocity component v_i [i.e., each piece corresponds to either forward-going (>) or backward-going (<) velocities with respect to the i direction]. The subscript "0" implies that it is calculated with the initial electron-distribution function $\langle F_{\mathrm{e}} \rangle (t = 0)$. For a symmetric (e.g., Maxwellian) initial distribution, $\vec{q}_0^{\,>} = -\vec{q}_0^{\,<}$ and the net heat flux vanishes.[80]

Together with Eq. (10), global energy conservation may be expressed as

$$\partial_t \left[W_1 + W_2 + W_{\mathrm{e}} \right] = -A \sum_{i=1}^{2} \frac{s_i}{L_i} \Delta Q_i - \int \mathrm{d}\vec{s} \cdot \vec{\mathcal{P}}_2 \qquad (14)$$

provided that

$$\int \mathrm{d}\vec{v} (1/2) m v^2 \hat{\sigma}_{\mathrm{IB}} \left[\left\langle F_{\mathrm{e}} \right\rangle, \left| \vec{E}_1 \right|^2 \right]$$

can be reduced to $\nu_{\mathrm{ei}} \langle W_1 \rangle$ and

$$\int \mathrm{d}\vec{v} (1/2) m v^2 \hat{\sigma}_{\mathrm{IB}} \left[\left\langle F_{\mathrm{e}} \right\rangle, \left| \vec{E}_{2,T} \right|^2 \right]$$

to $2\nu_{2,T} \langle W_2 \rangle \sim \nu_{\mathrm{ei}} \langle W_{2,T} \rangle / 4$. Therefore, in statistical steady state

$$-\frac{1}{A} \left\langle \int \mathrm{d}\vec{s} \cdot \vec{\mathcal{P}}_2 \right\rangle_{\tau} = \sum_{i=1}^{2} \frac{s_i}{L_i} \left\langle \Delta Q_i \right\rangle_{\tau}, \qquad (15)$$

and the absorbed power of the laser is balanced by the power flowing through the boundaries carried by the kinetic energy of electrons. For the case where the velocity space diffusion is assumed periodic in the i direction (which is the y direction transverse to the density gradient in all the calculations presented here), the corresponding flux term $\Delta Q_i / L_i$ is absent. Consequently, for doubly periodic boundaries, the only steady-state solution is the trivial one $\left\langle \int d\vec{s} \cdot \vec{\mathcal{P}}_2 \right\rangle_\tau = 0$. When one boundary is open (e.g., in the direction of the gradient), it corresponds to the use of "thermalizing" boundaries as is often implemented in PIC codes. The applicability of these boundary conditions has been discussed in Myatt *et al.*,[26] where the possibility of the reheating of electrons that pass multiple times through the quarter-critical region was evaluated.

Figure 134.42 shows the hot-electron power fraction $f_h^{>30}$ as a function of time for two runs that correspond to overlapped laser intensities of $I_L = 6 \times 10^{14}$ W/cm^2 and an effective ionization of $Z_{eff} = 10$ for two values of the ion-acoustic damping rate ($\tilde{\nu}_i = 0.1$ and 0.02). The fraction $f_h^{>30}(t)$ is defined as the ratio of the heat flux ΔQ_x to the (constant) laser intensity I_L (in W/cm^2) with the restriction that the limits on the range of integration in the integral determining the heat flux ΔQ_x are adjusted to include only electrons having energies greater than 30 keV (for this reason, the superscript). Experimentally, the fraction $f_{h,exp} \equiv E_h / E_L$ is a time-integrated measurement often determined (for a laser pulse of energy E_L) by inferring the energy E_h of suprathermal electrons via the strength of K_α emission from a fluorescent layer buried in the target.[16] A model of electron–photon transport in matter is used to relate the observed energy in K_α emission to the energy of hot electrons. For example, a molybdenum layer was used in Yaakobi *et al.*[16] having $E_{K_\alpha} \approx 17.5$ keV [which justifies our cutoff energy of 30 keV in the definition of $f_h^{>30}(t)$]. To facilitate a comparison with experiment, we define a running time average $\langle f_h^{>30} \rangle_\tau$. It can be seen from Fig. 134.42 that it is often possible to define a meaningful steady state so that $\langle f_h^{>30} \rangle_\tau$ is constant (and can be crudely equated with the experimental energy fraction $\langle f_h^{>30} \rangle_\tau \sim f_{h,exp}$). This steady-state time average (for $\tau > 35$ ps) is plotted in Fig. 134.43 for materials of varying Z_{eff} and $\tilde{\nu}_i$.

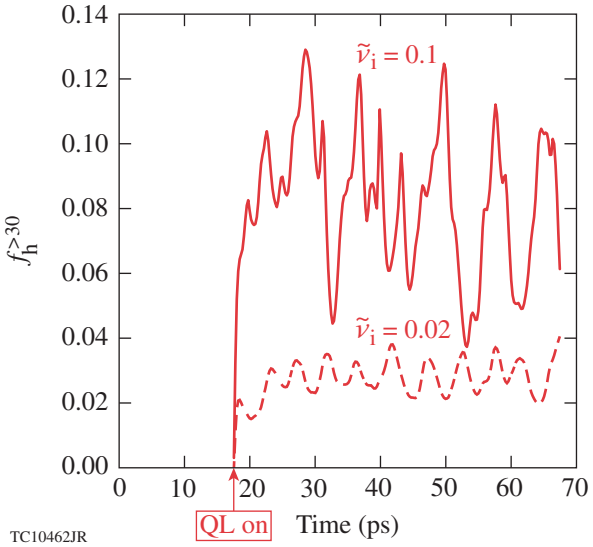

Figure 134.42
The heat flux carried by hot electrons with energies greater than 30 keV as a fraction of the incident laser power as a function of time $\left[f_h^{>30}(t)\right]$. These results were obtained for a plasma with $Z_{eff} = 10$ and a total laser intensity of 5×10^{14} W/cm^2. The solid curve corresponds to an ion-acoustic damping rate of $\tilde{\nu}_i = 0.1$, while the dashed curve corresponds to $\tilde{\nu}_i = 0.02$. In both cases, the runs commence at $t = 0$ but quasi-linear diffusion is not started until approximately $t = 17$ ps (as indicated by the arrow).

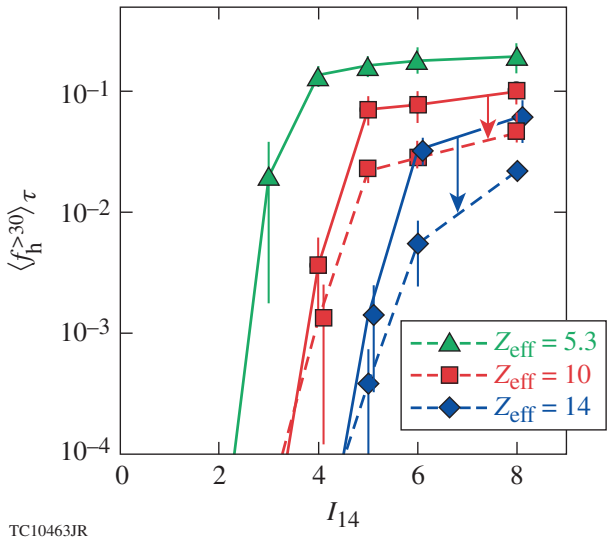

Figure 134.43
Hot-electron fraction $\langle f_h^{>30} \rangle_\tau$, as determined at nonlinear saturation as a function of total laser intensity for $Z_{eff} = 5.3$ (green curve), 10 (red curve), and 14 (blue curve). The solid curves indicate runs with an IAW damping rate of $\tilde{\nu}_i = 0.1$, while the dashed curves correspond to $\tilde{\nu}_i = 0.02$. The error bars quantify the rms fluctuations about the average that is associated with the steady state.

Figure 134.43 shows the main results of this study. It can be seen that the hot-electron fraction $\langle f_h^{>30} \rangle_\tau$ increases rapidly for $I_L \gtrsim 3$ to 5×10^{14} W/cm^2 (with a threshold depending on Z_{eff}) and then saturates at the level of several percent for CH targets, which is broadly consistent with PIC calculations[27,68] when electron–ion collisions are accounted for (in the RPIC calculations of Vu *et al.*,[27] grid damping plays the role of elec-

tron–ion collisions), and also experimental measurements[65] (the density scale length, electron temperature, and laser intensities were motivated by OMEGA EP experimental conditions using CH targets[65]). Calculations of SiO_2 targets, having weak ion-acoustic wave damping $\left(\tilde{\nu}_i = 0.02\right)$, show a similar intensity dependence but saturate at a level approximately half that of CH targets, while calculations of Si targets ($Z_{\text{eff}} = 14$, $\tilde{\nu}_i = 0.02$ had the lowest hot-electron fraction of all, which is particularly pronounced at mid-intensities ($I_L \sim 5 \times 10^{14}$ W/cm^2). In part, this is due to the effect of the increased threshold for Si associated with the Langmuir-wave damping (see Fig. 134.35).

In general, the lowest hot-electron production was seen for materials with the highest Z_{eff} and the smallest ion-acoustic wave damping $\tilde{\nu}_i = 0.02$. This suggests CH ablators might not be the best choice of ablator material from the point of view of TPD.

3. Confirmation of the Sensitivity to Ion-Acoustic Damping Using RPIC Calculations

Two 2-D RPIC simulations that do not make the quasi-linear approximation or any assumption regarding the spatial uniformity of the electron distribution function were performed to independently investigate the effect of the IAW damping rate on the development and saturation of TPD.

Over 50 *QZAK* calculations were performed in the current analysis, most for a long density scale length (L_n = 330 μm) and integrated out to times close to ~0.1 ns (~5 ns in combined total). Because RPIC calculations are much more computationally intensive than *QZAK*, the RPIC calculations were performed at a shorter scale length (L_n = 130 μm) and integrated for shorter times (t = 9 ps). The ion-acoustic damping rate was modified by varying the ion Landau-damping contribution to $\tilde{\nu}_i$ through the ion temperature [a hydrogen (Z = 1) plasma was assumed]. All other physical parameters were the same as described earlier for the *QZAK* calculations.

The two RPIC simulations used identical simulation domains consisting of 4096 (x direction) × 1024 (y direction) computational cells, and the electron and proton distributions were each represented by 32 particles/computational cell. The boundary conditions were compatible with those assumed by *QZAK* [see **Numerical Simulation of TPD Growth and Saturation in Inhomogeneous Collisional Plasma** (p. 113) and **The Production of Energetic Electrons** (p. 120)]: the particles were recycled periodically in the y direction and absorbed at the surfaces $x = 0$ (laser entrance boundary) and $x = L_x$ (laser exit boundary). At these boundaries, Maxwellian baths of electrons with temperature T_e and ions with temperature T_i were assumed, and the particles absorbed at these surfaces were replenished accordingly. Each of the two incident pump plane EM waves was given an intensity of $I_0 = 1 \times 10^{15}$ W/cm^2 with polarization in the x–y plane.

The so-called "low" and "high" IAW damping simulations correspond to $T_i = 0.1$ keV $\left(T_e/T_i = 20 \text{ and } \tilde{\nu}_i \approx 1.11 \times 10^{-3}\right)$ (electron Landau damping of IAW is not present in RPIC) and $T_i = 1$ keV $\left(T_e/T_i = 2 \text{ and } \tilde{\nu}_i \approx 2.70 \times 10^{-1}\right)$, respectively. The high-damping case has been presented elsewhere,[27,28] but the results are reproduced here for comparison. Figure 134.44 shows the suprathermal heat flux f_h ($\Delta Q_x^{>}$ normalized to the total laser intensity) as a function of time over a period of 10 ps for both cases. In the simulations, $\Delta Q_x^{>}$ is computed from the electron flux accumulated at the laser exit boundary ($x = L_x$) accounting for electrons of all energies. As before [**The Production of Energetic Electrons** (p. 120)], $\Delta Q_x^{>}$ represents the electron heat flux in excess of its initial (Maxwellian) value.

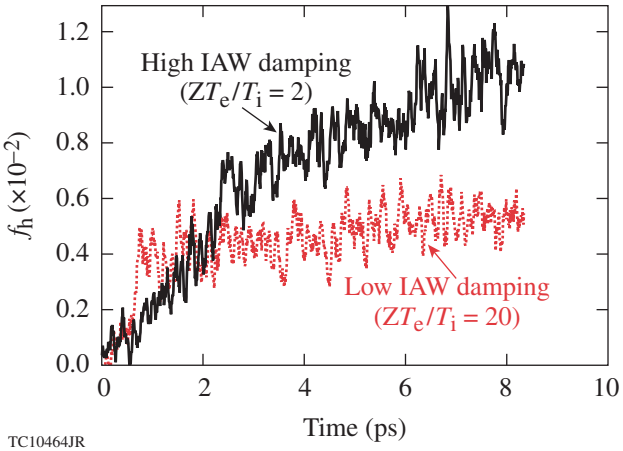

Figure 134.44
The suprathermal heat flux f_h, as computed by the code RPIC,[27] is shown as a function of time for cases of high $\left(\tilde{\nu}_i \approx 2.70 \times 10^{-1}\right)$ and low $\left(\tilde{\nu}_i \approx 1.11 \times 10^{-3}\right)$ IAW damping. While the low-damping case reaches saturation much more quickly, its saturation level is lower.

Figure 134.44 indicates that both the high-damping and low-damping cases reached saturation, and that the high-damping case achieved a suprathermal heat flux $\Delta Q_x^{>}$ about twice as large as that of the low-damping case. Furthermore, while the high-damping case took several (~10) picoseconds to reach saturation, the low-damping case achieved saturation in about

0.5 ps. The comparison shown in Fig. 134.44 presents supporting evidence that the IAW damping rate has an important effect on the temporal development and saturation level of TPD.

The RPIC simulation corresponding to high $\tilde{\nu}_i$ and shown in Fig. 134.44 has been previously analyzed in some detail.[27,28] The nonlinear state was described in terms of cavitating LW turbulence, and it was determined that prerequisites for the quasi-linear description were met—i.e., the distribution function was well described by its spatial average and trapping effects were negligible.[28] A comparison between RPIC and *QZAK* is given in Vu *et al.*,[81] but we speculate here on the importance of the ion-acoustic damping rate in the context of cavitating LW turbulence.

4. Dependence of $\langle f_h \rangle$ on the IAW Damping Rate and Nucleation Dynamics

The significant sensitivity of the saturated level of TPD excitation on the IAW damping rate is clearly a nonlinear effect since the linear theory does not involve IAW's. Such sensitivity might be anticipated since it has been observed in previous *ZAK* model studies of SRS in the weak Landau-damping regime.[29] Previous work[30–32] has also demonstrated that nucleation of cavitons is favored by strong IAW damping. The detailed manifestation of this for the simulation regime considered here is under study. A qualitative summary of our current view is based on the assumption that Langmuir cavitation and collapse are the dominant processes in the nonlinear stage of TPD for the parameters considered.[28]

In the cavitating turbulence scenario, the level of electrostatic fluctuations is governed by the nucleation–collapse–burnout cycle[82,83] and the time scale of this process is governed by the IAW damping rate.[27] The interference pattern of the linearly excited triad of free plane LW's (see Fig. 134.36) produces density trenches that are modulated longitudinally by the beating of the forward common LW with the backward pair of triad waves. The ponderomotive force from the peaks in $\left|\vec{E}_1\right|^2$ resulting from this modulation produces density depressions that can support localized (or bound) states of the Langmuir field. The backward triad waves have long wavelengths and frequencies near the local electron plasma frequency and can directly nucleate the bound state.[82,83] These localized states then proceed to collapse and burn out, producing a large enhancement of LW energy and electron flux. As the triad modes evolve to higher k values,[28] the spatial scale of the longitudinal modulation appears to produce much stronger, smaller-scale density cavities in the trenches. These residual cavities appear to be too narrow and deep to efficiently nucleate new cavitons. The Langmuir turbulence then dies out locally until the short-scale density fluctuations dissipate by IAW Landau damping. The nucleation process can then resume with another burst of Langmuir turbulence once this has occurred.

In the nucleation–collapse–burnout cycle,[82,83] a source must be present that can excite the bound state. The nucleation source is essentially the overlap integral of the bound-state wave function and the source, which may be the TPD current on the right-hand side of Eq. (4). This source produces freely propagating LW's that are dominantly the triad modes discussed recently.[27,28] If this source has frequencies close enough to the bound-state eigenfrequency, it can cause a near-resonant excitation of the bound state and initiate a collapse. To have such frequencies, free LW's must have long wavelengths such that the bound-state wave function having the largest overlap integral with this long-wavelength source is the lowest or "ground state" with no nodes in its wave function. Our experience is that only this state is appreciably excited. A density well that is too deep may have a deeply bound ground-state wave function, which will not efficiently couple to a long-wavelength free LW. This means that for efficient nucleation, the density well should not be too deep, implying that the spatial width should be large enough to trap a weakly bound ground state. Strong IAW damping appears to produce more cavities of this type (because of this nucleation effect, the LDI cascade, where LW's decay into LW's with increasingly lower wavelengths, never progresses past a few steps before cavitons are nucleated in the ion-density fluctuations created by the LDI process itself).[29] For these TPD simulations, LDI appears to play a minor role, while the TPD triad[25] and the ion-density fluctuations arising from their beating play a similar role in the nucleation process.

It is very difficult to diagnose, in microscopic detail, a system with as many as 10^4 cavitons.[28] The scenario outlined above is consistent with our experience with simpler systems. Further microscopic details will be presented in a future publication.

Summary and Discussion

A two-dimensional model that further generalizes the extended Zakharov model of TPD to include quasi-linear diffusion of the electron distribution function has been described. The model addresses the nonlinear evolution of the TPD instability caused by the self-consistent coupling of TPD-generated LW's with ion-density fluctuations and quasi-linear evolution of the electron-distribution function. Quasi-linear evolution of

the electron-distribution function was shown to lead to saturation of the average LW intensity at lower values than predicted by the Zakharov model alone for parameters of interest to recent experiments.

In the linear regime of infinitesimal LW amplitude, the model allows for TPD stability to be determined in the presence of both density inhomogeneity and LW damping for a laser pump described in terms of multiple overlapping plane EM waves in two dimensions. A more-complete treatment requires the model to be solved in three dimensions. A 3-D code solving Eqs. (4) and (5) but omitting the quasi-linear diffusion terms is described in Zhang *et al*.[76] It was shown that collisional damping of LW's is important for directly driven ICF targets at the ignition scale. In the nonlinear stage of TPD it was shown that the energy absorbed by the target and converted into electron thermal energy by the collisional absorption of TPD LW's is comparable to, or greater than, the energy converted into hot electrons. It was suggested that maximizing the collisional damping of LW's in direct-drive designs could be beneficial in mitigating TPD absorption and preheat.

For fixed electron temperature and density scale length, the lowest hot-electron production was seen for materials with the highest Z_{eff} and the smallest IAW damping rate. The reduction in hot-electron fraction can be partly explained by the increased threshold. The nonlinear effect associated with weakly damped ion-acoustic waves was independently investigated with RPIC calculation, and a possible physical explanation for this effect was given in terms of nucleation dynamics of cavitating Langmuir turbulence. An experimental test might be to compare TPD in two materials of similar Z_{eff}, e.g., Si- and Ge-doped plastic, where the second material has a greater IAW damping rate because of the presence of light (H) ions.

Future improvements to the *QZAK* model will include implementation of terms describing the effects of pump depletion and collisional absorption for the EM pump. Self-consistent evolution of the reference electron temperature will also be investigated. Work is also underway to implement the quasi-linear diffusion equation in three dimensions.

ACKNOWLEDGMENT

This work was supported by the U.S. Department of Energy Office of Inertial Confinement Fusion under Cooperative Agreement No. DE-FC52-08NA28302, the University of Rochester, and the New York State Energy Research and Development Authority. The support of DOE does not constitute an endorsement by DOE of the views expressed in this article.

REFERENCES

1. M. V. Goldman, Ann. Phys. **38**, 117 (1966).
2. M. N. Rosenbluth, Phys. Rev. Lett. **29**, 565 (1972).
3. Y. C. Lee and P. K. Kaw, Phys. Rev. Lett. **32**, 135 (1974).
4. V. P. Silin and A. N. Starodub, Sov. Phys.-JETP **39**, 82 (1974).
5. A. B. Langdon, B. F. Lasinski, and W. L. Kruer, Phys. Rev. Lett. **43**, 133 (1979).
6. A. Simon, R. W. Short, E. A. Williams, and T. Dewandre, Phys. Fluids **26**, 3107 (1983).
7. H. Derblom *et al*., J. Geophys. Res, A, Space Phys. **94**, 10111 (1989).
8. D. W. Phillion *et al*., Phys. Rev. Lett. **49**, 1405 (1982).
9. W. Seka, R. E. Bahr, R. W. Short, A. Simon, R. S. Craxton, D. S. Montgomery, and A. E. Rubenchik, Phys. Fluids B **4**, 2232 (1992).
10. S. P. Regan, N. B. Meezan, L. J. Suter, D. J. Strozzi, W. L. Kruer, D. Meeker, S. H. Glenzer, W. Seka, C. Stoeckl, V. Yu. Glebov, T. C. Sangster, D. D. Meyerhofer, R. L. McCrory, E. A. Williams, O. S. Jones, D. A. Callahan, M. D. Rosen, O. L. Landen, C. Sorce, and B. J. MacGowan, Phys. Plasmas **17**, 020703 (2010).
11. W. Seka, D. H. Edgell, J. F. Myatt, A. V. Maximov, R. W. Short, V. N. Goncharov, and H. A. Baldis, Phys. Plasmas **16**, 052701 (2009).
12. N. A. Ebrahim *et al*., Phys. Rev. Lett. **45**, 1179 (1980).
13. H. A. Baldis and C. J. Walsh, Phys. Rev. Lett. **47**, 1658 (1981).
14. D. M. Villeneuve, R. L. Keck, B. B. Afeyan, W. Seka, and E. A. Williams, Phys. Fluids **27**, 721 (1984).
15. C. Rousseaux *et al*., Phys. Fluids B **4**, 2589 (1992).
16. B. Yaakobi, P.-Y. Chang, A. A. Solodov, C. Stoeckl, D. H. Edgell, R. S. Craxton, S. X. Hu, J. F. Myatt, F. J. Marshall, W. Seka, and D. H. Froula, Phys. Plasmas **19**, 012704 (2012).
17. C. S. Liu and M. N. Rosenbluth, Phys. Fluids **19**, 967 (1976).
18. B. B. Afeyan and E. A. Williams, Phys. Rev. Lett. **75**, 4218 (1995).
19. E. Z. Gusakov, Sov. J. Plasma Phys. **8**, 324 (1982).
20. G. Laval, R. Pellat, and D. Pesme, Phys. Rev. Lett. **36**, 192 (1976).
21. C. Stoeckl, R. E. Bahr, B. Yaakobi, W. Seka, S. P. Regan, R. S. Craxton, J. A. Delettrez, R. W. Short, J. Myatt, A. V. Maximov, and H. Baldis, Phys. Rev. Lett. **90**, 235002 (2003).
22. D. F. DuBois, B. Bezzeridels, and H. A. Rose, Phys. Fluids B **4**, 241 (1992).
23. R. W. Short, Bull. Am. Phys. Soc. **53**, 245 (2008).

24. D. T. Michel, A. V. Maximov, R. W. Short, S. X. Hu, J. F. Myatt, W. Seka, A. A. Solodov, B. Yaakobi, and D. H. Froula, Phys. Rev. Lett. **109**, 155007 (2012).

25. H. X. Vu, D. F. DuBois, D. A. Russell, and J. F. Myatt, Phys. Plasmas **17**, 072701 (2010).

26. J. F. Myatt, J. Zhang, J. A. Delettrez, A. V. Maximov, R. W. Short, W. Seka, D. H. Edgell, D. F. DuBois, D. A. Russell, and H. X. Vu, Phys. Plasmas **19**, 022707 (2012).

27. H. X. Vu, D. F. DuBois, J. F. Myatt, and D. A. Russell, Phys. Plasmas **19**, 102703 (2012).

28. H. X. Vu, D. F. DuBois, D. A. Russell, and J. F. Myatt, Phys. Plasmas **19**, 102708 (2012).

29. D. A. Russell, D. F. DuBois, and H. A. Rose, Phys. Plasmas **6**, 1294 (1999).

30. D. F. DuBois *et al*., Phys. Fluids B **5**, 2616 (1993).

31. D. F. Dubois *et al*., J. Geophys. Res. **98**, 17543 (1993).

32. D. F. DuBois, D. A. Russell, and H. A. Rose, Phys. Rev. Lett. **74**, 3983 (1995).

33. V. A. Smalyuk, R. Betti, J. A. Delettrez, V. Yu. Glebov, D. D. Meyerhofer, P. B. Radha, S. P. Regan, T. C. Sangster, J. Sanz, W. Seka, C. Stoeckl, B. Yaakobi, J. A. Frenje, C. K. Li, R. D. Petrasso, and F. H. Séguin, Phys. Rev. Lett. **104**, 165002 (2010).

34. S. X. Hu, D. T. Michel, D. H. Edgell, D. H. Froula, R. K. Follett, V. N. Goncharov, J. F. Myatt, S. Skupsky, and B. Yaakobi, Phys. Plasmas **20**, 032704 (2013).

35. R. Betti, R. Nora, M. Lafon, J. F. Myatt, and K. S. Anderson, Bull. Am. Phys. Soc. **57**, 154 (2012).

36. M. Lafon, R. Nora, and R. Betti, Bull. Am. Phys. Soc. **57**, 153 (2012).

37. V. N. Goncharov, T. C. Sangster, T. R. Boehly, S. X. Hu, I. V. Igumenshchev, F. J. Marshall, R. L. McCrory, D. D. Meyerhofer, P. B. Radha, W. Seka, S. Skupsky, C. Stoeckl, D. T. Casey, J. A. Frenje, and R. D. Petrasso, Phys. Rev. Lett. **104**, 165001 (2010).

38. V. E. Zakharov, Sov. Phys.-JETP **35**, 908 (1972).

39. A. Hasegawa, Phys. Rev. A **1**, 1746 (1970).

40. R. C. Davidson, *Methods in Nonlinear Plasma Theory* (Academic Press, New York, 1972).

41. P. A. Robinson, Rev. Mod. Phys. **69**, 507 (1997).

42. M. V. Goldman, Rev. Mod. Phys. **56**, 709 (1984).

43. P. Y. Cheung and A. Y. Wong, Phys. Rev. Lett. **55**, 1880 (1985).

44. A. Y. Wong and P. Y. Cheung, Phys. Rev. Lett. **52**, 1222 (1984).

45. B. Eliasson and B. Thidé, J. Geophys. Res, A, Space Phys. **113**, A02313 (2008).

46. D. A. Russell and D. F. DuBois, Phys. Rev. Lett. **86**, 428 (2001).

47. J. Briand *et al*., Phys. Fluids B **2**, 160 (1990).

48. J. C. Weatherall, Astrophys. J. **506**, 341 (1998).

49. A. Hanssen *et al*., J. Geophys. Res, A, Space Phys. **97**, 12,073 (1992).

50. D. F. DuBois, H. A. Rose, and D. Russell, Phys. Rev. Lett. **66**, 1970 (1991).

51. D. F. DuBois and M. V. Goldman, Phys. Rev. **164**, 207 (1967).

52. A third-harmonic envelope could be used to describe $3/2\omega_0$ emission, as in Ref. 46.

53. A. N. Starodub and M. V. Filippov, Sov. J. Plasma Phys. **5**, 610 (1979).

54. V. Yu. Bychenkov, V. P. Silin, and V. T. Tikhonchuk, Sov. J. Plasma Phys. **3**, 730 (1977).

55. R. L. Berger and L. V. Powers, Phys. Fluids **28**, 2895 (1985).

56. W. Seka, B. B. Afeyan, R. Boni, L. M. Goldman, R. W. Short, K. Tanaka, and T. W. Johnston, Phys. Fluids **28**, 2570 (1985).

57. V. E. Zakharov, in *Handbook of Plasma Physics*, edited by M. N. Rosenbluth and R. Z. Sagdeev, Volume 2: Basic Plasma Physics II, edited by A. A. Galeev and R. N. Sudan (Elsevier Science Publishers B.V., Amsterdam, 1984), Chap. 5.3, pp. 81–121.

58. P. Mounaix *et al*., Phys. Fluids B **3**, 1392 (1991).

59. J. Dawson and C. Oberman, Phys. Fluids **5**, 517 (1962).

60. A series of runs were performed to investigate the sensitivity of the saturated state (described in terms of LW excitation level and hot-electron flux) to the LW noise level. No significant difference was found when varying the intensity of LW noise over two orders of magnitude.

61. K. Y. Sanbonmatsu *et al*., Phys. Plasmas **7**, 2824 (2000).

62. B. Fornberg, *A Practical Guide to Pseudospectral Methods*, Cambridge Monographs on Applied and Computational Mathematics, Vol. 1 (Cambridge University Press, Cambridge, England, 1998).

63. O. Skjaeraasen, P. A. Robinson, and D. L. Newman, Phys. Plasmas **18**, 022103 (2011).

64. D. Peaceman and H. H. Rachford, Jr., J. Soc. Indust. Appl. Math. **3**, 28 (1955).

65. D. H. Froula, B. Yaakobi, S. X. Hu, P.-Y. Chang, R. S. Craxton, D. H. Edgell, R. Follett, D. T. Michel, J. F. Myatt, W. Seka, R. W. Short, A. Solodov, and C. Stoeckl, Phys. Rev. Lett. **108**, 165003 (2012).

66. R. Yan, A. V. Maximov, C. Ren, and F. S. Tsung, Phys. Rev. Lett. **103**, 175002 (2009).

67. R. Yan, A. V. Maximov, and C. Ren, Phys. Plasmas **17**, 052701 (2010).

68. R. Yan, C. Ren, J. Li, A. V. Maximov, W. B. Mori, Z. M. Sheng, and F. S. Tsung, Phys. Rev. Lett. **108**, 175002 (2012).

69. C. S. Liu, in *Advances in Plasma Physics*, edited by A. Simon and W. B. Thompson (Wiley-Interscience, New York, 1976), Vol. 6, pp. 167–174.

70. B. F. Lasinski and A. B. Langdon, Lawrence Livermore National Laboratory, Livermore, CA, Report UCRL-50021-77, 4-49 (1978).

71. T. R. Boehly, D. L. Brown, R. S. Craxton, R. L. Keck, J. P. Knauer, J. H. Kelly, T. J. Kessler, S. A. Kumpan, S. J. Loucks, S. A. Letzring, F. J. Marshall, R. L. McCrory, S. F. B. Morse, W. Seka, J. M. Soures, and C. P. Verdon, Opt. Commun. **133**, 495 (1997).

72. L. J. Waxer, D. N. Maywar, J. H. Kelly, T. J. Kessler, B. E. Kruschwitz, S. J. Loucks, R. L. McCrory, D. D. Meyerhofer, S. F. B. Morse, C. Stoeckl, and J. D. Zuegel, Opt. Photonics News **16**, 30 (2005); D. N. Maywar, J. H. Kelly, L. J. Waxer, S. F. B. Morse, I. A. Begishev, J. Bromage, C. Dorrer, J. L. Edwards, L. Folnsbee, M. J. Guardalben, S. D. Jacobs, R. Jungquist, T. J. Kessler, R. W. Kidder, B. E. Kruschwitz, S. J. Loucks, J. R. Marciante, R. L. McCrory, D. D. Meyerhofer, A. V. Okishev, J. B. Oliver, G. Pien, J. Qiao, J. Puth, A. L. Rigatti, A. W. Schmid, M. J. Shoup III, C. Stoeckl, K. A. Thorp, and J. D. Zuegel, J. Phys., Conf. Ser. **112**, 032007 (2008).

73. M. V. Goldman, Ann. Phys. **38**, 95 (1966).

74. W. L. Kruer, in *The Physics of Laser Plasma Interactions*, Frontiers in Physics, Vol. 73, edited by D. Pines (Addison-Wesley, Redwood City, CA, 1988).

75. J. Zhang, J. F. Myatt, A. V. Maximov, R. W. Short, D. F. DuBois, D. A. Russell, and H. X. Vu, Bull. Am. Phys. Soc. **57**, 299 (2012).

76. J. Zhang, J. F. Myatt, R. W. Short, A. V. Maximov, H. X. Vu, D. F. DuBois, and D. A. Russell, "Multibeam Two-Plasmon Decay from Linear Threshold to Nonlinear Saturation," to be published in Physical Review Letters.

77. W. J. Hogan, E. I. Moses, B. E. Warner, M. S. Sorem, and J. M. Soures, Nucl. Fusion **41**, 567 (2001); E. I. Moses, Fusion Sci. Technol. **54**, 361 (2008).

78. H. X. Vu, J. M. Wallace, and B. Bezzerides, Phys. Plasmas **1**, 3542 (1994).

79. E. A. Williams, R. L. Berger, R. P. Drake, A. M. Rubenchik, B. S. Bauer, D. D. Meyerhofer, A. C. Gaeris, and T. W. Johnston, Phys. Plasmas **2**, 129 (1995).

80. The assumption that the reference distribution function is Maxwellian is not quite correct because there is expected to be a nonvanishing heat flux at the quarter-critical surface. Future work will take this into account, where it is speculated that heat-carrying electrons propagating down the density gradient may be able to couple more efficiently with TPD-generated Langmuir waves.

81. H. X. Vu, D. F. DuBois, D. A. Russell, and J. F. Myatt, Phys. Plasmas **19**, 102708 (2012).

82. G. D. Doolen, D. F. DuBois, and H. A. Rose, Phys. Rev. Lett. **54**, 804 (1985).

83. D. A. Russell, D. F. DuBois, and H. A. Rose, Phys. Rev. Lett. **60**, 581 (1988).

Hot-Electron Generation from Laser/Pre-Plasma Interactions in Cone-Guided Fast Ignition

Introduction

The cone-guided scheme for fast-ignition inertial confinement fusion (ICF)[1,2] provides the potential of higher gains at lower total driver energy than conventional central hot-spot–ignition schemes. In this scheme, a spherical target with a hollow gold cone attached is first compressed by laser beams outside the cone and then ignited by a petawatt (PW) short ignition pulse launched into the cone. The cone keeps the plasma out during the compression so that the ignition pulse can reach the cone tip and generate MeV electrons close to the assembled fuel core. Given the angular spread of laser-generated hot electrons, keeping the hot-electron source closer to the assembled core is important to the success of fast ignition. Early Gekko XII experiments with the cone-guided scheme showed good laser–core coupling.[2,3] Recent scaled-up integrated experiments on OMEGA/OMEGA EP showed, however, a lower coupling efficiency.[4]

One of the important factors affecting the laser–core coupling efficiency is the pre-plasma inside the cone.[5] The pre-plasma is generated by an ~1-mJ laser prepulse from amplified spontaneous emission in the PW ignition pulse. Previous experiments and simulations[5–7] have shown that the pre-plasma can significantly reduce the forward-going hot-electron flux. The interaction of the main ignition pulse with the pre-plasma depends on the duration of the ignition pulse, as indicated by recent particle-in-cell (PIC) simulations of laser channeling[8,9] for the channeling/hole-boring fast-ignition scheme. The duration of the short pulse in the early work was of the order of 1 ps (Refs. 5 and 7), and was shorter than the 10-ps pulse in the OMEGA experiment.[4] The required pulse duration for ignition, producing an electron beam with tens of kilojoules of energy,[10] would be 10 to 20 ps. PIC simulations with longer ignition-pulse durations can help answer questions such as whether a longer ignition pulse can essentially push away the pre-plasma to interact mostly with the cone tip.

Here we present recent PIC simulations using *OSIRIS*[11] to study hot-electron generation and their transport in plasma at densities up to 100 n_c, where $n_c = 1 \times 10^{21}$ cm^{-3} is the critical density of 1.053-μm laser light, as used in the cone-in-shell integrated fast-ignition experiments at the Omega Laser Facility.[4] The simulations are 2-D in space and 3-D in velocity. The pulse duration in the simulations was 6.7 ps, comparable to the 10-ps OMEGA EP pulse. To achieve these simulations, we used an artificial drag force[12] to slow down hot electrons after they leave the laser-interaction region. This prevented the hot electrons from accumulating near the simulation box boundaries and interrupting the simulations. Combined with particle thermal boundary conditions, this also reduced the effects of a finite box size on laser–plasma interactions. The simulations showed that the generated hot electrons were dominated in number by low-energy electrons but in energy by multi-MeV electrons. The hot electrons had a mean half-angle of 68°. Except for differences during the early stage of the pulse, *s*- and *p*-polarizations showed similar accumulated laser-absorption rates and hot-electron characteristics. The electron transport in the density region from 5 n_c to 100 n_c was ballistic, which may make it possible to use the current results for further transport study.

The following sections describe the simulation setup and results, which are then discussed and summarized.

Simulation Setup

The simulation setup is shown in Fig. 134.45(a). Three species of particles were used in the simulations: the electrons (Species 1) and ions (Species 2) initially inside the cone and the electrons initially outside the cone (Species 3). The "cone boundary" in this article refers to the $n_e = 100\ n_c$ surface. The cone boundary had a full opening angle of 34°. The ions outside the cone were treated as immobile. The plasma density profile inside the cone was obtained from linear interpolation of a hydrodynamics simulation using *HYDRA*,[13] in which the laser prepulse had an energy of ~22 mJ and a duration of 0.9 ns. The initial density scale length at n_c was ~20 μm. Densities above 100 n_c (outside the cone) were capped at 100 n_c; therefore, particle transport in plasmas above 100 n_c was not studied. The temperatures of all electrons and gold ions were set at 1 keV. The ionization state of the ions was fixed at 20, estimated based on the *HYDRA* simulation.

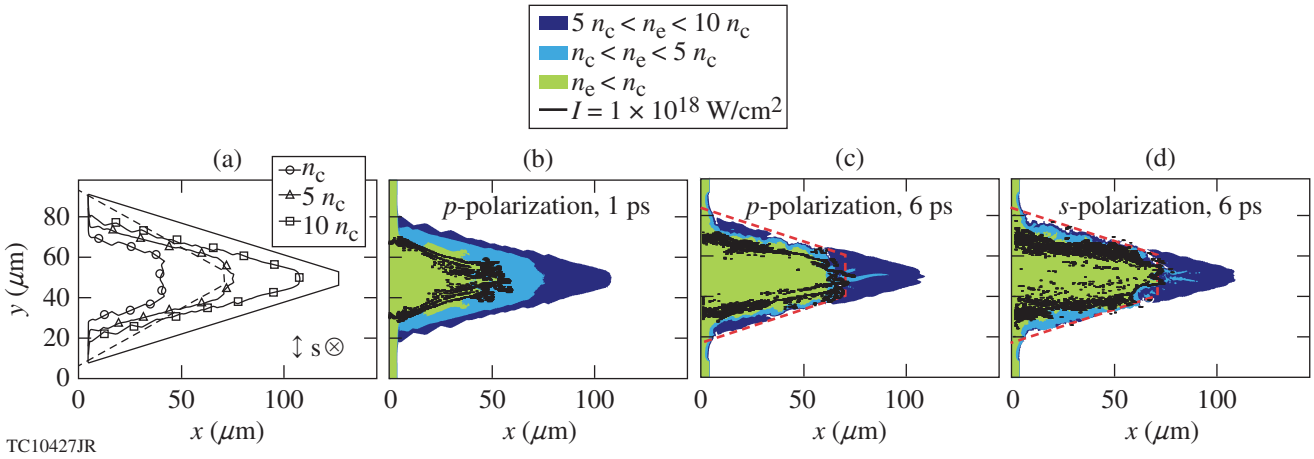

Figure 134.45

(a) Initial setup of pre-plasma inside the cone. The double arrow and the circle with a cross show the oscillation directions of the electric field for *p*- and *s*-polarizations. The solid line is the boundary (100 n_c) and the dashed line is the first diagnostic boundary. Plasma density and magnitude of the laser Poynting vector for *p*-polarization at (b) 1 ps and (c) 6 ps and (d) for *s*-polarization at 6 ps. The white regions indicate electron density $n_e > 10\ n_c$. The solid black lines show the laser intensity contours of 1.0×10^{18} W/cm^2. In (c) and (d), the red dashed lines are the boundaries for checking charge balance.

The incident laser with wavelength $\lambda = 1.053\ \mu$m was launched at time $t = 0$ from the left side and focused at the cone tip with a peak intensity of 1×10^{19} W/cm^2 and a rise time of 0.56 fs. This short rise time was chosen to speed up the simulation. The transverse profile of the laser intensity was Gaussian with a full width at half maximum (FWHM) of $w_0 = 21\ \mu$m. Both *p*- and *s*-polarizations were used in separate simulation runs to infer three-dimensional (3-D) effects. For comparison, the 1.053-μm-wavelength short pulse from OMEGA EP had an energy of ~1 kJ and a 10-ps duration and was focused to a spot with a diameter of $D_{80} = 52 \pm 4\ \mu$m containing 80% of the laser energy. The peak intensity exceeded 1×10^{19} W/cm^2, while the average intensity within D_{80} was several times 10^{18} W/cm^2.

The simulation box size was $150 \times 100\ \mu$m. The Cartesian grid sizes dx and dy were set at $0.05\ c/\omega_0 = 7.96 \times 10^{-3}\ \mu$m and the time step at $dt = 0.035/\omega_0 = 1.86 \times 10^{-2}$ fs, where ω_0 and c are the laser-pulse frequency and the speed of light, respectively. The total number of grid cells was 17,856 × 11,900. The number of particles per cell was chosen to be 10, 1, and 4 for Species 1, 2, and 3, respectively. For electromagnetic fields, we used open boundary conditions in the x (longitudinal) direction and periodic boundary conditions in the y (transverse) direction.

For particles, a thermal boundary condition was used at all four boundaries; electrons reaching the boundaries were reflected with a new Maxwellian velocity distribution at the initial temperature (1 keV). To prevent hot electrons from accumulating near the boundaries, an artificial drag[12] was introduced on electrons above 30 keV outside the cone

$$\frac{d\vec{v}}{dt} = -\alpha\vec{v}, \tag{1}$$

where $\vec{v}$ is the electron velocity normalized to c and t is the time normalized to $1/\omega_0$. The drag coefficient α was chosen to be 0.0043, which would stop a 1-MeV electron in 17 μm.

The initial density change was represented by a change in the charge weights of the particles while the number of particles per cell was initially constant throughout the simulation box. Therefore, the particles in higher-density regions had larger charge weights than the particles in lower-density regions.

Figure 134.45(a) shows the initial setup for the PIC simulations with different contours matching the critical (n_c), 5-n_c, and 10-n_c density lines inside the cone that were obtained from the *HYDRA* simulation. It is noted that the full-scale plasma in the cone tip was implemented in the simulation and that the target was the same as in the integrated experiments (34° full inner cone angle, 10-μm flat tip, Au cone wall, and pre-plasma). Hot-electron diagnostics were set up at two places as shown in Fig. 134.45(a). The first diagnostic boundary (dashed line) was near the initial $n_e = 5$-n_c surface and the other was at the cone boundary, where $n_e = 100\ n_c$. Whenever an electron passed one of these diagnostic boundaries, its position, momentum, and charge weight were recorded. The incoming and outgoing electrons were separately recorded at these two boundaries. In this article, when calculating hot-electron–related quantities such as average energy, a net distribution function of the hot electrons (>30 keV) was usually used:

$$f_{\text{hot}} = f_{\text{outgoing}} - f_{\text{incoming}}, \quad (2)$$

where the flux was normal to the cone boundary. This definition excluded the hot electrons trapped near the boundaries.

Simulation Results

1. Laser Propagation Inside the Cone

To illustrate the laser and plasma evolution inside the cone, we plot the contours of plasma density and the magnitude envelope of the laser Poynting vector at time $t = 1$ ps [Fig. 134.45(b)] and at 6 ps [Fig. 134.45(c)] for the p-polarization case, and at $t = 6$ ps [Fig. 134.45(d)] for the s-polarization case. The initial position of n_c was ~85 μm away from the cone tip and was pushed ~25 μm forward with s-polarization (~60 μm from cone tip) and ~30 μm with p-polarization (~55 μm from cone tip) at 6 ps. At 1 ps, the laser intensity contour of 1.0×10^{18} W/cm^2 interacted with $n_c < n < 5$-n_c plasma. At 6 ps, however, the plasma was pushed transversely to both sides so that the side n_c surface was far from the laser intensity contour of 1.0×10^{18} W/cm^2. In this case hot electrons can be generated only in the underdense plasma. At the end of the simulation ($t = 6.7$ ps), the laser had not reached the original 10-n_c surface, demonstrating the importance of the pre-plasma effect for hot-electron generation inside the cone.

2. Establishment of Return Currents

For the laser to continuously generate hot electrons from the pre-plasma inside the cone during the time considered, there must be a return current drawn from outside the laser–plasma interaction region. Any inhibition of this return current would lead to the buildup of an electrostatic field, preventing further electron acceleration. This could occur numerically as a result of the high weight of the particles in the 100-n_c region, preventing them from moving freely into a region with a density near n_c.

Therefore, the total charges of Species 1 and 3 inside a region defined by the red dashed line in Figs. 134.45(c) and 134.45(d) are plotted as a function of time in Fig. 134.46(a) for p-polarization and Fig. 134.46(b) for s-polarization. The total charge of Species 1 (the electrons originally inside the cone) decreased over time as a result of laser acceleration. In the meantime, Species 3 (the electrons originally outside the cone) moved into the cone to form the return currents, as shown in Figs. 134.46(a) and 134.46(b). The total charge of Species 1 and 3 inside this region was very close to the total charge of Species 2 (the ions, not shown) throughout the simulation, which decreased at later times as the ions were expelled. Similar results were obtained for other regions where $n_e < 3$ n_c and $n_e < 30$ n_c. Therefore, the charge was mostly balanced

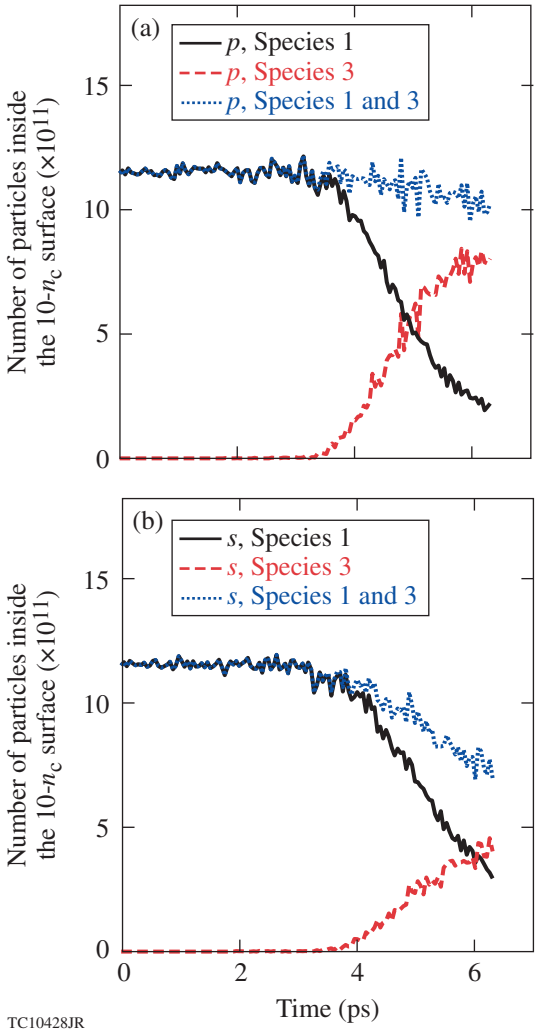

Figure 134.46
Total charge of the electron Species 1 and 3 inside the 10-n_c surface in the unit of electron charge for (a) p-polarization and (b) s-polarization.

and the return current was well established in our simulations. We note that more electrons were pushed out of the cone early for the p-polarized laser beam than for the s-polarized laser beam. We will discuss the reason for this feature in **Energy Density of Electrons** (p. 132).

3. Laser-to-Hot-Electron Conversion Rates and Hot-Electron Energy Spectra

To study how much laser energy was transferred into hot electrons, we define an instantaneous laser-to-hot-electron conversion rate as the total energy of the net outgoing hot electrons normalized by the incident laser energy in a short period of ~0.05 ps. To calculate this rate, the contribution from the incoming hot electrons was subtracted, using Eq. (2). The instantaneous conversion rates of both p- and s-polarized laser

beams are shown in Fig. 134.47(a). Initially, the *p*-polarized laser beam had a higher conversion rate than the *s*-polarized laser beam, but the difference decreased at later times. The conversion rates from 3.5 to 6.7 ps for both cases were about 50%.

The mean energy of the hot electrons is shown in Fig. 134.47(b) as a function of time. The mean energies for the *p*- and *s*-polarized cases reached maximum values of 2 MeV and 1.5 MeV at 0.74 ps and 0.93 ps, respectively; they then decreased over time. This trend was the opposite from that in Ref. 14, where no significant pre-plasma was present, indicating a different hot-electron–generation mechanism in these simulations [see **Energy Density of Electrons** (p. 132)]. After 4 ps, the *p*- and *s*-polarized cases had about the same mean energies.

The energy spectra for accumulated hot electrons for both polarizations are plotted in Fig. 134.47(c). The overall spectra are similar. They can be fitted by a two-temperature function

$$f(E) = 1.06\times 10^{11}\exp\left(-E/0.12\right) + 5.8\times 10^{8}\exp\left(-E/3.3\right), \quad (3)$$

where E is the electron energy in MeV. The temperature was 0.12±0.03 MeV for the "cold" component (below 500 keV) and 3.3±0.2 MeV for the "hot" component (above 1 MeV). The hot-component temperature was 3.5× the ponderomotive energy (corresponding to the laser intensity of 1×10^{19} W/cm^2) of 0.95 MeV. This again indicates a different hot-electron–generation mechanism from that in previous simulations with no significant pre-plasma.[15]

To describe the spectra in more detail, we define an electron energy fraction function $g(E)$ that is the fraction of the electron energy below E:

$$g(E) = \frac{\int_{30\,\mathrm{keV}}^{E} f(E')E'\,\mathrm{d}E'}{\int_{30\,\mathrm{keV}}^{E_{\max}} f(E')E'\,\mathrm{d}E'}, \quad (4)$$

where $f(E)$ is the distribution function of the hot electrons from Eq. (2) and $E_{\max}$ is chosen to be 30 MeV, above which there were few electrons.

Figure 134.47(d) plots $g(E)$ for the accumulated hot-electron spectra for both polarizations. While the mean hot-electron energies at the end of the simulations dropped below 0.5 MeV, the sub-1-MeV electrons contributed only 22% of the total hot-electron energy, as indicated by point A. The electron distribution was dominated by the low-energy electrons in number but by the high-energy electrons in energy. The median energy E_M, defined as $g(E_M) = 0.5$, was much higher than the mean energy of the distribution in Fig. 134.47(b). In Fig. 134.47(d), the median energy E_M was 4.2 MeV for the *p*-polarized case and 3.7 MeV for the *s*-polarized case. These data clearly show that the hot-electron energy is mainly carried by high-energy electrons.

4. Angular Distribution of Hot Electrons

The divergence of the electrons above 1 MeV is one of the quantities critical to the ultimate energy-coupling efficiency in fast ignition. Here, we define the half spread angle of an electron as

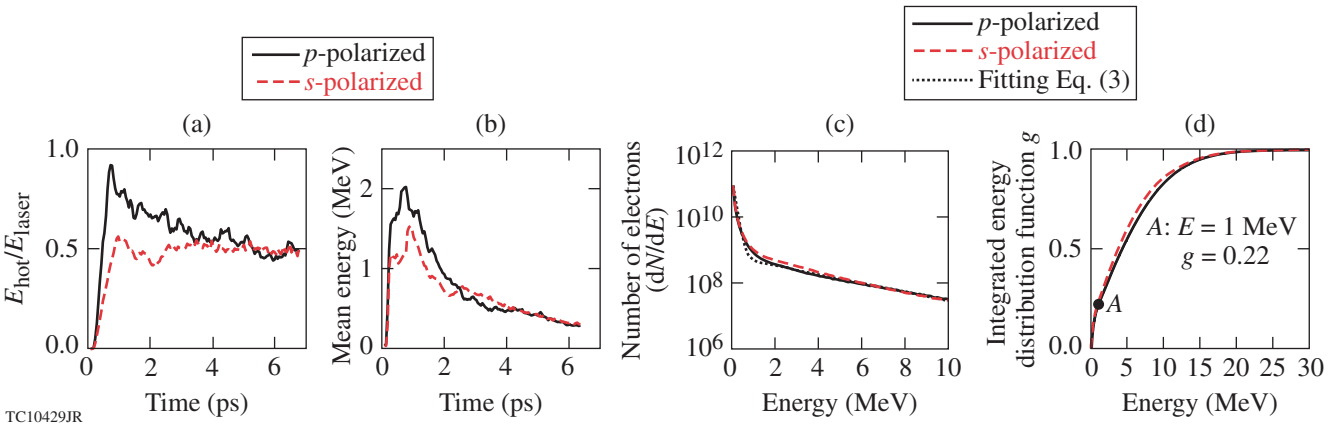

Figure 134.47
(a) Instantaneous laser-to-hot-electron conversion rate; (b) mean energy of the outgoing hot electrons; (c) accumulated hot-electron energy spectra and the fitting [Eq. (3)]; and (d) function g in Eq. (4) for accumulated hot electrons. All plots are shown for both *p*- and *s*-polarization cases.

$$\theta = \tan^{-1}\left(\frac{p_y}{p_x}\right), \tag{5}$$

where p_x and p_y are the momenta of the electron in the x and y directions.

Since the hot electrons were dominated in number by low-energy electrons, we plot the normalized angular distribution of hot electrons with and without energy weighting in Fig. 134.48(a). These distributions show that a significant amount of energy was carried by electrons with a large θ. The energy-weighted, mean half-angle

$$\sum_i \theta_i q_i E_i \Big/ \sum_i q_i E_i$$

of the hot electrons is plotted in Fig. 134.48(b), where q_i and E_i are the charge weight and kinetic energy of each particle, respectively. The mean half-angle for the accumulated distribution increased slightly over time and was between 58° and 68°.

5. Ballistic Electron Motion Inside the Cone

A realistic electron source is vital for the transport study of hot electrons in fast ignition.[10,15–17] Figure 134.49 plots the energy-weighted angular spread and energy spectra from

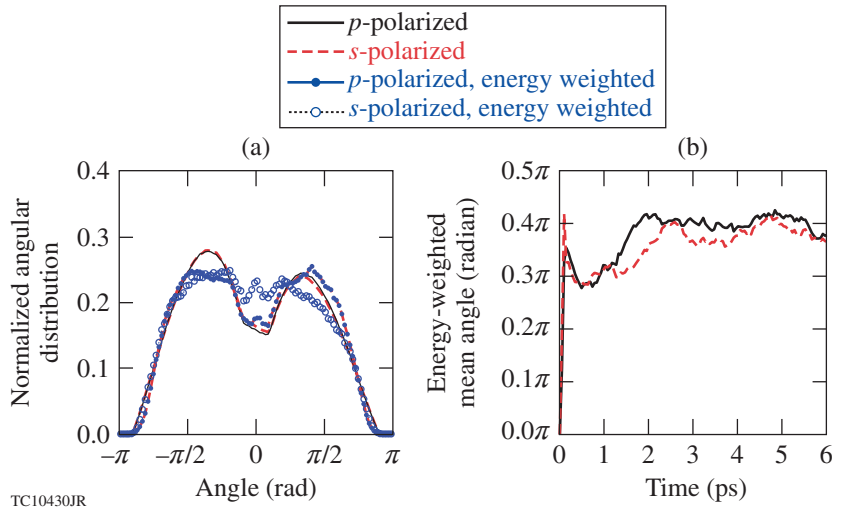

Figure 134.48
(a) Normalized angular distribution of accumulated hot electrons with and without energy weighting; (b) energy-weighted mean angle of accumulated hot electrons versus time for p- (solid) and s-polarization (dashed).

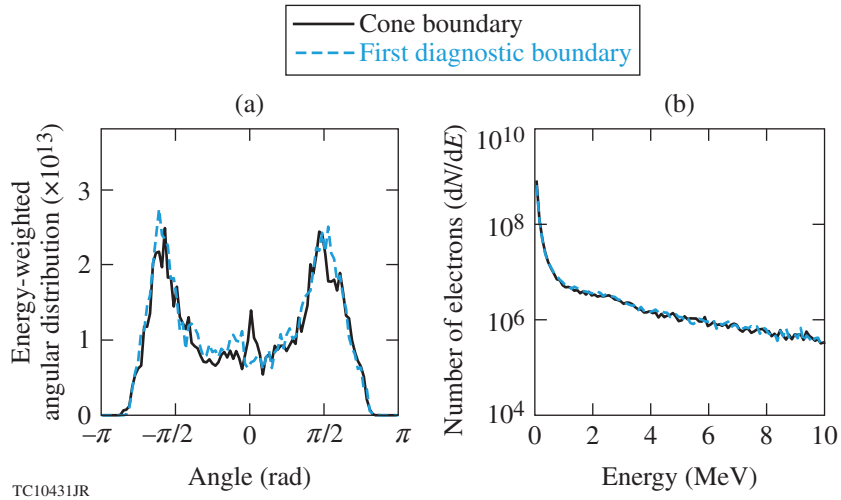

Figure 134.49
(a) Energy-weighted angular distribution at 1.96 ps < t < 2.01 ps and (b) corresponding energy spectrum recorded at the cone boundary (solid) and the first virtual boundary (dashed).

both the first diagnostic boundary [see Fig. 134.45(a)] and the cone boundary at 1.96 ps < t < 2.01 ps. The similarity of the electron characteristics shows that the transport between the two boundaries was mostly ballistic. This makes it possible to build an electron source from the information collected at the cone boundary for future transport study.

6. Energy Density of Electrons

The observed hot-electron characteristics, including the accumulated energy and angular distributions and the long-term laser-to-hot-electron conversion rates, were similar for *p*- and *s*-polarizations. Significant differences existed only early in time (Fig. 134.47), indicating that some of the known laser-heating mechanisms operating only in *p*-polarization, such as resonant[18,19] and Brunel[20] heating, were not dominant in these simulations. To further illustrate this, the electron energy densities at two different times for both polarizations are plotted in Fig. 134.50. The normalized electron energy density is defined as

$$h(x,y) = n_e(x,y)\bar{E}_k(x,y) \Big/ \left(n_c mc^2\right), \tag{6}$$

where $n_e(x,y)$ is the total electron density, including both Species 1 and 3; $\bar{E}_k(x,y)$ is the mean kinetic energy of local electrons; and n_c, m, and c are the previously defined quantities. Initially, with the uniform electron temperature T_e = 1 keV, $h(x,y)$ was in the range [0, 0.3]. When hot electrons are present, $h(x,y)$ can increase to the range [1, 3], as shown by the regions in black in Fig. 134.50. Therefore, Fig. 134.50 essentially plots the hot-electron energy density.

At 1 ps [Figs. 134.50(a) and 134.50(b)], both polarizations show the highest hot-electron densities in the laser region and hot-electron fluxes in the forward direction. For *p*-polarization, however, additional fluxes were propagating sideways. The sideways fluxes had a modulated structure with a wavelength close to the laser wavelength λ. They appeared to originate from the edge of the laser beam, where the electron density was approximately n_c and the density scale length was $\sim\lambda$ [see also Fig. 134.45(b)]. This indicates that Brunel heating[20] was the likely generation mechanism for these sideways hot electrons and accounts for the higher conversion rate for the *p*-polarization in Fig. 134.47(a). The return current for the *p*-polarization also emerged earlier in Fig. 134.46(a).

At 6 ps, more sideways fluxes appeared for both polarizations [Figs. 134.50(c) and 134.50(d)]; however, these fluxes did not have a modulated structure, indicating that they were no longer generated by the Brunel mechanism. This is also corroborated by the fact that the n_c surface moved away from the laser region [Figs. 134.45(c) and 134.45(d)]. Most hot electrons were likely generated stochastically through interactions of the laser pulse with the underdense plasma. From particle trajectories, we observed many hot electrons passing through the laser region multiple times before crossing the cone boundary. Actual heating processes are difficult to analyze but they can be a high-intensity analog of the stochastic heating from mode coupling in parametric instabilities[21] and/or the stochastic heating from the laser pulse and its reflection.[22,23] The electrons can be heated stochastically to an energy much higher than the laser ponderomotive potential.[24] The sideways fluxes in

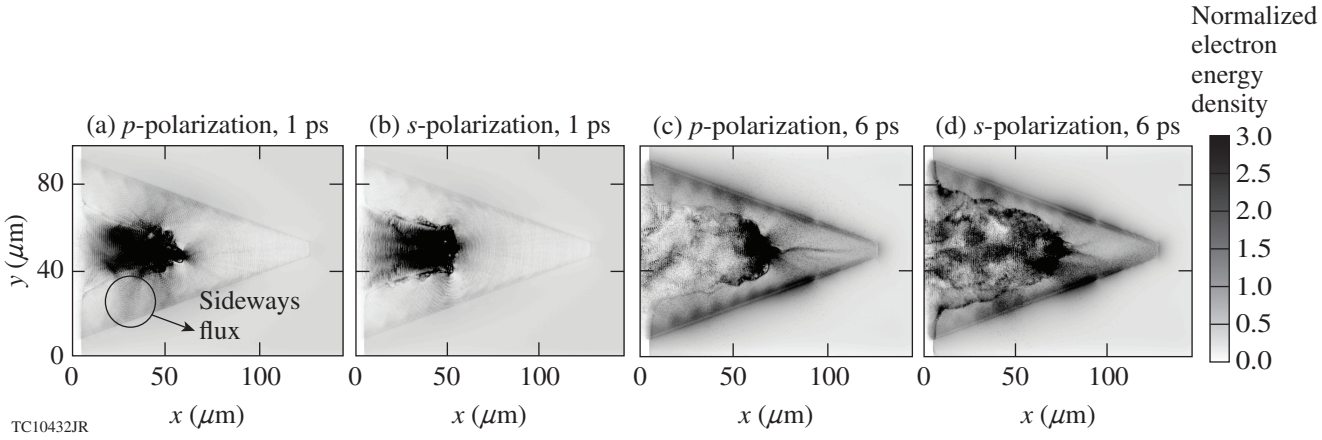

Figure 134.50
Energy density of all electrons (Species 1 and 3) for a *p*-polarized laser beam at (a) 1 ps and (c) 6 ps and for an *s*-polarized laser beam at (b) 1 ps and (d) 6 ps.

Figs. 134.50(a) and 134.50(b) explain the large spreading angles in Figs. 134.48(a) and 134.48(b). The stochastic heating is independent of the polarization direction and the hot electrons generated are relatively isotropic. The large spreading angles observed here have a different origin from the deformation of the laser/overdense-plasma interface observed in previous simulations where no significant pre-plasmas were present.[14,25,26]

Discussion and Summary

Figure 134.51 compares several measured electron spectra from the integrated experiments[4] and the simulated spectrum of the outgoing electrons. In the experiment, fast electrons that escaped the target were recorded in two different directions: in the laser's forward direction [Fig. 134.51(a)] and sideways [Fig. 134.51(b)] at an angle of 79° to the laser-beam axis. For the simulation, the simulated outgoing electrons with an absolute angle of less than 9° and between 70° and 88°, respectively, were considered as forward and sideways electrons. They are also plotted in Fig. 134.51 multiplied by a factor of 20 to allow for a better comparison with the experimental data. The choice of an angular range of ±9° is arbitrary but justified by the fact that over this range, the shape of the simulated electron spectrum was uniform. Despite the shot-to-shot fluctuations in the measured spectra, the experimental and simulated spectra are remarkably similar in the high-energy region above ~10 MeV. A quantitative comparison of the simulated and measured spectra over the entire energy range is made difficult by the fact that the escaped electrons measured in the experiments were influenced by the electron transport in the dense ($n_e > 100\ n_c$) plasmas, which was not simulated here. Strong self-generated electric and magnetic fields in the dense plasma region would affect the directionality of lower-energy electrons ($\lesssim$1 MeV) and were not taken into account in the simulation data. It is expected, however, that the high-energy tail of the escaped electrons was less influenced by the transport and that inferred slope temperatures should be comparable. Figure 134.52 shows the inferred slope temperatures from the electron spectra in the 10- to 20-MeV energy range of Fig. 134.51. The circles correspond to the spectra in the forward direction and the triangles correspond to the sideways spectra. The square

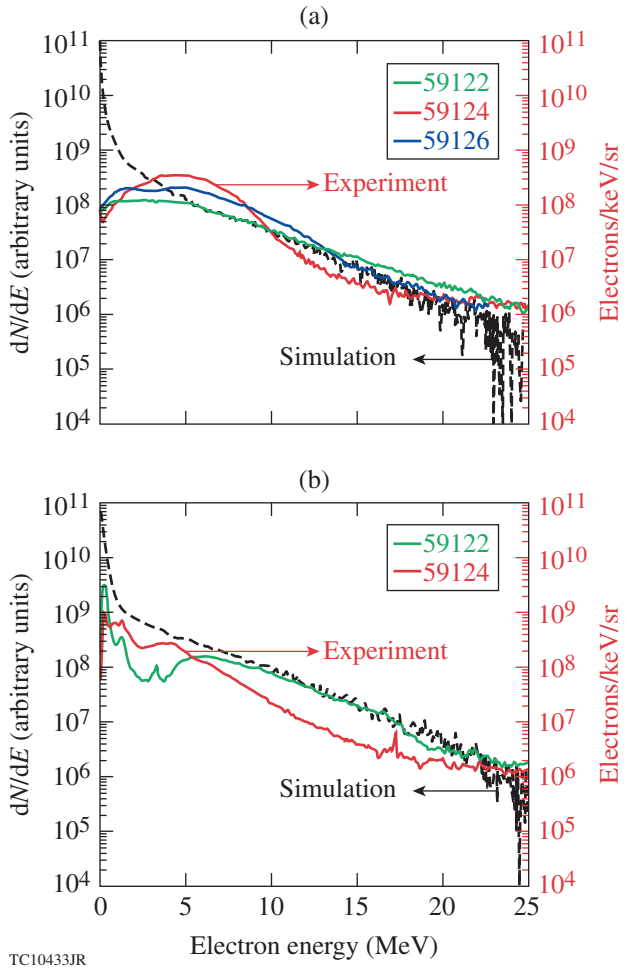

Figure 134.51
Comparison of measured (solid) and simulated (dashed) electron spectra in (a) the laser's forward direction and (b) approximately 79° to the laser-beam direction.[4]

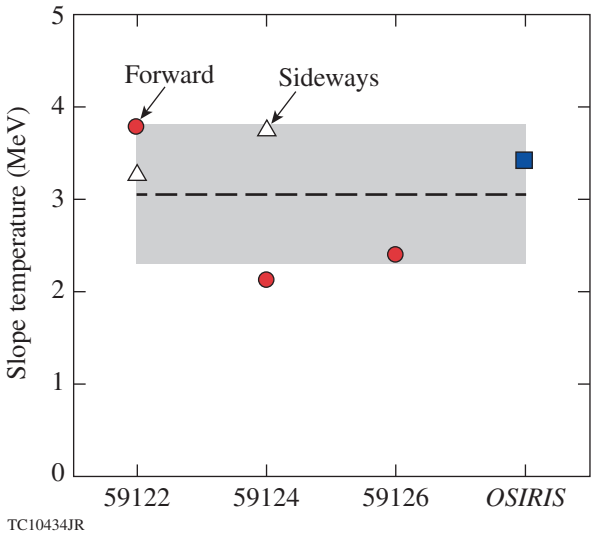

Figure 134.52
Inferred slope temperature from the electron spectra in Fig. 134.51 in the 10- to 20-MeV energy range. The circles correspond to the spectra in the forward direction and the triangles correspond to the sideways spectra. The square represents the simulation result. The dashed line is the average of the five measurements and the gray band represents the measurement uncertainty (range equal to twice the standard deviation).

represents the simulated temperature. The dashed line is the average of the five measurements, 3.05 MeV, which is close to the simulated value of 3.4 MeV within the measurement uncertainty (gray band). This shows good agreement between the simulation and the experiment. The laser–core energy coupling rate in the simulation is estimated by assuming the compressed dense deuterated plastic core is 115 μm away from the laser–plasma interface with an areal density of 0.1 g/cm^2 and a diameter of 160 μm. These conditions were obtained from the previous hydrodynamic simulations of the implosion.[27] With the assumption of ballistic motion, hot electrons with a deflection angle smaller than 35° can reach the dense core and deposit energy there. Considering the different energy-deposition rates of hot electrons with different energies, the total energy-coupling rate from laser beam to the dense core is ~0.9%, which is less than the 3.5±1.0% estimation from the integrated-experiment results. There are two possible reasons for the inconsistency. First, a self-generated magnetic field could exist that can couple the electrons with a larger deflection angle to the core.[9,28] Second, the neutrons might be generated by fast-electron–induced shocks in the core plasma. Such shocks can be generated either by direct heating of the core by fast electrons or by hydrodynamic expansion of the gold cone heated by fast electrons to ~1 keV (Ref. 4). A significant number of electrons were recorded in the sideways direction, corroborating a large divergence angle of the electrons. The large hot-electron spread angles found here can qualitatively explain the low laser–core coupling in these experiments. It is worth noting that recent integrated-experiments[29] using Cu-doped shells and monochromatic imaging of the Cu K$_\alpha$ fluorescence emission induced by the fast electrons also showed that a significant amount of hot electrons hit the side wall of the cone, which is again an indication of the large angular spread of the electrons consistent with the simulations. These simulations will help us gain a further understanding of the integrated experiments, and the hot-electron source from the simulations can be used in transport studies.

In summary, we have studied the properties of hot electrons generated during laser/pre-plasma interactions in cone-guided fast ignition over 6.7 ps using PIC simulations. Hot electrons were generated mainly through stochastic heating, which produced similar hot-electron characteristics for *p*- and *s*-polarizations in 2-D, indicating that this will also be the case in 3-D. The laser-to-hot-electron conversion rate approached 50%. Electrons with energy <300 keV dominated in number in the distribution but 78% of the hot-electron energy was carried by electrons with energy above 1 MeV. The hot electrons had an energy-weighted mean half-angle of 68°. The electron transport in the 5-n_c to 100-n_c region was ballistic. These results provide further evidence of the detrimental effects of pre-plasma in the cone.

ACKNOWLEDGMENT

This work was supported by U.S. Department of Energy under Grant Nos. DE-FG02-06ER54879, DE-FC02-04ER54789, DE-FG52-06NA26195, and DE-FG02-03ER54271. The simulations used resources of the National Energy Research Scientific Computing Center.

REFERENCES

1. M. Tabak *et al*., Phys. Plasmas **1**, 1626 (1994).
2. R. Kodama *et al*., Nature **412**, 798 (2001).
3. R. Kodama *et al*., Nature **418**, 933 (2002).
4. W. Theobald, A. A. Solodov, C. Stoeckl, K. S. Anderson, R. Betti, T. R. Boehly, R. S. Craxton, J. A. Delettrez, C. Dorrer, J. A. Frenje, V. Yu. Glebov, H. Habara, K. A. Tanaka, J. P. Knauer, R. Lauck, F. J. Marshall, K. L. Marshall, D. D. Meyerhofer, P. M. Nilson, P. K. Patel, H. Chen, T. C. Sangster, W. Seka, N. Sinenian, T. Ma, F. N. Beg, E. Giraldez, and R. B. Stephens, Phys. Plasmas **18**, 056305 (2011).
5. A. G. MacPhee *et al*., Phys. Rev. Lett. **104**, 055002 (2010).
6. H. Shiraga *et al*., Plasma Phys. Control. Fusion **53**, 124029 (2011).
7. S. D. Baton *et al*., Phys. Plasmas **15**, 042706 (2008).
8. G. Li *et al*., Phys. Rev. Lett. **100**, 125002 (2008).
9. G. Li *et al*., Phys. Plasmas **18**, 042703 (2011).
10. A. A. Solodov, K. S. Anderson, R. Betti, V. Gotcheva, J. Myatt, J. A. Delettrez, S. Skupsky, W. Theobald, and C. Stoeckl, Phys. Plasmas **15**, 112702 (2008).
11. R. A. Fonseca *et al*., Lect. Notes Comput. Sci. **2331**, 342 (2002).
12. J. Tonge *et al*., Phys. Plasmas **16**, 056311 (2009).
13. M. M. Marinak *et al*., Phys. Plasmas **3**, 2070 (1996).
14. A. J. Kemp and L. Divol, Phys. Rev. Lett. **109**, 195005 (2012).
15. D. J. Strozzi *et al*., Phys. Plasmas **19**, 072711 (2012).
16. J. J. Honrubia and J. Meyer-ter-Vehn, Nucl. Fusion **46**, L25 (2006).
17. T. Johzaki, Y. Nakao, and K. Mima, Phys. Plasmas **16**, 062706 (2009).
18. D. W. Forslund *et al*., Phys. Rev. A **11**, 679 (1975).
19. K. Estabrook and W. L. Kruer, Phys. Rev. Lett. 40, **42** (1978).
20. F. Brunel, Phys. Rev. Lett. **59**, 52 (1987).

21. J. J. Thomson, R. J. Faehl, and W. L. Kruer, Phys. Rev. Lett. **31**, 918 (1973).

22. Z.-M. Sheng *et al*., Phys. Rev. Lett. **88**, 055004 (2002).

23. Z.-M. Sheng *et al*., Phys. Rev. E **69**, 016407 (2004).

24. S. C. Wilks *et al*., Phys. Rev. Lett. **69**, 1383 (1992).

25. A. Debayle *et al*., Phys. Rev. E **82**, 036405 (2010).

26. H. Schmitz, R. Lloyd, and R. G. Evans, Plasma Phys. Control. Fusion **54**, 085016 (2012).

27. A. A. Solodov, M. Theobald, A. S. Anderson, A. Shvydky, R. Betti, J. F. Myatt, and C Stoeckl, Bull. Am. Phys. Soc. **57**, 29 (2012).

28. A. A. Solodov, K. S. Anderson, R. Betti, V. Gotcheva, J. F. Myatt, J. A. Delettrez, S. Skupsky, W. Theobald, and C. Stoeckl, Phys. Plasmas **16**, 056309 (2009).

29. L. C. Jarrott, M. S. Wei, A. A. Solodov, H. Sawada, R. B. Stephens, A. Greenwood, D. Hoover, N. Alfonso, H. Huang, E. Giraldez, W. Theobald, C. Stoeckl, F. J. Marshall, J. Delettrez, R. Betti, P. K. Patel, H. McLean, C. Chen, M. K. Key, H. Chen, T. Doeppner, T. Yabuuchi, H. Habara, and F. N. Beg, presented at the 2012 Stewardship Science Academic Alliances (SSAA) Symposium, Washington, D.C., 22 February 2012.

Pulsed Laser Ablation of Dental Calculus in the Near-Ultraviolet

Introduction

Selective removal of subgingival dental calculus is a preferred treatment method in nonsurgical periodontal therapy. While complete removal of calculus and disease-causing agents (i.e., oral bacteria) is of primary importance, leaving behind a hard tissue surface less prone to bacterial accumulation is also important. Grooves and craters resulting from conventional cleaning measures provide sites for future bacteria and calculus crystals to accumulate.[1] Healthy cementum should be preserved since attachments, via periodontal ligaments, from either the gingiva or alveolar bone with root dentin are not as strong as with root cementum.[2,3] A weak connection could lead to subsequent reoccurrence of periodontal problems.

Conventional methods to remove calculus typically depend on the experience of the clinician[4,5] and other treatment factors.[1] Unintentional damage can easily occur using hand instruments[6] and power-driven scalers (e.g., ultrasonic and air abrasion)[7] that cause grooves and/or excessive cementum removal. In most cases, mechanical root scaling leaves behind a smear layer containing harmful bacteria, infected cementum, and calculus debris.[8,9]

Currently, the Er:YAG laser (λ = 2.94 μm) (Ref. 10) is the only commercially available laser with significant experimental and clinical studies for dental hard tissue removal.[1] Hard-tissue (enamel, dentin, and cementum) ablation at this wavelength relies on absorption by water,[11] so calculus ablation is not selective. A review of several clinical studies[12] and recent meta-analysis[13] concluded that the clinical outcome of calculus removal using the Er:YAG laser is similar to conventional mechanical debridement.

A frequency-doubled alexandrite (FDA) laser ($\lambda \sim 380$ nm) can selectively remove plaque, caries, and calculus without damaging the underlying and surrounding hard tissue.[14] The ablation mechanism is assumed to be based on absorption by haemins (i.e., iron-containing porphyrins) into the Soret band.[15,16] Iron-containing porphyrins are found in some oral bacteria in dental plaque and dental calculus.[15,17] However, the inconsistent output of the FDA laser has not allowed for more-detailed studies into the calculus ablation mechanism.

Recently, a frequency-doubled Ti:sapphire laser (λ = 400 nm) was developed to allow for a more-detailed analysis of dental calculus ablation in the near-ultraviolet (NUV, 300 to 400 nm) (Ref. 18). This laser selectively removes dental calculus[19,20] and extrinsic enamel stains.[21] For incident laser fluences close to the ablation threshold (1 to 2 J/cm^2), ablation stalling is frequently encountered. Stalling is not observed at fluences well above the ablation threshold (6 to 8 J/cm^2).

This article describes a variety of experimental diagnostics used to study the ablation mechanism of dental calculus at 400 nm and compares the results with predictions made by heuristic ablation models. Laser profilometry measures volume and depth of calculus ablated for different irradiation conditions. Blue-light microscopy and fluorescence spectroscopy identify photobleaching during calculus ablation. Together these diagnostics allow one to identify a heuristic, modified ablation blowoff model that explains the experimental observations. Finally, the effect of tooth sterilization prior to laser irradiation is assessed by comparing removal rates of gamma-ray–sterilized and unsterilized calculus samples at the same incident fluence. This information has been used to propose a mechanism for calculus ablation at 400 nm.

Heuristic Ablation Models

1. Standard Blowoff Model

In the standard blowoff model, Beer's law is assumed to govern energy deposition into calculus.[22] In this model, deposited energy densities E_d exceeding the ablation-threshold energy density E_abl cause calculus removal. The threshold energy density is typically a constant[22,23] related to the enthalpy of ablation for calculus. The absorption coefficient μ_a is assumed to remain constant during irradiation, and scattering is assumed to be negligible. For the standard blowoff model, E_d is given by

$$E_\mathrm{d} = -\frac{\mathrm{d}F}{\mathrm{d}z} = \mu_\mathrm{a} F(z) = \mu_\mathrm{a} F_0 e^{-\mu_\mathrm{a} z}, \quad (1)$$

where F_0 is the incident fluence (in J/cm^2) and $F(z)$ is the fluence at depth z. Ablation occurs over the etch depth δ_{SB} if $\mu_a F(z) > E_{abl}$. Beyond the etch depth, tissue is not ablated but merely heated. The fluence at the etch depth is the ablation threshold fluence F_{th}, and for $F(z) > F_{th}$ the etch depth is found from Eq. (1) to be

$$\delta_{SB} = \frac{1}{\mu_a} \ln\left(\frac{F_0}{F_{th}}\right). \tag{2}$$

2. Modified Blowoff Model

In the modified blowoff model, the absorption coefficient is assumed to decrease during the laser pulse. This assumption may be better suited for predicting calculus-removal rates since a photobleached surface layer is observed after 400-nm irradiation.[18] This model was originally proposed for photoablation of polymethyl methacrylate (PMMA) in the deep ultraviolet.[23] For photoablation, the number density of chromophores ρ_a decreases as the absorption of UV photons breaks chemical bonds that prevent absorption of subsequent photons.[24,25] Permanent photochemical damage of the chromophores (i.e., photobleaching) similarly decreases ρ_a during laser irradiation. The derivation for the modified blowoff model is found in Ref. 23, where the approximate etch depth δ_{MB}, for the fluences used in this article, is determined to be

$$\delta_{MB} \approx \frac{F_0 - F_{th}}{h\nu\rho_a}, \tag{3}$$

where h is Planck's constant and ν is the laser frequency. The etch depth depends linearly on F_0 as opposed to the logarithmic dependence in Eq. (2) for the standard model. The full expression for Eq. (3) is found in Ref. 23. The chromophore number density is related to the absorption coefficient by $\mu_a = \sigma_a \rho_a$, where σ_a is the absorption cross section of the chromophore. The deposited energy density is approximately constant for $z < \delta_{MB}$ and is given by

$$E_d(z < \delta_{MB}) \approx h\nu\rho_a. \tag{4}$$

Equation (4) indicates that the deposited energy is limited by the chromophore number density of the tissue within the etch depth. The deposited energy density for both blowoff models is plotted as a function of depth in Fig. 134.53 based on the data in Table 134.VI. A layer consisting of partially photobleached chromophores is located beyond the etch depth in Fig. 134.53(b).

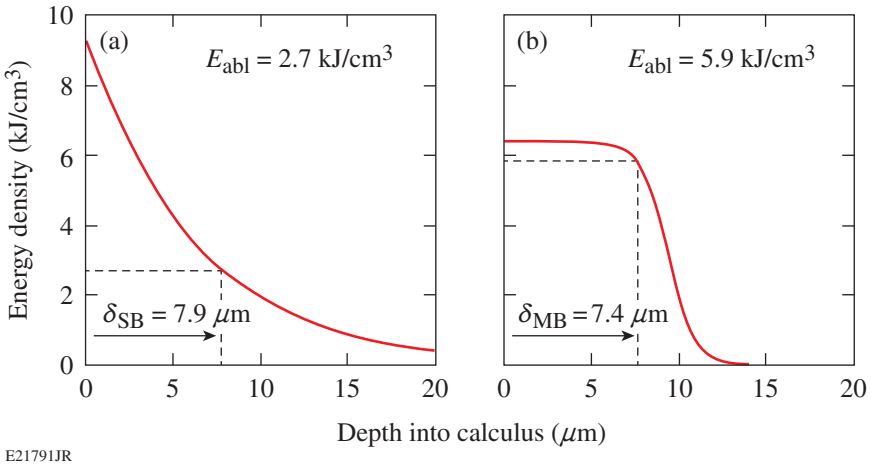

E21791JR

Figure 134.53
Deposited energy density as a function of depth in calculus based on the (a) standard and (b) modified blowoff models. The incident fluence is 6 J/cm^2. The curves are based on data in Table 134.VI. In (a) μ_a = 1600 cm^{-1} and in (b) $\rho_a = 1.3 \times 10^{22}$ cm^{-3}.

Table 134.VI: Absorption coefficients, threshold fluences, and chromophore number densities for the standard and modified blowoff models obtained from removal rates in Fig. 134.58.

	Removal Rates		Standard Blowoff Model		Modified Blowoff Model	
	$\frac{\mu\text{m/pulse}}{\text{J/cm}^2}$	$\times 10^{14}\ \frac{\mu\text{m}^3\text{/pulse}}{\text{J/cm}^2}$	μ_a (cm^{-1})	F_{th} (J/cm^2)	$\rho_a\ 10^{22}$ (cm^{-3})	F_{th} (J/cm^2)
Supragingival	1.5±0.3	6.6±1.4	1618±323	1.7±0.4	1.32±0.27	1.2±0.4
Subgingival	1.6±0.3	7.9±1.6	1574±281	1.8±0.4	1.27±0.23	1.3±0.4

3. Removal Rates

The etch depths in Eqs. (2) and (3) can be used to calculate volume removal rates for each blowoff model. Assuming an nth-order super-Gaussian fluence distribution $F(r)$, we find

$$F(r) = F_0 \exp\left(-r^n / w^n\right), \tag{5}$$

with peak fluence F_0 and $1/e$ beam width w. Substituting Eq. (5) into Eqs. (2) and (3), one obtains a radial distribution of the etch region. Scattering is assumed to be negligible compared to absorption. The volume removal rate is found by integrating over the entire volume irradiated at fluences $>F_{\text{th}}$. The volume removal rate V_{SB} per pulse for the standard blowoff model is

$$V_{\text{SB}} = \frac{2\pi w^2}{\mu_a}\left(\frac{1}{n+2}\right)\left(\ln\frac{F_0}{F_{\text{th}}}\right)^{\frac{n+2}{n}}. \tag{6}$$

The volume removal rate predicted by the modified blowoff model V_{MB} is

$$V_{\text{MB}} = \frac{2\pi^2}{\rho_a h\nu}\left[\frac{F_0\Gamma(2/n)}{n}\eta_{\text{E}}\left(n, F_0/F_{\text{th}}\right) - \frac{F_{\text{th}}}{2}\left(\ln\frac{F_0}{F_{\text{th}}}\right)^{2/n}\right], \tag{7}$$

where η_{E} is the energy efficiency for selective ablation shown in Ref. 18 and Γ is the gamma function. For our experimental conditions the volume removal rates in Eqs. (6) and (7) simplify to $V_{\text{SB}}(\mu\text{m}^3) \approx (10^8/\mu_a)$ and $V_{\text{MB}}\left(\mu\text{m}^3\right) \approx \left(F_0/\rho_a\right)\times 10^{27}$, where the units of ρ_a, μ_a, and F_0 are cm^{-3}, cm^{-1}, and J/cm^2, respectively. The underlying experimental parameters are $n = 10$, $w = 150\ \mu$m, $F_0/F_{\text{th}} \approx 4$ to 5, $\eta_{\text{E}} \approx 1$, and $h\nu = 3.1$ eV.

Materials and Methods

1. Tooth Samples

Twenty extracted human teeth exhibiting calculus, equally divided between sub- and supragingival calculus, were obtained from the Department of Preventive and Restorative Dental Sciences, School of Dentistry at the University of California, San Francisco. They were sterilized with gamma radiation and stored in a 0.1% thymol solution. Ten extracted, unsterilized human teeth with subgingival calculus were obtained from the Eastman Institute for Oral Health at the University of Rochester (UR) and stored in a saline solution.

2. Experimental Setup

A frequency-doubled Ti:sapphire laser (400-nm wavelength, 60-ns pulse duration, 10-Hz repetition rate, and 25-mJ pulse energy) was developed for selective calculus ablation and has been described elsewhere.[18] Laser radiation was coupled into a 600-μm-core-diam optical fiber with a 1.8-mm-diam tapered input (FVPE600660710/2M, Polymicro Technologies) using a $\Delta\theta = 0.5°$ engineered diffuser (RPC Photonics) and an $F = 7.5$-cm lens [Fig. 134.54(a)]. The output beam was demagnified using an $F = 2$-cm lens objective to create an ~300-μm-diam, tenth-order super-Gaussian irradiation beam on the calculus surface. This irradiation geometry was chosen to facilitate experimental observations. The peak fluence of each pulse was varied from 1.7 to 8 J/cm^2 ($\pm 0.1\ \text{J/cm}^2$) by varying the laser pulse energy. All tooth surfaces were irradiated at normal (perpendicular) incidence to the surface. (Similar ablation studies using oblique incidence were reported in Ref. 19.)

During laser irradiation, the tooth samples were sprayed with a water/air mixture at ~3 mL/min. The effect of this water spray on the intensity distribution of the irradiation laser at the tooth surface is minimal.[18] After five laser pulses, excess water was gently blown off the tooth samples using an air spray to allow for the diagnostic imaging (i.e., laser profilometry and blue-light microscopy) described below.

3. Laser Profilometry

The depth and volume of calculus removed were measured using a laser profilometer. A HeNe laser at $\lambda = 543$ nm (Model LHGR-0050, PMS Electro-Optics) was focused to a line onto the tooth surface using an $F = 10$-cm cylindrical lens and then scanned across the irradiated region before and after laser irradiation. The line was magnified 3× (VMZ450i, Edmund Industrial Optics) by imaging onto a charge-coupled–device (CCD) camera (TM-1020A-15CL, JAI) along a line of sight at 45°, resulting in an axial resolution of ~6 μm. The transverse resolution was 60 μm × 40 μm. Depth-removal maps were found by taking the difference between 3-D surface images taken before and after irradiation (as described in Ref. 19). Calculus removal rates were determined by irradiating in five-pulse increments using a remotely operated shutter in the laser cavity. The average depth and volumetric removal rate uncertainties are $\pm 0.6\ \mu$m/pulse and $1.4 \times 10^{-3}\ \mu\text{m}^3$/pulse based on the uncertainty in the 3-D surface images resulting from laser speckle and the high f number of the imaging objective.

4. Blue-Light Microscopy

Images of calculus before and after laser irradiation were taken with illumination from a flashing blue light–emitting diode (LED, $\lambda \sim 450$ to 490 nm) using the same camera used in laser profilometry, as shown in Fig. 134.54(a). Identical images were obtained when illuminating with a 400-nm light source. Blue-light illumination provides high contrast between healthy

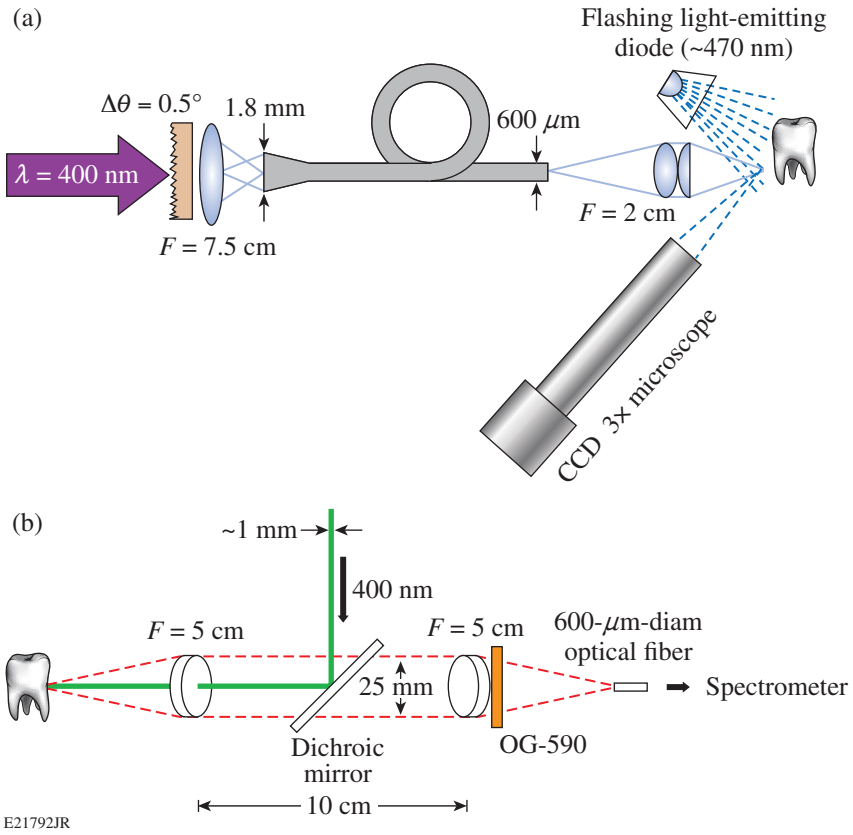

Figure 134.54
(a) Experimental setup for tooth irradiation with the 400-nm laser and for blue-light microscopy. (b) Hard tissue fluorescence between 600 and 800 nm was excited at 400 nm and coupled into an optical fiber leading to a fiber-coupled spectrometer. CCD: charge-coupled device.

hard tissue and dental calculus. It also serves to qualitatively distinguish unbleached from photobleached calculus since the latter appears brighter under blue-light microscopy because of increased scattering and decreased absorption.

5. Fluorescence Spectroscopy

Fluorescence spectroscopy was used to compare unbleached and photobleached calculus. As shown in Fig. 134.54(b), fluorescence was excited with low pulse energy (≤200 μJ at 400 nm) over a 50-μm beam spot. Fluorescence between 600 and 800 nm was then directed into a fiber-coupled spectrometer (HR2000CG-UVNI, Ocean Optics) using two F = 5-cm achromatic doublets, a dichroic mirror, and an OG590 filter. In this spectral range, one can discriminate between dental hard tissue and calculus caused by fluorescence from bacterial porphyrins.[26] At each measurement, 50 spectra were collected with a 10-s integration time, averaged, and smoothed by applying an ~5-nm spectral averaging filter.

6. Scanning Electron Microscopy

The laser-treated areas were examined using a scanning electron microscope (SEM) (Zeiss-Auriga CrossBeam FIB-SEM, Carl Zeiss NTS) at the UR's Institute of Optics. The tooth surface topology was examined using an SE2 detector and a 10-keV electron beam with a 30-μm aperture and ≤15-mm working distance. The teeth were dried in a desiccator for at least 24 h. An ~5-nm gold layer was subsequently sputtered onto the tooth surface.

Results

Blue-light microscope images show nonsterilized subgingival calculus removed at 6.4 J/cm^2 [Figs. 134.55(a)–134.55(f)] within the irradiation beam (dashed red lines). After 30 pulses, the calculus was completely removed and the underlying cementum was reached [Fig. 134.55(f)]. No ablative stalling was observed, but irradiated calculus appears brighter compared to nonirradiated calculus, indicating a photobleached surface layer. Differential depth removal maps [Figs. 134.55(g)–134.55(k)] are shown below the microscope images. Average depth and volume removal rates for nonsterilized calculus are 9.7±3.1 μm/pulse and 5.3 × 10^5±1.8 × 10^5 μm^3/pulse, respectively. Identical results are found for ablating sterilized subgingival calculus[19] at the same fluence.

Blue-light microscope and fluorescence spectra of supragingival calculus irradiated at a 3.5-J/cm^2 fluence are shown in Figs. 134.56(a) and 134.56(b). The calculus was irradiated with a 650-μm-diam, sixth-order super-Gaussian beam. The tooth

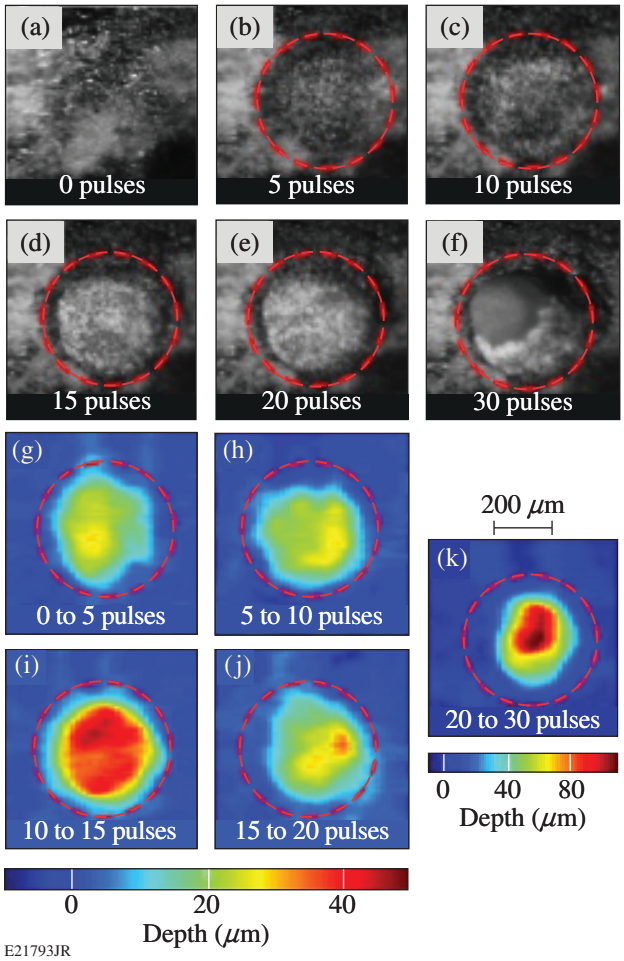

Figure 134.55
Blue-light microscope images of nonsterilized subgingival calculus irradiated at 6.4 J/cm^2 (a) before and after (b) 5, (c) 10, (d) 15, (e) 20, and (f) 30 irradiation pulses. Differential removal maps from (g) 0 to 5, (h) 5 to 10, (i) 10 to 15, (j) 15 to 20 and (k) 20 to 30 irradiation pulses correspond to the above microscope images. Red dashed circles outline the irradiation area.

was moved back and forth for 40 passes at 0.2 mm/s, resulting in ~30 superposed irradiation pulses per pass along the center on any given spot. The blue-light microscope images before and after irradiation [Figs. 134.56(a) and 134.56(b)] indicate that a layer of calculus was removed but a photobleached calculus surface layer remained [blue arrow in Fig. 134.56(b)]. The ablation stalled and further irradiation at this fluence removed no additional calculus.

Figure 134.56(c) shows the fluorescence spectra between 600 and 800 nm, excited at 400 nm, of the enamel (black arrow), unbleached calculus (red arrow), and photobleached calculus (blue arrow) indicated in Fig. 134.56(b). The fluorescence spectrum of photobleached calculus resembles the spectrum of enamel in shape, emitting more fluorescence photons than unbleached calculus [Fig. 134.56(c)]. Normalizing each spectrum [Fig. 134.56(d)] reveals that unbleached calculus has a distinct structure between 615 and 725 nm caused by the Soret band of porphyrins.[26–28] This band is not seen for either enamel or photobleached calculus. Fluorescence from these tissues originates from the hard-tissue matrix. Remnant unbleached porphyrins within the photobleached calculus likely result in the differences observed for enamel and photobleached calculus spectra.

Removing the OG590 filter in the fluorescence setup allowed us to measure the scattered/reflected signal at 400 nm. Photobleached calculus and enamel scattered twice as much 400-nm light into the collection optics as did unbleached calculus. The exact amount of 400-nm light scattered by photobleached calculus varies from tooth to tooth and can equal that for sound enamel.

Subgingival calculus irradiated with 25 pulses at 5 J/cm^2 was investigated under a SEM [Fig. 134.57(a)]. The ~100-nm pores on the calculus surface [arrows in Fig. 134.57(a)] act as

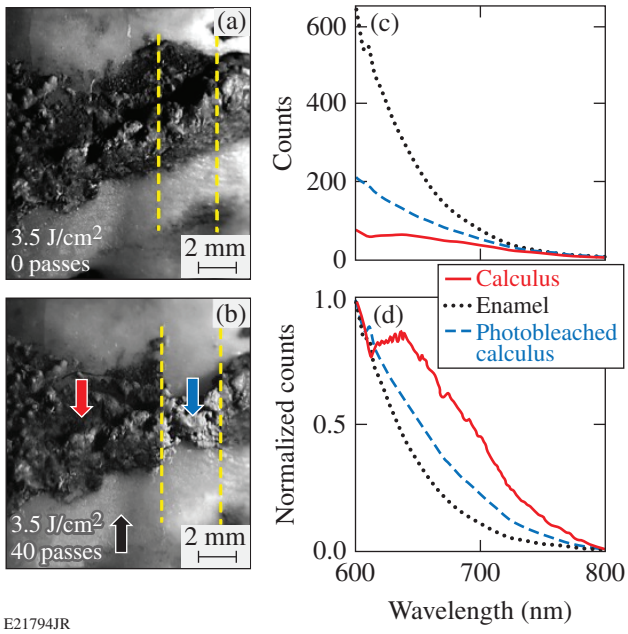

Figure 134.56
Blue-light microscope images of supragingival calculus on enamel (a) before and (b) after 40 passes at 3.5 J/cm^2 using an ~650-μm-diam, sixth-order super-Gaussian beam. The dashed yellow lines outline the irradiation path. (c) Fluorescence spectra of enamel, unbleached calculus, and photobleached calculus using a 400-nm excitation wavelength. (d) Normalized fluorescence spectra corresponding to (c). Colored arrows in (b) correspond to the spectra in (c) and (d) (i.e., red arrow: unbleached calculus; black arrow: enamel; and blue arrow: photobleached calculus).

a reservoir for oral bacteria.[29–32] For comparison, the porous surface of non-laser-irradiated calculus, covered with a biofilm, was also observed under a SEM [Fig. 134.57(b)]. The calculus surface was always covered by a layer of noncalcified dental plaque.[1] Blue-light microscope images (not shown) of the irradiated calculus surface in Fig. 134.57(a) indicate it was photobleached. The pores seen in this image were likely originally filled with oral bacteria that were removed upon NUV irradiation.

Average depth and volume removal rates for sub- and supragingival calculus are plotted as a function of incident fluence in Fig. 134.58. Within the error bars, both depth and volume removal rates increase linearly with increasing incident fluence and are indistinguishable between sub- and supragingival calculus. We have attributed the large error bars to tissue variations in absorption and/or the heterogeneity of the physical properties in calculus.[19] The absolute error in depth and volume removal rates increases with fluence in Fig. 134.58 but the relative error actually decreases. Depth removal rates in Figs. 134.58(a) and 134.58(b) are fitted to Eqs. (2) and (3). The results from these fits are summarized in Table 134 VI. The error bars render μ_a, ρ_a, and F_{th} indistinguishable for both types of calculus. The relevant tissue parameters in Table 134 VI are substituted into Eqs. (6) and (7) and plotted in Figs. 134.58(c) and 134.58(d) as predicted volume removal rates for sub- and supragingival calculus, respectively. The modified blowoff model overestimates the volume removal rate, whereas the standard model underestimates it.

The single-pulse (SP) depth and volume removal rates at ~6.3 J/cm^2 for either subgingival [Figs. 134.59(a) and 134.59(c)] or supragingival [Figs. 134.59(b) and 134.59(d)] calculus show similar trends with the number of incident pulses. The SP removal rate is calculated as the depth/volume removed from five laser pulses divided by the number of pulses, whereas the average removal rates in Fig. 134.58 are calculated from the total depth/volume removed. Outliers in the SP removal-rate data that skew the distribution are rejected according to Chauvenet's criterion.[33] The SP removal rates of sub- and

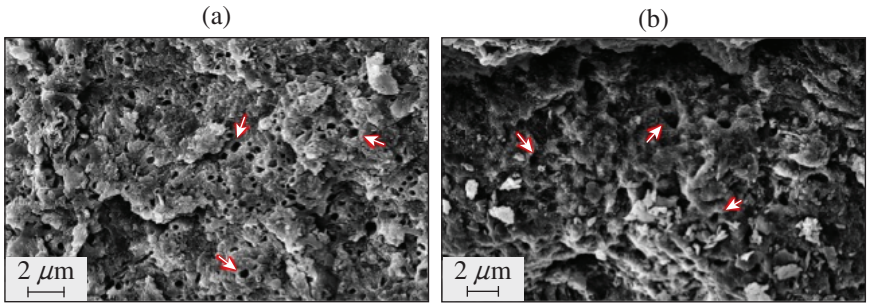

Figure 134.57
Scanning electron microscope (SEM) images of (a) laser-irradiated (5-J/cm^2) and (b) non-laser-irradiated subgingival calculus. Arrows in (a) and (b) indicate representative ~100-nm craters found in the calculus surface.

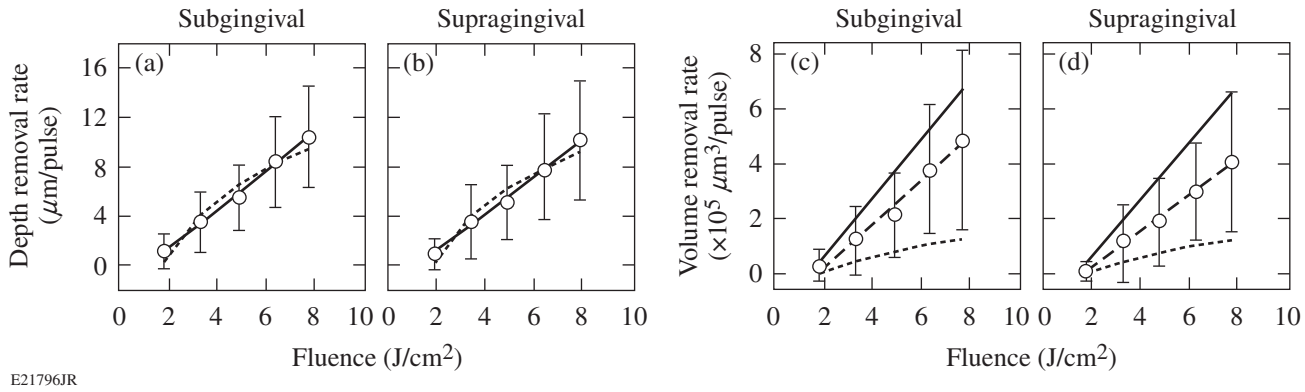

Figure 134.58
Fluence-dependent depth removal rates for (a) subgingival and (b) supragingival calculus and corresponding volume removal rates [(c) and (d), respectively]. Solid and short-dashed lines correspond to fits using the modified and standard blowoff models, respectively. Long-dashed lines in (c) and (d) are a linear regression through the data.

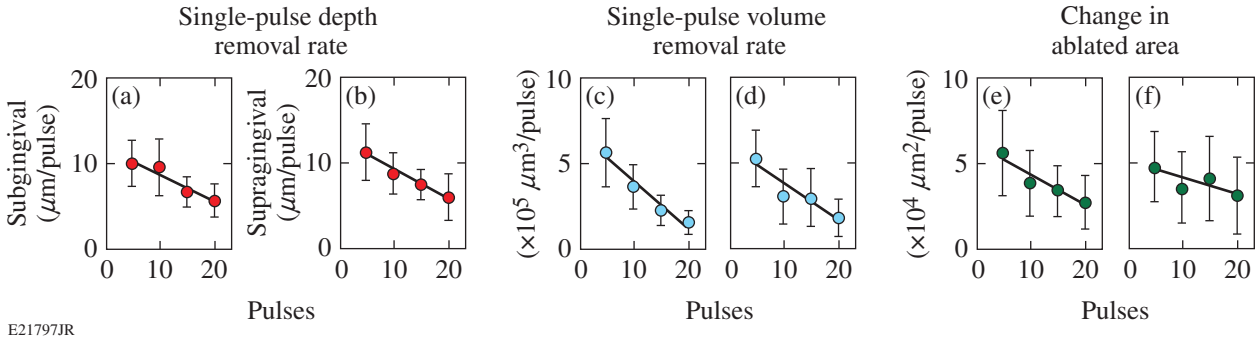

Figure 134.59
Single-pulse (SP) removal rates for all calculus samples irradiated at 6.3 J/cm^2 as a function of the number of incident pulses: the SP depth removal rates for (a) subgingival and (b) supragingival calculus; the SP volume removal rates for (c) subgingival and (d) supragingival calculus; the change in ablated area for (e) subgingival and (f) supragingival calculus. Trend lines through data are from a linear regression.

supragingival calculus at fluences from 3.5 to 7.7 J/cm^2 exhibit similar behavior. The change in the ablated area at 6.3 J/cm^2 for sub- and supragingival calculus [Figs. 134.59(e) and 134.59(f)] was found by dividing the SP volume removal rates by the SP depth removal rates in Fig. 134.59. The ablated area also decreases with increasing number of incident pulses. There is no statistically significant difference between the SP removal rates for sub- and supragingival calculus.

Discussion

The properties (i.e., pulse energy and duration) of the 400-nm laser used in this study are extremely reproducible, causing shot-to-shot variations in ablation measurements to be attributable to the material heterogeneity of calculus itself. Therefore, using the diagnostics outlined earlier allows for rather detailed inferences regarding the actual ablation mechanism. This contrasts with previous work using the 380-nm FDA laser[34] whose poor reproducibility and characterization rendered it unsuitable for this kind of detailed study. However, the selective removal of oral bacteria, dental caries, and calculus by the 380-nm laser (summarized in Ref. 14) was attributed to porphyrins endogenous to oral bacteria.

In this study, blue-light microscopy clearly indicates photobleaching and reduced absorption on the calculus surface after laser irradiation (Figs. 134.55 and 134.56). For thick calculus layers and laser fluences of less than ~6 J/cm^2, this may lead to stalling before the entire calculus layer is removed. Therefore, photobleaching affects calculus ablation but does not necessarily prevent it.

Fluorescence spectroscopy (Fig. 134.56) supports the interpretation of the blue-light microscope images. The fluorescence spectra [Fig. 134.56(c)] of irradiated and nonirradiated photobleached calculus show that endogenous porphyrins (e.g., protoporphyrin IX and coporphyrin) in oral bacteria (e.g., *P. intermedia*, *P. nigrescens*, and *P. melaninogenica*) are the primary absorbers for 400-nm ablation. This finding is further supported by the corresponding SEM images in Fig. 134.57, which show empty pores and paucity of microorganisms on the surface of irradiated calculus. These diagnostics are unable to determine, however, the depth of this photobleached layer, which, from here on, we refer to as the "depletion layer." This depletion layer also leads to the measured increase in reflection/scattering of 400-nm radiation compared to nonirradiated calculus and clearly affects ablation by subsequent laser pulses.

The modified blowoff model appears well suited to explain calculus ablation at 400 nm, while the standard blowoff model does not. The assumption of permanent chromophore depletion agrees with the results of blue-light microscopy, fluorescence spectroscopy, and scattered-laser-light measurements. The model predicts a partially depleted layer of chromophores [Fig. 134.55(b)] with thickness ~$1/\mu_a$ beyond the etch depth after each laser pulse. The linear dependence of the average depth and volume removal rates with incident fluence (Fig. 134.57) also agrees with this model.

The modified blowoff model readily agrees with most of the observations in Figs. 134.55–134.58. This model does not, however, predict the ablation stalling seen in Fig. 134.56 nor the reduction of ablation depth and volume with successive laser pulses in Fig. 134.59. This limitation probably is caused mostly by the modified blowoff model neglecting scattering of laser light within dental calculus. These losses, especially within the depletion layer, can be significant because of multiple scattering, including broadening of the spot size. In addition, calculus formation is layered,[35] progressing from low chromo-

phore number density (low ρ_a), gram-positive bacteria[36] on the calculus/tooth interface to high ρ_a, gram-negative bacteria on the calculus surface.[36–40]

The gradual decrease in absorber density with depth and the concomitant increase in the depletion layer exacerbate the laser-light losses ahead of the region where it may be effectively absorbed. This naturally leads to decreasing removal rates with depth (Fig. 134.59) and potential stalling. This problem is compounded by the fact that the scattering length within dental hard tissue[41] is not much longer than typical measured etch depths. (For this purpose we have assumed scattering within calculus to be comparable to that in enamel.) The same reasoning also predicts that increasing the incident fluence and corresponding etch depths effectively prevents stalling before complete removal of the calculus layer. These conclusions agree with our observations that stalling occurs close to the ablation threshold (1 to 2 J/cm^2) and is typically not observed for fluences >6 J/cm^2.

Of significant importance is the fact that sound cementum and enamel are not ablated below 9 and 12 J/cm^2, respectively.[42] Therefore, selective calculus ablation without stalling is assured for fluences of 6 to 8 J/cm^2.

Most ablation experiments in this study were carried out with gamma-ray–sterilized teeth. However, comparison of ablation rates of sterilized and unsterilized teeth under otherwise identical conditions were essentially indistinguishable. Previous NUV ablation studies[43] carried out at 380 nm reported ablation fluences of 1 to 2 J/cm^2 for effective calculus ablation using unsterilized teeth. Our comparison study eliminates the possibility that sterilization of the teeth significantly affects calculus ablation. We therefore suspect that the complicated nature of the temporal laser pulse shape in the 380-nm experiments (two successive, irregular 100-ns pulses within ~10 μs) may account for the different reported relevant ablation fluences.

Conclusion

Calculus ablation at 400 nm is best described by a modified blowoff model that is based on chromophore depletion (photobleaching). The results presented here strongly suggest that the relevant calculus chromophores are bacterial porphyrins, endogenous to plaque and dental calculus. A thin surface layer of these chromophores becomes photobleached after each irradiation pulse. Tissue scattering within this photobleached layer exacerbated by a decreasing absorber (bacterial porphyrin) density with depth leads to decreasing removal rates with successive laser pulses and potential ablation stalling. Stalling can be avoided, however, by irradiating at incident fluences >6 J/cm^2.

ACKNOWLEDGMENT

We thank Dr. Georgios Romanos for contributing the nonsterilized tooth samples for this study. This work was supported by the U.S. Department of Energy Office of Inertial Confinement Fusion under Cooperative Agreement No. DE-FC52-08NA28302, the University of Rochester, and the New York State Energy Research and Development Authority. The support of DOE does not constitute an endorsement by DOE of the views expressed in this article. This work was also partially financially supported through a 2010 student grant from the American Society for Laser Medicine and Surgery (ASLMS).

REFERENCES

1. S. Jepsen *et al*., Periodontol. 2000 **55**, 167 (2011).
2. S. Nyman *et al*., J. Clin. Periodontol. **9**, 290 (1982).
3. P. Rechmann and T. Hennig, Med. Laser Appl. **16**, 223 (2001).
4. H. T. Bellini and J. R. Johansen, Acta Odontol. Scand. **31**, 283 (1973).
5. W. K. Brayer *et al*., J. Periodontal. **60**, 67 (1989).
6. J. Eberhard *et al*., J. Clin. Periodontol. **30**, 511 (2003).
7. A. Aoki *et al*., Periodontol. 2000 **36**, 59 (2004).
8. A. M. Polson *et al*., J. Periodontal. **55**, 443 (1984).
9. P. A. Adriaens *et al*., J. Periodontal. **59**, 493 (1988).
10. L. J. Walsh, Aust. Dent. J. **48**, 146 (2003).
11. D. Fried, in *Photon Processing in Microelectronics and Photonics IV*, edited by J. Fieret *et al*. (SPIE, Bellingham, WA, 2005), Vol. 5713, pp. 259–269.
12. F. Schwarz *et al*., J. Clin. Periodontol. **35**, 29 (2008).
13. F. Sgolastra *et al*., Lasers Med. Sci. **27**, 661 (2012).
14. P. Rechmann, Dent. Clin. North Am. **48**, 1077 (2004).
15. P. Rechmann, T. Hennig, and B. Spengler, in *The 4th International Congress on Lasers in Dentistry*, edited by H. Loh (Monduzzi Editore, International Proceedings Division, Bologna, Italy, 1994), pp. 159–162.
16. P. Rechmann, U.S. Patent No. 5,795,153 (18 August 1998).
17. T. E. Bramanti and S. C. Holt, J. Bacteriol. **173**, 7330 (1991).
18. J. E. Schoenly, W. Seka, and P. Rechmann, Lasers Surg. Med. **42**, 51 (2010).
19. J. E. Schoenly, W. D. Seka, and P. Rechmann, J. Biomed. Opt. **16**, 071404 (2011).
20. J. E. Schoenly, W. Seka, and P. Rechmann, in *Lasers in Dentistry XVI*, edited by P. Rechmann and D. Fried (SPIE, Bellingham, WA, 2010), Vol. 7549, p. 754906.

21. J. E. Schoenly, W. Seka, J. D. B. Featherstone, and P. Rechmann, Lasers Surg. Med. **44**, 339 (2012).

22. A. Vogel and V. Venugopalan, Chem. Rev. **103**, 577 (2003).

23. G. H. Pettit, in *Lasers in Medicine*, edited by R. W. Waynant (CRC Press, Boca Raton, FL, 2002), pp. 109–133.

24. R. Srinivasan, Science **234**, 559 (1986).

25. G. H. Pettit *et al*., Appl. Phys. A **58**, 573 (1994).

26. W. Buchalla, A. M. Lennon, and T. Attin, J. Periodontal. Res. **39**, 327 (2004).

27. Y. L. Qin *et al*., J. Photochem. Photobiol. B:Biol. **87**, 88 (2007).

28. W. C. Dolowy *et al*., J. Vet. Dent. **12**, 105 (1995).

29. B. T. K. Tan *et al*., J. Periodontal. **75**, 23 (2004).

30. H. E. Schroeder, Helv. Odont. Acta **8**, 117 (1964).

31. J. Friskopp and L. Hammarström, J. Periodontal. **51**, 553 (1980).

32. J. Friskopp, J. Periodontal. **54**, 542 (1983).

33. J. R. Taylor, *An Introduction to Error Analysis: The Study of Uncertainties in Physical Measurements*, Second ed., Third print (University Science Books, Sausalito, CA, 1997), p. 327.

34. P. Rechmann and T. Hennig, in *Medical Applications of Lasers III*, edited by S. G. Bown *et al*. (SPIE, Bellingham, WA, 1996), Vol. 2623, pp. 180–188.

35. D. J. White, Biofouling **4**, 209 (1991).

36. P. Marsh and M. Martin, *Oral Microbiology*, 4th ed. (Oxford, Boston, MA, 1999), p. 193.

37. L. J. Walsh and F. Shakibaie, Australas. Dent. Prac. **18**, 56 (2007).

38. N. S. Soukos *et al*., Antimicrob. Agents Chemother. **49**, 1391 (2005).

39. S. S. Socransky *et al*., J. Clin. Periodontol. **25**, 134 (1998).

40. W. E. C. Moore and L. V. H. Moore, Periodontol. 2000 **5**, 66 (1994).

41. D. Fried, R. E. Glena, J. D. B. Featherstone, and W. Seka, Appl. Opt. **34**, 1278 (1995).

42. J. E. Schoenly, "Selective Ablation of Dental Calculus at 400 nm," Ph.D. thesis, University of Rochester, 2012.

43. P. Rechmann and T. Hennig, in *Lasers in Dentistry*, edited by H. A. Wigdor, J. D. Featherstone, and J. M White (SPIE, Bellingham, WA, 1995), Vol. 2394, pp. 203–210.

Publications and Conference Presentations

Publications

D. R. Harding and W. T. Shmayda, "Stress- and Radiation-Induced Swelling in Plastic Capsules," Fusion Sci. Technol. **63**, 125 (2013).

D. R. Harding, M. D. Wittman, and D. H. Edgell, "Considerations and Requirements for Providing Cryogenic Targets for Direct-Drive Inertial Fusion Implosions at the National Ignition Facility," Fusion Sci. Technol. **63**, 95 (2013).

H. P. Howard, A. F. Aiello, J. G. Dressler, N. R. Edwards, T. J. Kessler, A. A. Kozlov, I. R. T. Manwaring, K. L. Marshall, J. B. Oliver, S. Papernov, A. L. Rigatti, A. N. Roux, A. W. Schmid, N. P. Slaney, C. C. Smith, B. N. Taylor, and S. D. Jacobs, "Improving the Performance of High-Laser-Damage-Threshold, Multilayer Dielectric Pulse-Compression Gratings Through Low-Temperature Chemical Cleaning," Appl. Opt. **52**, 1682 (2013).

S. X. Hu, D. T. Michel, D. H. Edgell, D. H. Froula, R. K. Follett, V. N. Goncharov, J. F. Myatt, S. Skupsky, and B. Yaakobi, "Hydrodynamic Simulations of Long-Scale-Length Two-Plasma–Decay Experiments at the Omega Laser Facility," Phys. Plasmas **20**, 032704 (2013).

M. Lafon, X. Ribeyre, and G. Schurtz, "Optimal Conditions for Shock Ignition of Scaled Cryogenic Deuterium–Tritium Targets," Phys. Plasmas **20**, 022708 (2013).

K. Mehrotra, H. P. Howard, S. D. Jacobs, and J. C. Lambropoulos, "Nanoindentation Probing of High-Aspect Ratio Pillar Structures on Optical Multilayer Dielectric Diffraction Gratings," in *Local Probing Techniques and In-Situ Measurements in Materials Science*, edited by N. Balke, H. Wang, J. Rijssenbeek, and T. Glatzel, Mater. Res. Soc. Symp. Proc. Vol. 1474 (Materials Research Society, Pittsburgh, PA, 2012).

W. T. Shmayda, D. R. Harding, V. Versteg, C. Kingsley, M. Hallgren, and S. J. Loucks, "Micron-Scaled Defects on Cryogenic Targets: An Assessment of Condensate Sources," Fusion Sci. Technol. **63**, 87 (2013).

Q. Wang, J. U. Wallace, T. Y.-H. Lee, J. J. Ou, Y.-T. Tsai, Y.-H. Huang, C.-C. Wu, L. J. Rothberg, and S. H. Chen, "Evaluation of Propylene-, *Meta*-, and *Para*-Linked Triazine and *Tert*-Butyltriphenylamine as Bipolar Hosts for Phosphorescent Organic Light-Emitting Diodes," J. Mater. Chem. C **1**, 2224 (2013).

Forthcoming Publications

K. S. Anderson, R. Betti, P. W. McKenty, T. J. B. Collins, M. Hohenberger, W. Theobald, R. S. Craxton, J. A. Delettrez, M. Lafon, J. A. Marozas, R. Nora, S. Skupsky, and A. Shvydky, "A Polar-Drive Shock-Ignition Design for the National Ignition Facility," to be published in Physics of Plasmas.

C. Dorrer, "Analysis of Pulse Replicators for High-Bandwidth, High-Dynamic-Range, Single-Shot Optical Characterization," to be published in the Journal of Lightwave Technology.

C. Dorrer, "Analysis of the Chromaticity of Near-Field Binary Beam Shapers," to be published in Applied Optics.

L. Gao, P. M. Nilson, I. V. Igumenshchev, G. Fiksel, R. Yan, J. R. Davies, D. Martinez, V. A. Smalyuk, M. G. Haines, E. G. Blackman, D. H. Froula, R. Betti, and D. D. Meyerhofer, "Observation of Self-Similarity in the Magnetic Fields Generated by the Ablative Nonlinear Rayleigh–Taylor Instability," to be published in Physical Review Letters.

V. N. Goncharov, "Cryogenic Deuterium and Deuterium–Tritium Direct-Drive Implosions on OMEGA," to be published in Laser-Plasma Interactions and Applications.

I. V. Igumenshchev, D. H. Froula, D. H. Edgell, V. N. Goncharov, T. J. Kessler, F. J. Marshall, R. L. McCrory, P. W.

McKenty, D. D. Meyerhofer, D. T. Michel, T. C. Sangster, W. Seka, and S. Skupsky, "Laser-Beam Zooming to Mitigate Crossed-Beam Energy Losses in Direct-Drive Implosions," to be published in Physical Review Letters.

J. F. Myatt, H. X. Vu, D. F. DuBois, D. A. Russell, J. Zhang, R. W. Short, A. V. Maximov, W. Seka, and D. H. Edgell, "Mitigation of Two-Plasmon Decay in Direct-Drive Inertial Confinement Fusion Through the Manipulation of Ion-Acoustic and Langmuir Wave Damping," to be published in Physics of Plasmas.

S. Papernov, "Mechanisms of Near-Ultraviolet, Nanosecond-Pulse Laser Damage in HfO_2/SiO_2–Based Multilayer Coatings," to be published in Chinese Optics Letters.

L. Parlato, R. Arpaia, C. De Lisio, F. Miletto Granozio, G. Pepe, P. Perna, V. Pagliarulo, C. Bonavolonta, M. Radovic, Y. Wang, R. Sobolewski, and U. Scotti di Uccio, "Time-Resolved Optical Response of All-Oxide $YBa_2Cu_3O_7/La_{0.7}Sr_{0.3}MnO$ Proximitized Bilayers," to be published in Physical Review B.

J. Qiao, P. A. Jaanimagi, R. Boni, J. Bromage, and E. Hill, "Measuring 8- to 250-ps Short Pulses Using a High-Speed Streak Camera on Kilojoule, Petawatt-Class Laser Systems," to be published in Review of Scientific Instruments.

Conference Presentations

R. L. McCrory, "LLE FY13–FY15 Plans," 2013 ICF Executives Meeting, Washington, DC, 10 January 2013.

The following presentations were made at LASE Photonics West, San Francisco, CA, 2–7 February 2013:

M. Barczys, S.-W. Bahk, M. Spilatro, D. Coppenbarger, E. Hill, T. Hinterman, R. W. Kidder, J. Puth, T. Touris, and J. D. Zuegel, "Deployment of a Spatial Light Modulator-Based Beam-Shaping System on the OMEGA EP Laser."

J. H. Kelly, A. Shvydky, J. A. Marozas, M. J. Guardalben, B. E. Kruschwitz, L. J. Waxer, C. Dorrer, E. Hill, and A. V. Okishev, "Simulations of the Propagation of Multiple-FM Smoothing by Spectral Dispersion on OMEGA EP."

B. E. Kruschwitz, J. H. Kelly, C. Dorrer, A. V. Okishev, L. J. Waxer, G. Balonek, I. A. Begishev, W. A. Bittle, A. Consentino, R. Cuffney, E. Hill, J. A. Marozas, M. Moore, R. G. Roides, and J. D. Zuegel, "Commissioning of a Multiple-FM Smoothing by Spectral Dispersion Demonstration System on OMEGA EP."

A. V. Okishev, I. A. Begishev, R. Cuffney, S. Papernov, and J. D. Zuegel, "A Highly Energetic Multiwavelength Diode-Pumped Nanosecond Laser System with Flexible Pulse-Shaping Capability."

J. E. Schoenly, W. Seka, G. Romanos, and P. Rechmann, "The Efficacy of Selective Calculus Ablation at 400 nm: Comparison to Conventional Calculus Removal Methods," Lasers in Dentistry XIX, San Francisco, CA, 2–7 February 2013.

L. Gao, P. M. Nilson, I. V. Igumenshchev, G. Fiksel, R. Yan, J. R. Davies, D. Froula, R. Betti, D. D. Meyerhofer, M. G. Haines, D. Martinez, V. A. Smalyuk, and E. Blackman, "Observation of Self-Similarity in the Magnetic Fields Generated by the Nonlinear Rayleigh–Taylor Instability," Workshop on Exploratory Topics in Plasma and Fusion Research, Fort Worth, TX, 12–15 February 2013.

R. L. McCrory, "Direct-Drive and Alternate Approaches for Laser Inertial Confinement Fusion," 2013 AAAS Annual Meeting, Boston, MA, 14–18 February 2013.

D. H. Froula, J. Bromage, D. Haberberger, P. M. Nilson, J. D. Zuegel, and D. D. Meyerhofer, "Ultrahigh-Intensity Research Plans at the Laboratory for Laser Energetics," Workshop on Frontiers in Extreme Relativistic Optics, Columbus, OH, 20–21 February 2013.

M. M. Mayton, Z. Hobbs, and S. D. Jacobs, "Reclamation of Slurries Used in Optics Manufacturing," The Center for Emerging and Innovative Sciences, University Technology Showcase, Rochester, NY, 26 March 2013.


1850
MELIORA
UNIVERSITY of
ROCHESTER